Deposition rate, composition and sources of light-absorbing particles in the Langtang Valley in the Himalaya

Immerzeel, W.W. (October, 2018) Langtang Valley, Nepal

Kari-Anne Gerritsen

Universiteit Utrecht

Deposition rate, composition and sources of light-absorbing particles in the Langtang Valley in the Himalaya

MSc Thesis

March-2019

Author: Kari-Anne Gerritsen

Student number: 4043642

E-mail: k.e.gerritsen@students.uu.nl

Supervised by: Dr. G. Sterk, Dr. W.W. Immerzeel and J.F. Steiner MSc

MSc Programme: Earth Surface and Water

Faculty of Geosciences

Department of Physical Geography

Utrecht University

Acknowledgements

I would like to thank Walter Immerzeel and Jakob Steiner for their guidance in the field and for teaching me how to perform field work in high mountain areas. I am very grateful for the opportunity to collect my own measurements and for the experience to do field work in the Himalaya. Additionally, I would like to thank Jakob Steiner for thinking along with me and helping me to solve problems I faced during my thesis. Furthermore, I would like to thank Walter Immerzeel again, for the opportunity to perform field work in the Himalaya and for providing funding for the usage of the SEM. I would like to thank Geert Sterk for the useful feedback and meetings during my thesis. Furthermore, I would like to thank Gyalbu and Lopsang Tamang and their children for their hospitality and guidance in the field. I would like to thank Natasja Welters for the guidance in the lab. Furthermore, I would like to thank Friederike Wagner-Cremer, Fabian Ercan, Oliver Plümper and Maartje Hamers for their help with the microscopes. Finally, I would like to thank my fellow students for their feedback, mental support and enjoyable coffee breaks and lunches.

Abbreviations

AAI	Absorbing Aerosol Index
ABC	Atmospheric Brown Cloud
AE	Angstrom Exponent
AERONET	AErosol RObotic NETwork
AOD	Aerosol Optical Depth
BC	Black Carbon
CAMS	Copernicus Atmospheric Monitoring Service
CO	Carbon Monoxide
EDX	Energy Dispersive X-ray Spectroscopy
keV	kilo-electronVolt
LAP	Light-Absorbing Particle
NIR	Near-Infrared
Ppmw	parts per million by weight
SEM	Scanning Electron Microscopy
TROPOMI	TROPOspheric Monitoring Instrument
UVAI	UltraViolet Aerosol Index

Abstract

Millions of people in Asia depend on the meltwater of the Himalayan glaciers and snow. They serve as water storage, are used to generate hydropower and act as water source for major rivers in Asia. Due to global warming, the Himalayan glaciers are melting. Besides global warming, light-absorbing particles (LAPs) cause an increase in glacier melt by decreasing the ice albedo. Concentrations of LAPs have increased since the industrial revolution due to an increase in biomass and fossil fuel burning, induced drought and land-use change. The Himalaya is sensitive of LAPs because of the high air pollution at the Indo-Gangetic plain. Much research is done on the influence of LAPs on glaciers, especially for dust and black carbon (BC). However, it is unknown if this air pollution from the Indo-Gangetic plain reaches the high mountain areas of the Himalaya. Therefore, the main aim of this study is to understand if the source of LAPs in high Asia is local or whether the source is pollution from the Indo-Gangetic plain. The second aim of this study is to identify the deposition rate and composition of LAPs for the Langtang Valley in Nepal. To reach the aims of the study a ten-day field work was performed in the Langtang Valley. During the field work, aerosols were collected with two distinct measurement set-ups. The samples collected in the field were analysed with a microscope for the coarse LAPs and with a scanning electron microscope for the fine LAPs. Additionally, to detect possible LAP sources and estimate LAPs outside of the Langtang Valley, satellite images were analysed. Carbon monoxide and the ultra-violet aerosol index data were used to detect dust and black carbon in the atmosphere. Aerosol concentrations were determined to be highest during the pre-monsoon season and the lowest during the monsoon season. In number approximately 85% of the coarse LAPs consisted of transparent silicates. For the fine LAPs aluminosilicates had the highest abundancy. Some BC was measured but in very low concentrations. Therefore, it is suspected that most LAPs come from local sources and not from the Indo-Gangetic plain.

Table of Contents

1. Introduction

The Himalaya holds the largest amount of ice mass after the polar regions (Bolch et al., 2012; Li et al., 2016; Thompson et al., 2000; Ye & Wu, 1998), which makes the Himalayan glaciers important for the local water cycle (Fujita, 2007). They act as a water source for major rivers in Asia (Cong et al., 2015; Qian et al., 2011; Qu et al., 2014), serve as water storage and are used to generate hydropower (Scherler et al., 2011). This makes the glaciers an important water source for hundreds of millions of people (Immerzeel et al., 2010; Lutz et al., 2014; Orr et al., 2017).

The Himalayan glaciers are melting rapidly due to climate change (Xu et al., 2009). Because of the importance of the glaciers in the Himalaya, rapid melting can lead to several problems. First of all, the rapid melting causes shrinking of the glaciers, which will lead to increased river discharges on the short term and a reduced river discharge on the long term (Scherler et al., 2011; Huss & Hock, 2018). The higher discharges can cause natural hazards like soil erosion and floods in nearby areas (Lau et al., 2010), being a result of the extra released water from the glaciers. The reduced river discharges on the long term can have serious consequences for people who depend on water from rivers fed by the Himalayan glaciers. Furthermore, shrinking of the glaciers will lead to an increase in the seasonality of runoff, irrigation and hydropower supply (Bolch et al., 2012).

In addition to climate change, there are more causes for the melting of the glaciers in the Himalaya. One of these causes is the reduction of the albedo of the ice by light-absorbing particles (LAPs). Ice is one of the most (naturally) reflective surfaces on earth (Gul et al., 2017). Therefore, ice has a high albedo, which is defined as the ratio of the reflected flux density to the incident flux density for radiation. The cleaner the ice, the higher the albedo (Qu et al., 2014). When LAPs are deposited on glaciers, they can decrease the albedo of the ice significantly (Gul et al., 2017; Kaspari et al., 2014; Lüthi et al., 2015; Qian et al., 2015) because LAPs absorb solar radiation (Yasunari et al., 2010). Several glaciers in the Himalayan Langtang catchment in Nepal, are covered with these dark coloured LAPs (Kohshima & Yoshimura, 1993). The decrease of the albedo of the ice and the absorbance of solar radiation by the LAPs causes (increased) melting of the glaciers (Kaspari et al., 2014; Lu et al., 2012).

The aerosols that act as LAPs on glaciers can consist of several absorbing materials like black carbon (BC), organic material, or mineral dust (Lau et al., 2010; Marcq et al., 2010; Marinoni et al., 2010; Ramanathan and Carmichael, 2008). In some studies, BC is considered as one of the most influencing LAPs because of the high mass absorption coefficient of BC. The absorption coefficient of BC is approximately 10 times higher as for mineral dust (Gabbi et al., 2015). However, the absorbance capacity of BC depends on several factors, including: fuel species, moisture content and burn rate (Venkataraman et al., 2005). Besides, the extent to which dust and BC absorb radiation highly depends on the particle size and the mixture state between BC, dust and other light-absorbing materials (Kaspari et al., 2014; Dong et al., 2018).

Much research about LAPs in the Himalaya focuses on BC and mineral dust (Chen et al., 2018; Cong et al., 2015; Kaspari et al., 2014; Li et al., 2016). However, some studies focused on other LAP materials in the Langtang Valley (Kohshima & Yoshimura, 1993). The research of Kohshima & Yoshimura (1993) points at mud-like materials which consists of algae and bacteria, which act as LAPs on glaciers in the Langtang Valley. The difference between this study and studies that focused on BC and dust, is that their research was performed during the monsoon season. The reason for choosing that period is that the microbial production on glacial surfaces is largest during the monsoon. (Kohshima and Yoshimura, 1993). This in contrast to BC concentrations, which are smallest during the monsoon period (Chen et al., 2018).

Despite the many studies done about LAPs in the Langtang Valley, there are still some important questions left. To understand the effect of LAPs on the glaciers in the Langtang catchment, it is important to know what the source and composition is of the LAPs in the area. Therefore, the aim of this study is to understand if the source of the LAPs is local or whether the source is pollution in the Into-Gangetic plain. The second aim is to characterize and quantify the amount of the LAPs on the glaciers of the Himalayan Langtang catchment. It is suspected that most of the LAPs at high

altitude in the Himalaya consist of dust from a local source. To reach the aim of the study the following specific objectives are defined:

- Characterize the composition of the LAPs
- Quantify the LAP deposition rates and their seasonality in the Langtang Valley.
- Determine if the source areas of the LAPs in the Langtang Valley are local or from further areas.

2. Study area

The study area is in the Upper Langtang catchment in the Himalaya in Nepal (Figure 1). The catchment has an area of 584 km^2, is located 60 km north of Kathmandu and borders with the Tibetan Autonomous Region (Collier & Immerzeel, 2015). The climate has a summer monsoon season from June until September with heavy precipitation. In this period 75% of the annual snow accumulation occurs in locations with an elevation high enough to have temperatures below zero in summer (Orr et al., 2017; Steinegger et al., 1993). During summer there are prevailing easterly winds while during the other seasons there are primarily westerly winds (Immerzeel et al., 2014). During the post-monsoon season, the period in which the field work took place, the influence of westerlies increases. This causes cooling and drying of the atmosphere (Collier & Immerzeel, 2015). The average temperatures in the catchment differ per location due to the elevation differences, which ranges from 1406 to 7180 m a.s.l. (meter above sea level) (Collier & Immerzeel, 2015). For Kyanjin (3980 m a.s.l.) the average yearly temperature is 4.0 °C. For the summer the average temperature lays around 9.4 °C and for the winter around 0.2 °C (Immerzeel et al., 2014). For the other measurement locations (Langshisha and Lirung) these temperature data are not available. Because of the cold winters and high precipitation during the summers, spring and autumn are the best months to perform field work in the study area. For this study, data were collected from three locations within the Langtang catchment: Kyanjin (N28.21082, E85.57110, elevation: 3890 m a.s.l.), Lirung (N28.23888, E85.56107, elevation: 4250 m a.s.l.) and Langshisha (N28.21365, E85.67154, elevation: 4104 m a.s.l.) (Figure 1).

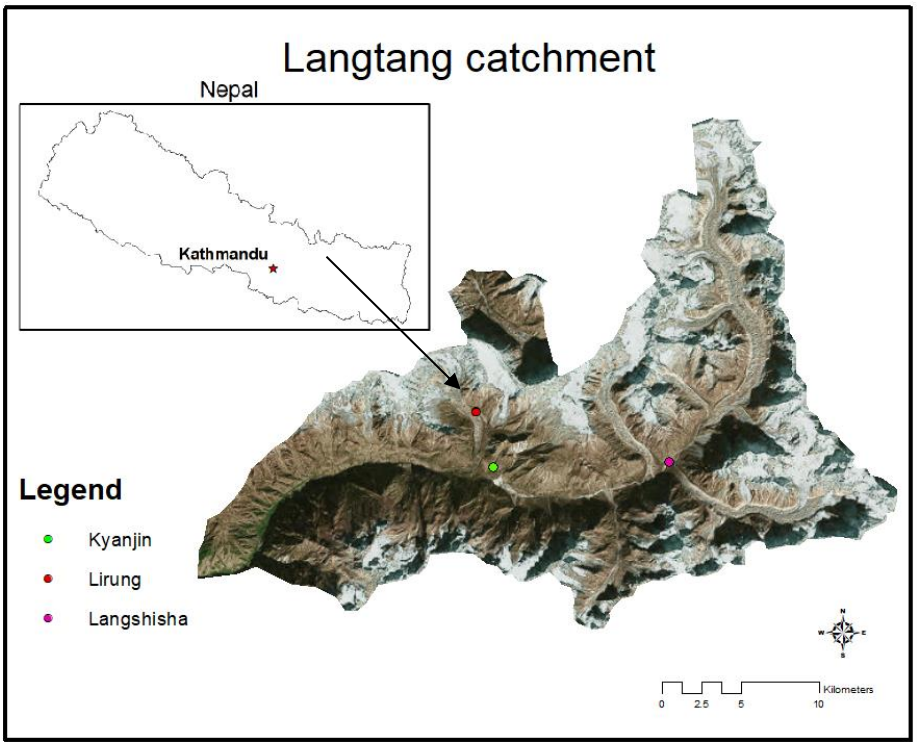

Figure 1: Map of the study area with the measurement locations (Source: Esri, DigitalGlobe, GeoEye, Earthstar Geographics, CNES/Airbus DS, USDA, USGS, AeroGRID, IGN, and the GIS User Community)

The measurement location Kyanjin was located near to the village Kyanjin, which is the highest village in the valley. The measurement site was located on an open field with small bushes and a sandy soil (Figure 2). On the field yaks were grazing frequently and the field was located next to hiking trails. A helicopter landing pad was located nearby the measurement site.

Measurements at Lirung were taken at the top of a moraine of the Lirung Glacier (Figure 2). Lirung is a debris-covered glacier covered with dust, silts, sands, gravel, cobbles, and boulders (Adhikary et al., 2000). The moraine also consists of these materials and is, at some places, covered with small vegetation patches. The location lays in between the high mountains Langtang Lirung, 7234m and Tsangbu Ri, 6781m.

Langshisha was located next to Langshisha basecamp on a relatively open area parallel to the valley (Figure 2). Langshisha was located on an alluvial plain close to the river. The surface was covered with vegetation and there was a silty/sandy soil.

Figure 2: Images of the three measurement sites. a: Kyanjin, b: Lirung, c: Langshisha (Figure 1)

3. Literature review

3.1 Impact of LAPs on glaciers

When LAPs are deposited on a snow or ice surface they have a warming effect on the snow or ice which induces (increased) melting (Gul et al., 2017; Lau et al., 2010; Qu et al., 2014). This warming effect is caused by the high absorbance capacity of solar radiation in the visible wavelengths by LAPs, the part of the electromagnetic spectrum where ice is most reflective (Skiles et al., 2018). Ice is one of the brightest natural surfaces on earth, while LAPs are typically dark in colour (Skiles et al., 2018). Because of this high contrast in absorbance capacity between LAPs and snow, only small amounts of LAPs can already directly reduce the albedo in the visible spectrum (Warren and Wiscombe, 1980). For the Near-Infrared (NIR) wavelengths this process is smaller since ice is already highly absorptive for the NIR wavelengths. Besides this process, there is a second feedback whereby LAPs cause ice to melt faster. This is the grain-size feedback, whereby the snow grain size increases due to snow aging caused by LAPs (Skiles et al., 2018). The snow grain size also influences the albedo of the snow in the NIR wavelength (Figure 3) (Gabbi et al., 2015). When the snow grain size increases, the scattering within the snowpack decreases and the absorbing path length within snow grains increases. This leads to a decrease in the albedo (Adolph et al., 2017). Skiles et al. (2018) modelled the decrease in snow albedo for different LAP concentrations (Figure 3). The graphs in Figure 3 show a decrease in albedo for an increase in LAP content for the visible spectrum. The higher the concentration of dust/BC the more the albedo decreases. Furthermore, a larger ice radius leads to a larger decrease in albedo due to the grain-size feedback process (Figure 3) (Warren and Wiscombe, 1980; Skiles et al., 2018).

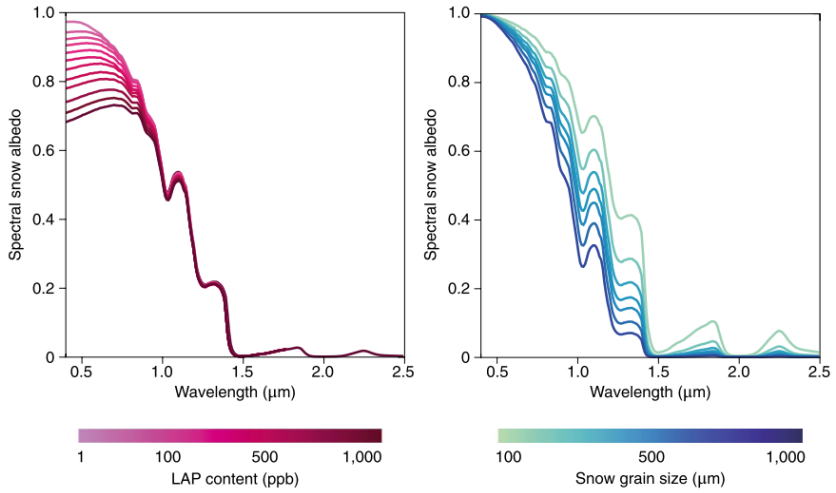

Figure 3: Influence of LAP content and snow grain size on the spectral snow albedo (Skiles et al., 2018)

Dust and BC combined can cause potential annual melt of 713 kg/m^2 ice per year for certain areas in the Himalayan Mountains (Ginot et al., 2014). Qian et al. (2011) simulated the deposition and concentration of BC and dust for the Tibetan Plateau to determine the influence of LAPs on the snow albedo and snow melt. They found that BC caused an albedo reduction of 0.04 and dust an albedo reduction of 0.02 for the south-western part of the Tibetan Plateau. This reduction in albedo led to an average increase in surface air temperature of about 1.0 °C for the Tibetan Plateau (Qian et al., 2011). This rise in surface temperature caused increased and earlier snowmelt during the melting season (Kaspari et al., 2014; Qian et al., 2011).

Gabbi et al. (2015) assessed the presence of Saharan dust and BC on a glacier in the Alps from 1914-2014 with the use of ice cores. Additionally, they examined the contribution of these LAPs on glacier melt. They measured an average albedo reduction of less than 0.01 by Saharan dust. This albedo reduction caused a mean decrease in mass balance of 28-58 mm w.e. (mm water equivalent). However, these values are an average over 100 years. The mass balance decreased substantially for some individual years with a high supply of Saharan dust. For BC, Gabbi et al. (2015) measured a mean annual albedo reduction of 0.03. This reduction in albedo caused a decrease in mass balance of 183-301 mm w.e. Together BC and Saharan dust caused an average increased annual ice loss of 15-19% for the period 1914-2014 (Gabbi et al., 2015). Painter et al. (2007) measured a decreased albedo in the visible spectrum from 0.92 for clean snow to 0.50 for snow covered with dust in the San Juan mountains, Colorado, US.

Warren and Wiscombe (1980) studied the effect of particle size of dust and soot (BC is the absorbing component of soot (Kaspari et al., 2011)) on snow albedo. Warren and Wiscombe (1980) detected that, for similar mass concentrations, smaller particles have a greater effect on albedo reduction than larger particles. Furthermore, soot has a larger effect on the albedo than dust. Dust concentrations of 20 ppmw (parts per million by weight) will decrease the albedo by the same amount as soot concentrations of only 0.3 ppmw (Warren and Wiscombe, 1980). This could partly be caused by the smaller grain size of soot compared to dust, or by the higher radiation absorbance capacity of soot. Although, in large concentrations dust can reduce the albedo to the same extent as soot. The study of Gabbi et al. (2015) showed comparable results for measurements in the Alps. Gabbi et al. (2015) measured a 5 times higher mineral dust concentration than BC concentration at the surface. However, since BC has a higher absorptivity coefficient than mineral dust, the effects of BC and mineral dust were established to be in the same order of magnitude for this area (Gabbi et al., 2015). The absorption by BC was higher than the absorption by mineral dust in general, but for some years, with high Saharan dust input, the mineral dust had a higher absorbance capacity than the BC (Gabbi et al., 2015). Additionally, the difference in absorption between BC and mineral dust was higher at higher altitudes. The lower difference in absorption between BC and mineral dust at lower altitudes is probably due to the higher removal rate of BC by snowmelt (Gabbi et al., 2015). Apart from LAP type,

LAP particle size and snow grain size, other factors that affect the reduction of the albedo are: solar zenith angle, snow depth, impurity ice/mixing state and liquid water (Warren and Wiscombe, 1980; Kaspari et al., 2014). However, this is beyond the scope of this research and focus will be primarily on LAPs.

3.2 Distribution and seasonality of LAPs

Previous research discovered that the lowest BC concentrations are during the monsoon season (June till October) and the highest BC concentrations are present during the pre-monsoon season (March till June) for the southern slope of the Himalaya (Chen et al., 2018). However, the values for the BC concentrations during the post-monsoon season (October till December) and the winter (December till March) are still lower than for the pre-monsoon season (Chen et al., 2018; Ginot et al., 2014). Measurements show a considerable variation in seasonal distribution for the BC concentrations in the Himalaya.

The average daily atmospheric BC concentration measured by Chen et al. (2018) in the Mt. Everest region was 0.30±0.34 μg/m^3. The highest daily BC concentration measured was during the pre-monsoon with a value of 2.8 μg/m^3, and the lowest daily BC concentration occurred during the monsoon with a value of 0.04 μg/m^3 (Table 1). These measurements were taken at an elevation of 4276 m a.s.l. Marinoni et al. (2010) measured BC concentrations in the Southern Himalaya at an elevation of 5079 m a.s.l. They measured an average annual concentration of 0.11 μg/m^3. The highest concentrations measured were during the pre-monsoon with values of 0.32±0.47 μg/m^{-3} and the lowest concentrations during the monsoon with values of 0.06±0.08 μg/m^{-3} (Table 1). Notable are the higher concentrations at lower altitude for the annual average and the pre-monsoon values while the concentrations during the monsoon are slightly higher at higher altitude (Table 1). Furthermore, these values are relatively low when compared to BC concentrations at Kathmandu. Putero et al. (2015) measured average annual BC concentrations of 11 μg/m^3 at Kathmandu. The highest BC concentrations were during the pre-monsoon with concentrations often exceeding 20 μg/m^3. The lowest concentration measured by Putero et al. (2015) was for the monsoon season with a value of 2.5 μg/m^3. Besides the large difference in concentrations, all three studies showed an increase in BC concentration during the post-monsoon and the winter (Chen etl al., 2018; Marinoni et al., 2010; Putero et al., 2015).

Table 1: BC concentrations for different elevations in the Himalaya and Kathmandu (Chen et al., 2018; Marinoni et al., 2010; Putero et al., 2015)

BC concentrations (μg/m^3)	Himalaya, 4276 m a.s.l. (Chen et al., 2018)	Himalaya, 5079 m a.s.l. (Marinoni et al., 2010)	Kathmandu (Putero et al., 2015)
Average annual	0.30±0.34	0.11	11
Pre-monsoon	2.80	0.32±0.47	>20
Monsoon	0.04	0.06±0.08	2.5

The variation in BC is caused by several seasonal conditions, and can be explained by the following processes (Bonasoni et al., 2010). First of all, the difference in BC concentrations for the pre-monsoon and the monsoon season could be a consequence of the larger number of agricultural and forest fires during the dry pre-monsoon period (Cong et al., 2015). During the dry months (November to May) atmospheric brown cloud (ABC) conditions are frequently observed on the southern side of the Himalaya (Lüthi et al., 2015), which could cause the higher concentrations of BC for the pre-monsoon season (Bonasoni et al., 2010). ABCs are often a result of bio-mass and fossil fuel burning during the dry season (Bonasoni et al., 2010; Ramanathan et al., 2007). Most BC aerosol emission originates from the Indo-Gangetic plain and China (Li et al., 2016). Therefore, studies suggest that the main source for BC on the Himalayan glaciers is originating from the Indo-Gangetic plain and East Asia (He et al., 2014; Li et al., 2016; Zhang et al., 2015). However, the models used in these studies are uncertain for the source-area emissions and air transport for the Himalayan areas (Li et al., 2016). Furthermore, it is questionable if BC can reach the high altitudes of the Himalayan glaciers, which is

important since most glaciers at lower altitudes are debris-covered and will therefore not be influenced by LAPs. Another reason for the seasonality of BC concentrations could be the change in prevailing wind direction. The westerly winds in the pre-monsoon period distribute air from the Indo-Gangetic plain towards the Himalayan area (Chen et al., 2018; Wang et al., 2015), while during the monsoon period southerly winds take air from the Arabic sea into the Himalayan area (Chen et al., 2018). There is less pollution around the Arabic Sea than at the Indo-Gangetic plain, and therefore these southerly winds will import lower BC concentrations. Another reason for the lower aerosol rates at higher altitudes in the monsoon season could be the high wet removal rates of aerosols from the atmosphere by the monsoon rainfall before they reach the higher mountainous regions (Marinoni et al., 2010). Due to the monsoon rains, the aerosols can travel smaller distances (Marinoni et al., 2010). Because of this large seasonality of the concentrations of BC, it is suspected that most of the BC comes from sources further away from the study area (Chen et al., 2018). In contrast to BC, dust is distributed more evenly over the year (Ginot et al., 2014). This can be an indication that dust comes from more nearby areas. However, little literature is available about the origin of dust LAPs for the Himalayan area.

3.3 Types of Light-absorbing particles

LAPs can consist of several materials, as there are several materials that absorb light. Examples of light-absorbing materials are: black carbon/soot, (mineral) dust, algae/bacteria, and organic material. Most of these materials are transported in the atmosphere as aerosols although algae/bacteria also can grow on a glacier. The LAPs can mix with each other. Fan et al. (2016) took aerosol measurements in Shangri-La, Tibetan Plateau. They found that 81% of the particles were mixed with two or more aerosols from different sources (Fan et al., 2016). Therefore, LAPs can consist of more elements/aerosol types.

Table 2: Types of aerosol particles and their properties (Fan et al., 2016; Cong et al., 2008)

Particle type	Major elements	Minor elements	Morphology
BC/soot	C	S	Round particles, chain aggregates
Dust	Si	Al, Na, Mg, K, Ca, or Fe	Irregular
Organic	C	Ca, Na, Mg, P, or K	Variable morphology

Black carbon (BC)/soot

There does not exist one clear definition of BC. Buseck et al. (2012) defined BC as: ''Light-absorbing refractory carbonaceous matter of uncertain character and BC should be used with a definition to explain what is meant''. While Kaspari et al. (2011) defined BC as: ''The absorbing component of soot''. BC can consist of several materials like soot, organic carbon or other carbonaceous LAP types (Buseck et al., 2012). For this study BC is defined as light-absorbing carbonaceous rich particles, generated by combustion. This mainly comes down to soot particles. Soot is produced during incomplete combustion of fossil fuels or biomass burning (Brodowski et al., 2005; Skiles et al., 2018).

BC has a high absorbance capacity. In snow, BC causes higher snowpack reduction than CO_2 increase in the air, even though the magnitude of surface air warming induced by the two are similar (Qian et al., 2011). BC has always been present on Earth, but concentrations have strongly increased since the mid-nineteenth century due to the industrial revolution, growing populations, and more intense forest fires (Skiles et al., 2018). The study of Kaspari et al. (2011) measured a threefold increase for BC concentrations between pre-industrial and industrial times for the Mt. Everest area. This increase indicates that BC from anthropogenic sources can be transported up to high elevation regions (Kaspari et al., 2011). However, the concentration of BC is significantly lower at higher altitudes than at lower altitudes. Their attachment to dust and particle size also decreases with higher elevations (Clarke et al., 2004).

The main element of BC is carbon (C) and it often contains a minor amount of sulphur (S) (Table 2) (Cong et al., 2008; Fan et al., 2016). Individual BC particles can vary in size from 1 to 500 µm

(Brodowski et al., 2005), and particles are spherical or near-spherical in shape. Soot particles often clump together into chains or compact aggregates (Clarke et al., 2004; Brodowksi et al., 2005). The high variety in particle size is due to many existing types of BC. The burning of different materials delivers different types of BC. For instance, the burning of coal will deliver another type of BC than the burning of oil (Brodowski et al., 2005). Not only the particle size for different types of BC is variable but also the carbon/oxygen ratio (C/O ratio) varies per BC type. Therefore, the C/O ratio of BC can give an indication for the type and source of BC. The C/O of BC varies from 0.11 to 0.27 (Brodowski et al., 2005).

Dust

In this study dust is considered to consist of clay and/or silicate minerals. By mass, dust is the most common atmospheric aerosol and it originates from arid and semi-arid landscapes (Skiles et al., 2018). Dust concentrations depend on local soil moisture, surface wind speed, soil erodibility and vegetation (Qian et al., 2011). Due to climate change, induced drought and land-use change, the amount of atmospheric dust has doubled during the twentieth century (Skiles et al., 2018). This increase in dust emission is global in nature (Painter et al., 2007). Thompson et al. (2000) measured a fourfold increase in dust since 1860 on the Dasuopu Glacier in Tibet, nearby the Langtang Valley. They found a strong correlation between increased dust levels and temperature increase. Much mineral dust at the Tibetan plateau originates from arid regions in Southwest Asia (Thar desert and Arabian Peninsula), transported by prevailing westerly winds (Qian et al., 2015).

Silica minerals are by itself relatively transparent and therefore have a limited effect on the albedo (Warren and Wiscombe, 1980). However, clay minerals often have inclusions of high absorbent materials such as irons oxide, carbon, or organic material (Warren and Wiscombe, 1980), which causes the minerals to act as LAPs when deposited on an ice surface. Therefore, the content of iron oxides, carbon and organic material highly influences the absorption of mineral dust in the visible spectrum (Gabbi et al., 2015; Warren and Wiscombe, 1980). The dependency of these absorptive constituents for dust to act as a LAP, causes a high variability in colour and absorption of sun-light for dust particles.

Algae/bacteria

Algae and bacteria can act as LAPs. When they cover the surface of a glacier, they create a dark coloured mud-like material (Kohshima & Yoshimura 1993). Algae and bacteria can be transported by wind or by animals to glaciers and can grow below the surface of snow packs (Skiles et al., 2018). The production of these algae and bacteria typically takes place during the monsoon season. Kohshima & Yoshimura (1993) estimated the effect of algae and bacteria during the monsoon of 1991 on the Yala Glacier, which is in the Langtang Valley. They found that 5% to 22% of the mud-like material on the glacier consisted of organic matter of which most were microbes. The albedo of the ice covered with this organic matter was only 20% to 50%. For comparison, the albedo of white snow was determined to be 70% to 90% (Kohshima & Yoshimura 1993). Furthermore, they found that many mineral grains were covered with microbes. These minerals had a transparent colour from themselves. Therefore, the microbes not only darkened the glacier by direct deposition/production, but they also darkened the glacier indirectly by darkening mineral grains.

Organic material

Organic materials are irregular in shape, and the main element is carbon (C). They can contain trace elements of oxygen (O), sulphur (S), potassium (K) and phosphor (P). Organic material can have a broad variety in shape and colour (Skiles et al., 2018). Therefore, their absorptivity is also highly variable. This makes it hard to determine their influence on ice albedo. In general, they are less absorptive than BC and dust.

3.4 Remote sensing of aerosols

Atmospheric Brown Clouds (ABC) can be observed using remote sensing data (Figure 4). Several studies used remote sensing to observe ABCs and aerosols in the air. Because of the fast improvement of satellite observation, the best method to do this also evolves fast. It is possible to classify aerosols in the air with the use of remote sensing, so that light-absorbing aerosols can be distinguished from light-reflective aerosols. To classify aerosols with remote sensing it is crucial to determine two aerosol properties; the aerosol size and the UV absorption of the aerosol (Penning De Vries et al., 2015).

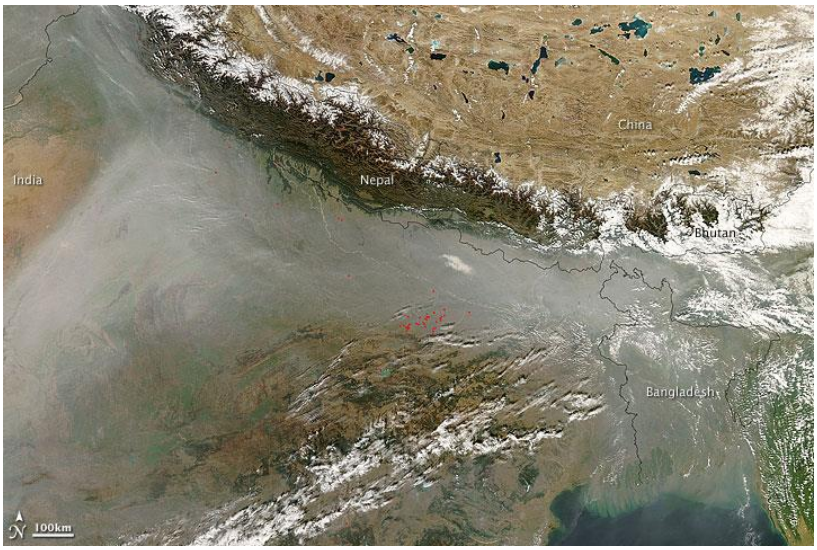

Figure 4: Atmospheric Brown Cloud at Northern India and Southern Nepal, 2008-12-11. The red dots are small fires (Source: NASA, https://earthobservatory.nasa.gov/images/36158/haze-over-india-and-the-bay-of-bengal)

Fine aerosols have a size between 0.1 µm and 1.0 µm and coarse aerosols are defined as larger than 1.0 µm (Kokhanovsky & De Leeuw, 2009). Fine aerosols are mainly produced during bio-mass burning while coarse aerosols are more likely to come from natural sources like sea salt and soil dust (Kokhanovsky & De Leeuw, 2009). To determine the size of aerosols the aerosol optical depth (AOD) can be used (Penning De Vries et al., 2015). The AOD is the measure of aerosols distributed within a column of air from the Earth's surface to the top of the atmosphere. From the AOD the size distribution of aerosols can be estimated. This is done by calculating the Angstrom Exponent (AE) (Penning De Vries et al., 2015), which describes the dependency of the AOD on wavelength and gives information on the particle size; the larger the AE, the smaller the particle size (Schuster, 2005).

The AE can be calculated as follows (Penning De Vries et al., 2015):

$$AE = -\frac{log(\tau_{660}/\tau_{470})}{log(\frac{660}{470})} \qquad (1)$$

Where AE is the angstrom exponent, τ is the daily mean AOD for a certain wavelength (660 and 470 nm), 660 is a wavelength of 660 nm and 470 is a wavelength of 470 nm. Penning De Vries et al. (2015) used the 660 nm and 470 nm wavelengths because those were the only channels for which the AOD was determined for land, ocean and bright surfaces at that time (Penning De Vries et al., 2015). However, the AE can also be calculated over other wavelengths. For instance, AERONET uses the 440/870 nm wavelength pair to calculate the AE. Which wavelength pair is best to calculate the AE depends on the information you want to get out of the data. Schuster (2005) mentions that the 670/870 nm wavelength pair has a greater sensitivity for the fine mode fraction than smaller wavelength pairs, while smaller wavelength pairs, like 380/440, are more sensitive for the fine mode

effective radius. The fine mode fraction is the proportion of fine mode aerosols to the total. The effective radius is defined as the average radius weighted with the geometrical cross-sectional area (Schuster, 2005). Therefore, it is better to use larger wave lengths when you want to find the proportion of fine particles while smaller wavelength pairs are better to use for information about the average radius of the aerosols.

UVAI

The second important property for the classification of aerosols is their UV absorbance, which can be determined with the UV aerosol index (UVAI). This index has existed for more than 30 years and has been calculated for several satellite instruments (Stein Zweers, 2018). The first satellite instrument for which the UVAI was calculated was the Total Ozone Mapping Spectrometer (TOMS). It detected the UV-absorbance by aerosols from the spectral contrast between the 340 and 380 nm channels (Herman et al., 1997). The calculation of the UVAI is based on wavelength dependent changes in Rayleigh scattering in the UV spectral wavelength (100-400 nm) (Stein Zweers, 2018). From the top of the atmosphere reflectance, a ratio between a given wavelength pair and the Rayleigh scattering-only atmosphere values is calculated. The resulting ratio gives the UVAI. The UVAI is dependent on the AOD, the aerosol single scattering albedo, the aerosol layer height and the underlying surface albedo (Stien Zweers, 2018).

Carbon monoxide

Besides classification of aerosols, remote sensing images can also be used to estimate the release and sources of BC. Carbon monoxide (CO) is released during combustion of fossil fuels, biomass burning and atmospheric oxidation of methane (Apituley et al., 2018). Since BC is also produced during combustion of fossil fuels and biomass burning, CO is a good proxy for the release and presence of BC. Lalitaporn et al. (2013) studied CO columns for Asia with the use of satellite images. They measured CO values ranging from 0.012 mol/m^2 to 0.058 mol/m^2. They measured the highest values for East China and the Indo-Gangetic plain. The lowest values were measured for the Tibetan plateau.

4 Methods

Field work was performed to collect data in the Langtang Valley (Figure 1). The field work took place from 24-10-2018 till 02-11-2018. During the field work, two data collection methods were used. The first setup used dust collectors with filter bags to determine the deposition rate of dust at the measurement locations. The dust collectors were installed in the field in April 2018 to take measurements over a longer period. The second setup used glass slides with Vaseline to catch wind-blown material to perform a qualitative estimation of the composition and concentration of LAPs. After the field work the collected data were measured and analysed in the lab. Prior to the field work several methods were tested in the lab to determine the best method for the analysis of the samples collected by the glass slides. By combining the information of the dust deposition, measured with the dust collectors, with the analysis of the collected LAPs on the glass slides, estimations of the total mass, types, and concentration of LAPs in the Langtang catchment were made. Wind data, from a weather station at Kyanjin, were used to obtain the main wind direction and wind speed during the field work period, which is an important indication for the direction of the source of the LAPs. Finally, remote sensing data were used to detect the source and distribution of LAPs in the Langtang catchment.

4.1 Field work

Dust collectors

To measure the deposition rate of aerosols in the study area, dust collectors were used (Goossens & Offer, 1994; Riksen et al., 2016). The dust collectors consisted of a plastic funnel (with a diameter of 0.22 m) with a filter bag attached underneath it (Figure 5). In total three funnels were installed, at Kyanjin, Lirung and Langshisha (Figure 1). A layer of marbles was put on top of each funnel (Figure 5). The marbles were used to prevent dust splashing out of the collectors during heavy rainfall (Goossens

et al., 2001). The filter bags under the plastic funnels were used to catch incoming (wet and dry) deposited material and to make a quantitative estimation of dust deposition. Before the filter bags were put in the field, they were weighed. After exchange, the filter bags were dried (Figure 6) and weighed again, to determine the weight of the deposited materials. The filter bags had a pore size of 1 µm. The filters were renewed approximately every month, from April 2018 till October 2018. During the 10-day field work in October/November 2018 the filter bags were collected once for every dust collector. Not every filter bag was in the field for the exact same period. Therefore, the loads of the weighed materials per filter bag were divided by the days the filter bag had been in the field, to get the average deposition rate per day. To derive the average deposition rate per day per unit area, the values were divided by the area of the funnel (0.038 m^2) of the dust collector. This method was carried out for several months to determine if there was seasonality for the deposition of dust. The highest deposition rates in the area were expected for the pre-monsoon period and the lowest values for the monsoon period (Chen et al., 2018).

Figure 5: Dust collector installation. a: Filter bag inside dust collector, b: Dust collector placed in the field, c: Marbles in the funnel of the dust collector

Figure 6: Drying of the filter bags

Glass dust detectors

A second dust collection instrument using glass slides (Cornelis et al., 1997) was installed to determine the composition and concentrations of wind-blown LAPs in the Langtang Valley. Glass slides (76 mm x 26 mm) with a thin layer of Vaseline were used to catch wind-blown and local materials. Vaseline was used because of its water resistance and resistance to temperatures below zero. To apply a fixed amount of Vaseline to each glass slide a measuring spoon of 0.5 ml was used. The Vaseline was equally spread over each glass slide with a knife. The glass slides were attached to a measuring pole in the field. One glass slide was attached vertically and two were attached horizontally, one at the bottom side of the plate of the measuring station and one at the top side of the plate (Figure 7). Table 3 shows the heights and wind directions of the glass slides per measurement location. The slide on the top of the plate catches fall-out materials, whereas the slide at the bottom of the plate catches local materials coming from the area close to the measuring station. The vertical glass slide catches materials coming directly from lateral winds (Cornelis et al., 1997). Three glass slide measuring stations were installed

into the field. They were located at Langshisha, Lirung and Kyanjin (Figure 1). During the October/November field work, the glass slides at Kyanjin were renewed every day. The glass slides at Lirung were renewed at least ones every two days and at Langshisha the glass slides were renewed twice during the field work. The glass slides at Lirung and Langshisha were not renewed every day because of the more difficult accessibility of these locations. All glass slides were in the field for approximately 24-48 hours.

Table 3: Measurement set up specifications of the glass slide measuring stations

Location	Height vertical slide	Orientation vertical slide	Height horizontal slides
Kyanjin	36 cm	West	74 cm
Lirung	28 cm	North	67 cm

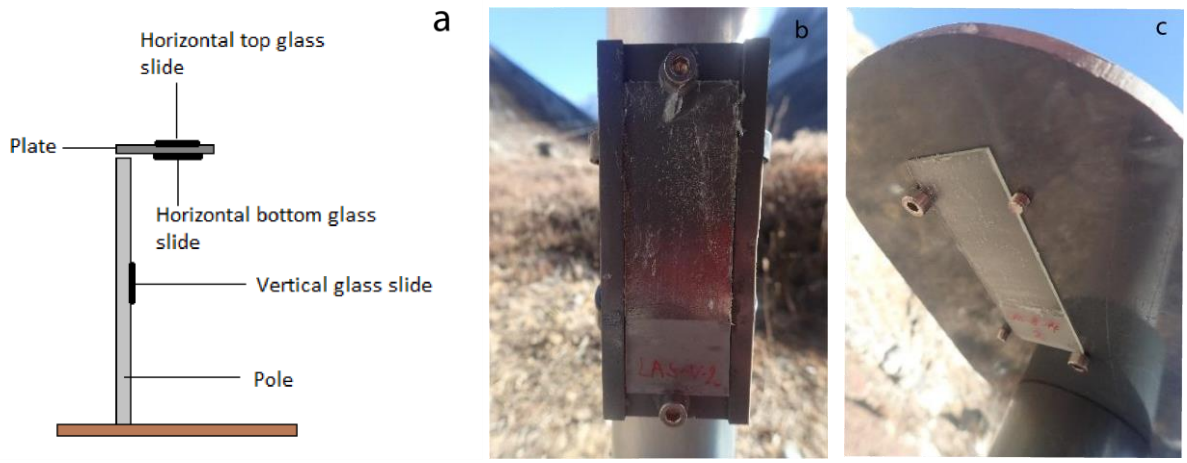

Figure 7: a: measurement station for the glass slides with Vaseline, b: Vertical slide, c: Horizontal bottom slide

4.2 Lab work

Qualitative analysis (coarse LAPs)

Because of the large differences in size between the LAPs in the samples (from < 1 µm up to 1 mm), two analytical techniques were used to classify the LAPs. One technique was used to analyse the coarse LAPs (100 µm-1000 µm), the other method was used to analyse the fine LAPs (1 µm – 100 µm). For the classification of the coarse LAPs a microscope (Leica MDG28 10446350) with a magnification of 10 times was used. The purpose of this method was to classify the coarse LAPs and to determine their concentrations in the samples. From each glass slide, 10 random pictures with an area of 3.8 mm² were made through the microscope with a camera. This camera had a 12-megapixel resolution and a focal length of f/1.7. The photos were used to classify LAPs based on colour and size. Classes that were identified are: transparent silica, silica with brown/black material, small black material, organic material, and large black material (Table 4). The LAPs on the pictures were categorized into these classes and counted, with the use of Image J software (Schneider et al., 2012), to determine the concentrations of the LAPs.

After categorizing and counting the material, the areas of individual LAP particles were measured to establish the average size of the LAPs per class. For 10 random pictures the areas of all present material were measured with the Image J software. The average of the measured areas per class were used to determine the deposition of the LAPs on the glass slides in percentage.

Table 4: Coarse LAPs (100 µm – 1000 µm) at the glass slides and their properties

Material	*Colour*	*Shape*
Transparent silica	Colourless	Irregular
Silica with brown/black material	Transparent with black/brown	Irregular
Small black material	Black	Round or irregular
Organic material	Brown or green	Irregular or plant structure
Large black material	Black	Round, irregular, or clustered material

Extracting samples from the Vaseline

To perform a qualitative analysis for the smaller particles (1 µm – 100 µm) a second, more advanced technique with a Scanning Electron Microscopy (SEM) was used. First the samples were extracted from the Vaseline. There was not yet a protocol available to extract dust samples from Vaseline. Therefore, a method for this has been developed. The methods tested to extract the samples from the Vaseline can be found in Appendix A. The best method was extracting the Vaseline from the samples with WD-40.

To extract the Vaseline from the samples with WD-40 the following protocol was followed:

1. First, the glass slides with the samples were put into a bowl with WD-40 (Figure 8) so that the Vaseline was submerged. The samples were soaked in the WD-40 for 24 hours. Then the bowl was shaken a little until the entire sample, including the Vaseline, was removed from the glass slide.

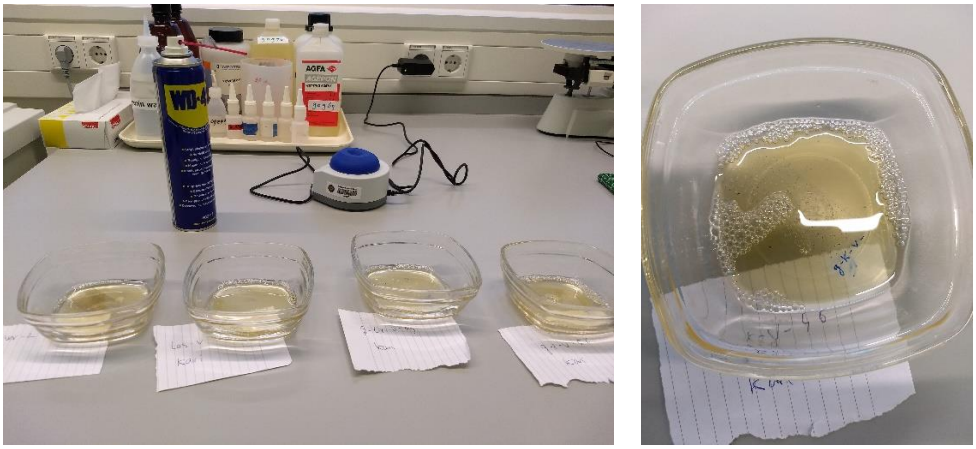

Figure 8: Dissolving of the Vaseline in WD-40

2. The glass slide was removed from the bowl using a tweezer and the glass slide and tweezer were flushed above the bowl with demi-water to make sure that the entire sample was removed from the glass slide and included in the WD-40.
3. The mixture of the sample, Vaseline and WD-40 was put into a 50 ml greiner (a plastic test tube) with the use of a funnel. The bowls and the funnel were flushed with demi-water.
4. The 50 ml greiner was centrifuged at a speed of 2100 rpm (Figure 9). This caused the sample to sink to the bottom of the greiner. Then the fluid on top of the sample was drained. When there was Vaseline/WD-40 sticking to the greiner (above the sample) this was removed with a

paper towel. Demi-water was added to centrifuge again. This process was repeated three times.

5. After centrifuging the samples in the 50 ml greiner three times the sample was put into a smaller glass test tube.
6. This smaller test tube was centrifuged at a speed of 2200 rpm and drained.
7. Then the samples were once again put in a smaller glass tube and centrifuged at a speed of 2200 rpm. The water on top of the sample was carefully removed with a glass pipette.
8. Finally, the samples were put into an oven with a temperature of 40 degrees Celsius for 24 hours to evaporate the remaining water. After this, only the sample remained in the small glass tube.

Figure 9: Centrifuging the samples with the 50 ml greiners

This procedure was done for five different samples, which were analysed under the SEM. All samples used for the SEM analysis were vertically situated slides. These samples were selected based on location (the analysis was done for at least one sample of every location), number of materials on the slide (the samples had to contain enough material), and field notes. Samples with any disturbance in the field were excluded from the SEM analysis. The SEM analysis was only performed for a few samples since the analysis is time consuming and expensive. For the analysis three vertical slides of Kyanjin were used of which two from the field work in October 2018 (samples: g-k-v-9 and g-k-v-56) and one from the field work in April 2018 (sample: k-ver2). From both Lirung and Langshisha one vertical slide of the October 2018 field work (samples: g-lir-v-49 and las-v1) was used for the analysis.

SEM and EDX microanalysis (coarse and fine material)

High-vacuum scanning electronic microscopy (SEM) (JEOL JCOM-6000 Tabletop SEM) was used to determine the size, morphology, and chemical composition of single particles in five samples. A SEM produces images of samples by scanning the surface with a beam of electrons. The SEM combined with energy dispersive X-ray Spectroscopy (EDX) can collect information about the interaction of the electrons from the electron beam with the atoms in a sample. This results in the chemical spectrum of the material, which gives the elemental composition of the material (Stokes, 2008). These spectra show the number of counts on the y-axis and the energy of the X-rays (kEv) on the x-axis. The energy of the X-rays tells which elements are present and the number of counts indicates the concentration of those elements. The location of the peak on the x-axis determines the type of element and the height of the peak on the y-axis is a measure for the concentration for that element.

The analysis with a SEM (Figure 10) was used to determine the presence of smaller particles (<100 µm), like BC, since those particles were too small to detect with the microscope used for the classification of the coarse LAPs. However, some larger particles (>100 µm) were also analysed with the SEM to determine their elemental composition and to support the classifications of the coarse

LAPs. To prepare the samples for SEM and EDX analysis, after they were extracted from the Vaseline, the samples were put on a Carbon sticker and coated with a Platinum coating of 6 nm (Figure 10). Pictures at a large scale (+-200 µm) were made for each sample, approximately 2 pictures per sample. Single particles on these pictures were selected for the SEM/EDX analysis. Then, pictures on a smaller scale (+-50 µm), approximately 2 pictures per sample, were made for each sample. Also, for these pictures single particles were selected for the SEM/EDX analysis. For each selected particle (large and small scale) the SEM/EDX produced a spectrum of the chemical composition. Individual particles were clearly visible on the pictures and as such provided information about the morphology and size of individual particles in the samples. The classification of the particles was based on shape, size and chemical composition obtained from the SEM (Table 5).

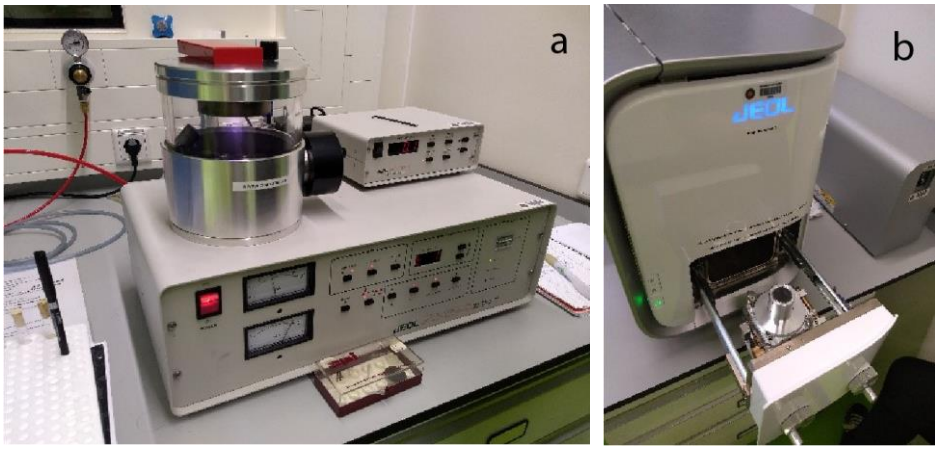

Figure 10: a: Platinum coasting machine, b: Placement of a sample in the SEM

Table 5: Types and properties of aerosol particles (Fan et al., 2016; Cong et al., 2008)

Particle type	Major elements	Minor elements	Morphology
Soot/BC	C	S	Round particles, chain aggregates
Aluminosilicates	AL and SI (>60%)	Na, Mg, K, Ca or Fe	Irregular
Silicates	Si	AL, Na, Mg, K, Ca or Fe	Irregular
Organic	C	Ca, Na, Mg, P or K	Variable morphology
Metals	Fe or Zn	-	Spherical or irregular

4.3 Remote sensing

Large scale remote sensing imagery (Nepal and the Indo-Gangetic plain) was evaluated to detect sources of LAPs that can be linked to aerosol presence in the Langtang Valley. The aim of this evaluation was to determine if aerosols emitted from areas further away, for instance the Indo-Gangetic plain, can reach the Langtang catchment and to see if these higher aerosol values can be identified in the field measurements. For this detection the UV aerosol index (UVAI) and carbon monoxide (CO) images, products from Sentinel-5 TROPOMI (Copernicus Sentinel-5P Data hub. 2018), were used. The Sentinel-5 satellite delivers daily products with a resolution of 3.5 x 7 km. The swath width of the satellite is 2600 km. Data from these products show the daily CO and UV-absorbing aerosol values in the air.

From the UVAI the absorbing aerosol index (AI) was derived, which is the final interpretation of UVAI data (Stein Zweers, 2018). When the AI is positive, it indicates the presence of aerosols that absorb UV radiation, like BC and dust. A negative AI indicates aerosols which do not absorb UV radiation, like sea salt and sulphates (Torres et al., 1998). Clouds give a near-zero value for the AI. These properties make the AI a good measure to detect the presence, origin, and transport of LAPs. CO data were used because CO is released during fossil fuel and biomass burning (Copernicus Sentinel-5P Data hub. 2018), which are the same processes for the emergence of BC. This makes CO a good

proxy to detect events whereby BC is released. By interpreting data from these products for the field work period the presence of events and the distribution of these events was determined. Additionally, it was determined if the aerosols from such events could reach the Langtang Valley.

Data on the size of aerosols were obtained from the angstrom exponent (AE). The AE describes the dependency of the AOD on wavelength and gives information on the particle size; the larger the AE, the smaller the particle size (Aerosol Angstrom Exponent, NASA, 2006). Penning De Vries et al. (2015) defined large particles as AE<0.75, medium size particles as 0.75<AE<1.25 and small particles as AE>1.25. The AE was established from Aerosol Robotic Network (AERONET), which delivers the AE as a product calculated from the aerosol optical depth (AOD), which is also a product from AERONET. AERONET delivers ground-based remote sensing aerosol data (AERONET system description, 2017). The system provides continuous and readily accessible aerosol data. The AOD data from AERONET are derived from sun photometer measurements of the direct solar radiation (Aerosol optical depth EARONET. 2018). Kyanjin (figure 1) has an AERONET station (Figure 11) which delivers these AOD data at Kyanjin (AERONET AOD data Kyanjin_Gompa, 2018). The AE data from AERONET are calculated from the 440/870 wavelength pair. Additional, larger scale AOD data for the pre-monsoon and post-monsoon form MODIS were used to compare the AOD measurements at Kyanjin with AOD values at possible source areas.

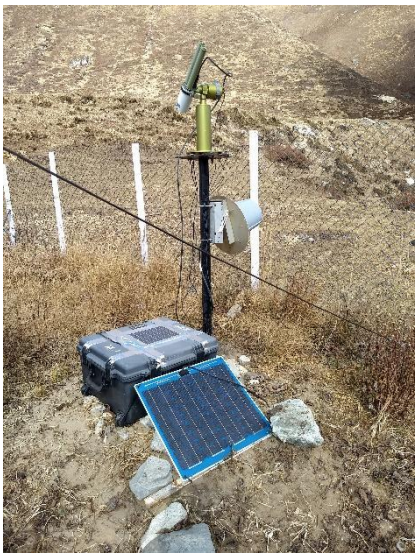

Figure 11: AERONET station at Kyanjin

5 Results

5.1 Wind data

Wind measurements for the field work period were obtained from a weather station at Kyanjin. The wind data show a diurnal pattern which is stable during the entire field work. The wind speed peaked every day during the early afternoon (12:00-17:00) (Figure 12). Wind speeds reached 7-8 m/s during this time of the day. The lowest wind speeds were observed during the night and early morning. For this time of the day the wind speed varied between 0 and 2 m/s. There were up-valley winds during the day and down-valley winds during the night. This is a typical wind pattern for high mountain areas caused by thermal winds. The main wind direction during this part of the day was approximately 75 degrees (Figure 12), which is an east-north-eastern wind. The main wind direction during the day time, when the wind speed was the highest, varied a little but was on average 250 degrees, which is a south-western wind. Therefore, most material on the samples is expected to come from a south-western direction.

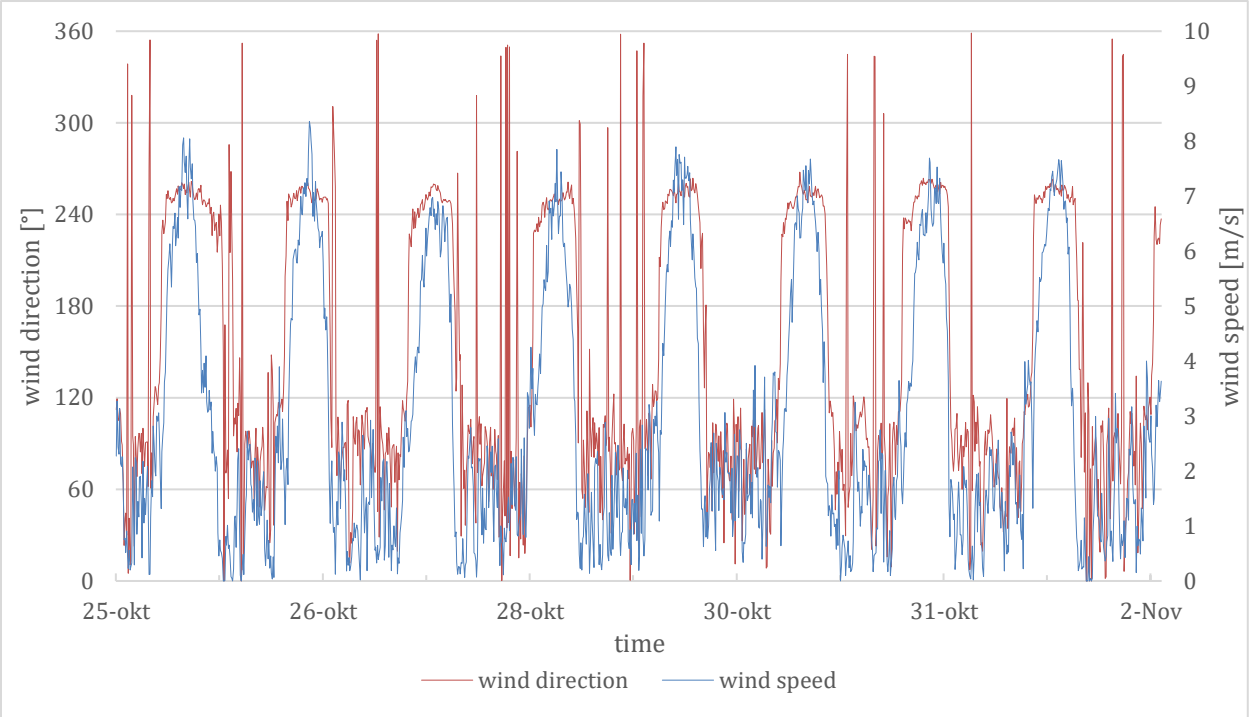

Figure 12: Wind direction and speed at Kyanjin during the field work period

5.2 Field data

LAP composition and concentrations

Coarse LAPs (100 µm - 1000 µm)

Figure 13 shows an example of a picture made of a glass slide sample under the microscope. This example is very dense covered and it contains an example of each LAP class. The complete dataset of the classification, derived from the pictures made under the microscope, can be found in appendix D. This appendix includes the estimated amounts for each class per picture. Every picture covered a circular area of 3.8 mm^2. Appendix C contains the field data of the glass slides, including the period a glass slide was in the field and special notes.

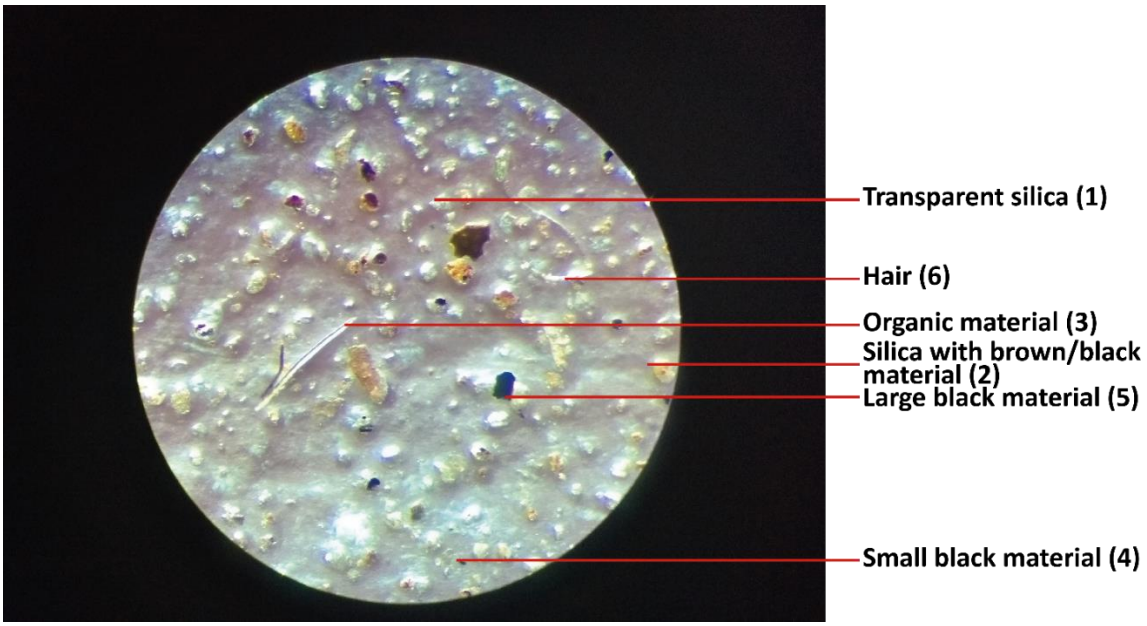

Figure 13: Example of one picture made of a glass slide sample (g-k-v-92-2) under the microscope

The coarse LAPs were classified into 5 classes: transparent silica (1), silica with brown/black material (2), organic material (3), small black material (4), and large black material (5). Black materials smaller than 1.0E-3 mm^2 were classified as small black material and black materials larger than 1.0E-3 mm^2 were classified as large black material. Besides these classes, 17 samples contained (yak) hairs and 6 samples contained small blue materials. However, because of low concentrations in the samples for these materials and their unknown influence on the albedo of snow and ice they will not be further discussed. The small and large black materials are potential BC.

The composition of LAPs at Lirung and Langshisha was almost the same (Figure 14). 88% of the classified material here consisted of transparent silicas, 6% of the LAPs consisted of organic material, 3 to 5% was small black material and the rest consisted of silica with brown/black material and large black material. Kyanjin had lower percentages of transparent silica (77%) and more organic material (11%) and silicas with brown/black material (7%). The contribution of small and large black materials was the same for all three locations.

The largest area on the glass slides was covered by transparent silicate, followed by organic material, silica with brown/black material, small black material and, large black material (Figure 15). This sequence of coverage by LAP class is the same for all three measurement locations. For all three locations the vertical slides caught the highest concentration of LAPs, followed by the horizontal top slides and the horizontal bottom slides. Kyanjin and Langshisha show a pattern where the vertical slides caught 3 to 8 times higher concentrations of LAPs than the horizontal top slides, this pattern applies for every class (Figure 15). Furthermore, the horizontal top slides caught slightly higher concentrations of LAPs than the horizontal bottom slides (+- 0.1 to 0.3 %). At Lirung the vertical slide only caught slightly more LAPs than the horizontal top slides (+-1.2 %). Although Kyanjin and Langshisha show the same pattern for the vertical and horizontal slides (Figure 15), Kyanjin has higher concentrations of LAPs than Langshisha. For the horizontal slides, Kyanjin and Lirung show the same values in concentrations of LAPs. The horizontal top and bottom slides at Langshisha contain less LAPs than the horizontal top and bottom slides at Kyanjin and Lirung.

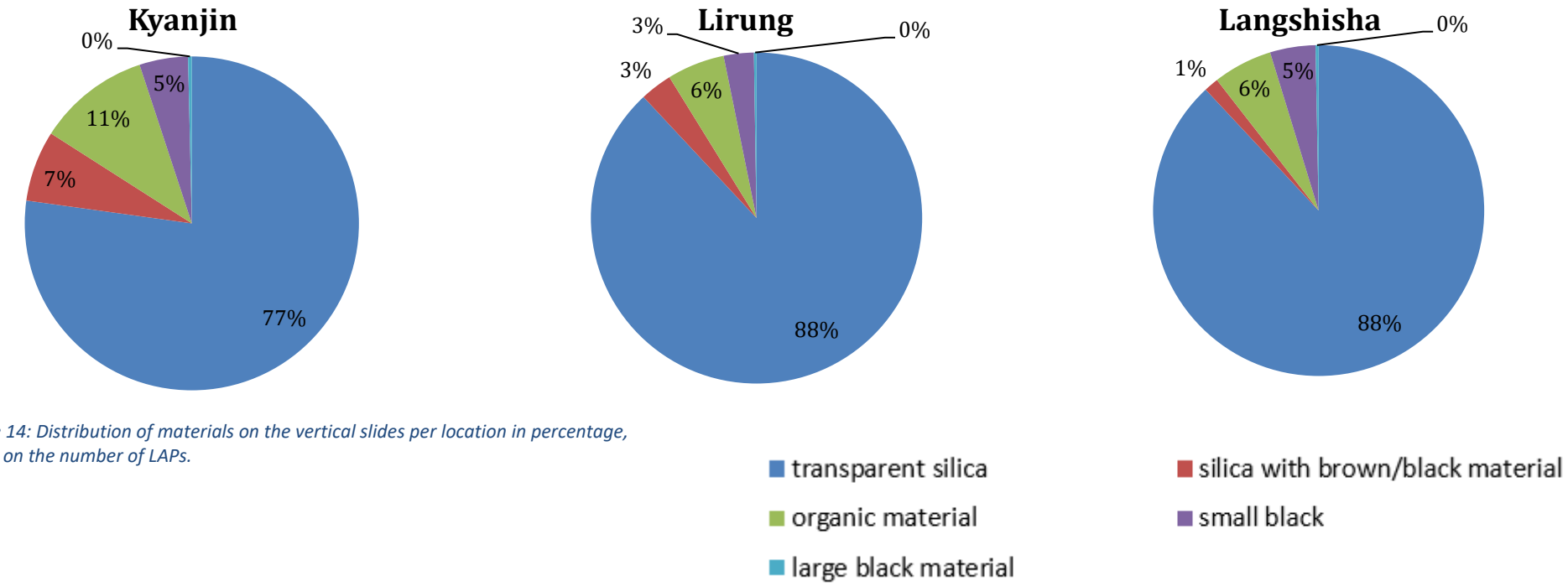

Figure 14: Distribution of materials on the vertical slides per location in percentage, based on the number of LAPs.

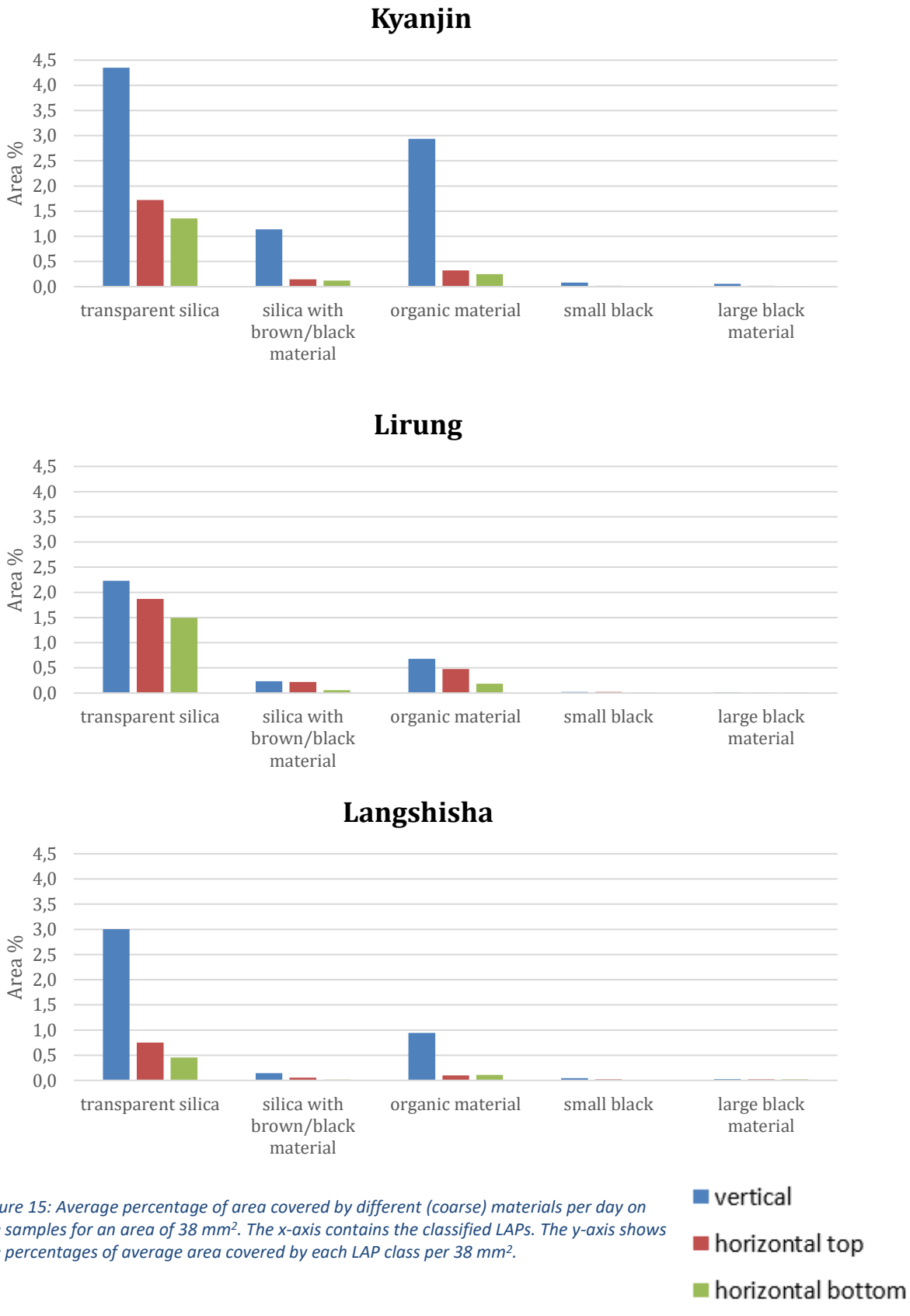

Figure 15: Average percentage of area covered by different (coarse) materials per day on the samples for an area of 38 mm². The x-axis contains the classified LAPs. The y-axis shows the percentages of average area covered by each LAP class per 38 mm².

Fine materials (1 µm - 100 µm) SEM

Table 6 shows the classification of the particles analysed with the SEM. In total 73 particles were randomly selected from 5 different glass plates at the three sites and analysed. Because of the low number of particles analysed, it is not possible to determine the concentrations of the classified material in the samples. However, particles classified as aluminosilicates, organic material, silica, and metals were detected several times in the samples while calcium and BC were only detected once or twice. Therefore, it can be assumed that calcium and BC had a much lower concentration in the samples than the other classes.

Table 6: Classification of selected particles under the SEM

	Glass slide Samples					
(Fine) materials	**g-k-v-9 (Kyanjin)**	**g-k-v-56 (Kyanjin)**	**k-ver2 (Kyanjin)**	**g-lir-v-49 (Lirung)**	**Las-v1 (Langshisha)**	**Total**
Aluminosilicates	2	6	8	9	2	**27**
Organic	4	1	2	5	9	**21**
Silica	3	1	4	5	1	**14**
Metals	1	0	3	2	2	**8**
Calcium	0	0	1	0	0	**1**
Black Carbon	0	1	0	0	1	**2**
Total	**10**	**9**	**18**	**21**	**15**	**73**

Below, an example for each classified material is given. The complete data set of all particles classified with the SEM analysis are added in Appendix E. The analysed particles in the pictures can be recognized by the numbers on the pictures, these numbers correlate with the numbers in the upper left corner of the chemical spectra. The chemical spectra show the identified elements for the selected particle. Some samples contain platinum according to the measurements. Although platinum could be present in some particles, these measurements are neglected since the samples were coated with a platinum coating.

Aluminosilicates

Figure 16 shows an aluminosilicate (Al_2SiO_5) with the corresponding chemical spectrum. Aluminosilicates mainly consist of aluminium (Al) and silica (Si) (Al + Si > 60%) (Cong et al., 2008). Besides these main elements, aluminosilicates can contain trace elements natrium (Na), magnesium (Mg), potassium (K), calcium (Ca) or iron (Fe) (Cong et al. 2008). These trace elements can attach to the negative area of the clay particles because of their positive charge. The classified aluminosilicates varied in size from 5 to > 200 µm (Appendix E). The morphology of aluminosilicates looks like the silicates; therefore, the chemical spectra are essential to distinguish the aluminosilicates from the silicates.

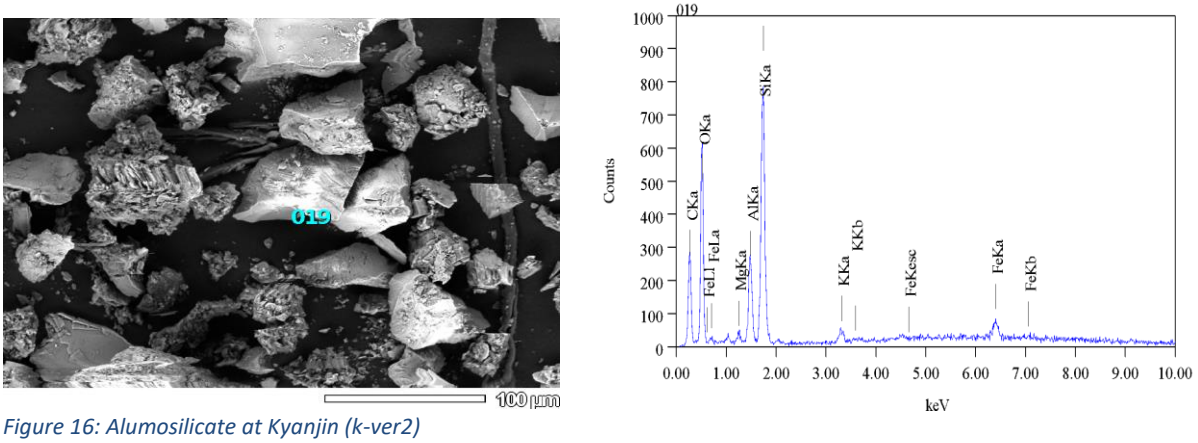

Figure 16: Alumosilicate at Kyanjin (k-ver2)

Silica

Figure 17 shows an example of a silica particle. The classified silicates were irregular in shape, varied in size from 2 µm to 100 µm and mainly consisted of silica elements. The silicates look very similar to the aluminosilicates on the pictures, however, the chemical spectra do not contain the positive charged ions (natrium (Na), iron (Fe) etc.) which are typical for aluminosilicates. Silica was very common in the samples (Appendix E). This corresponds with the high concentrations of transparent silicas measured under the microscope for the coarse materials.

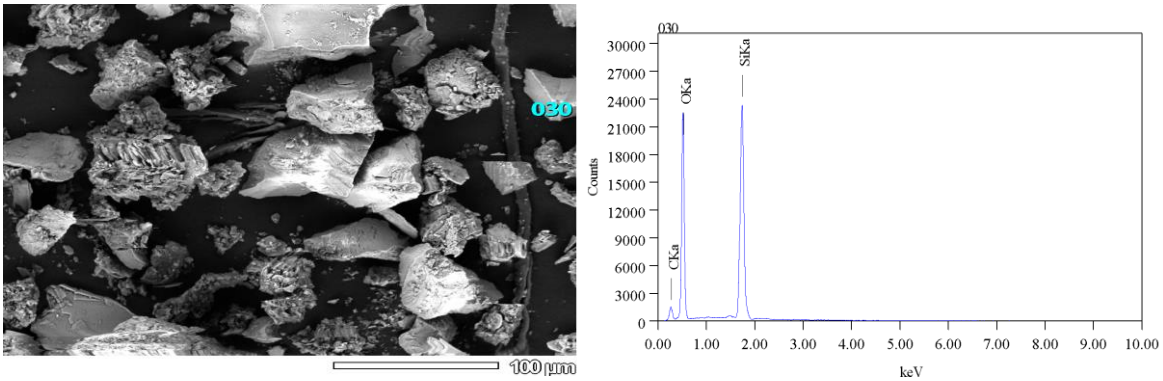

Figure 17: Silica particle at Kyanjin (k-ver2)

Organic material

The organic material was mainly classified based on high contents of carbon (C) (Figure 18). The organic material in the samples widely varied in shape and size (2 µm to 250 µm). Some of them had a small elongated shape while other organic materials were irregular in shape. This is caused by the variety in sources for the organic material. The material can originate from animals (yaks) or plants (grass).

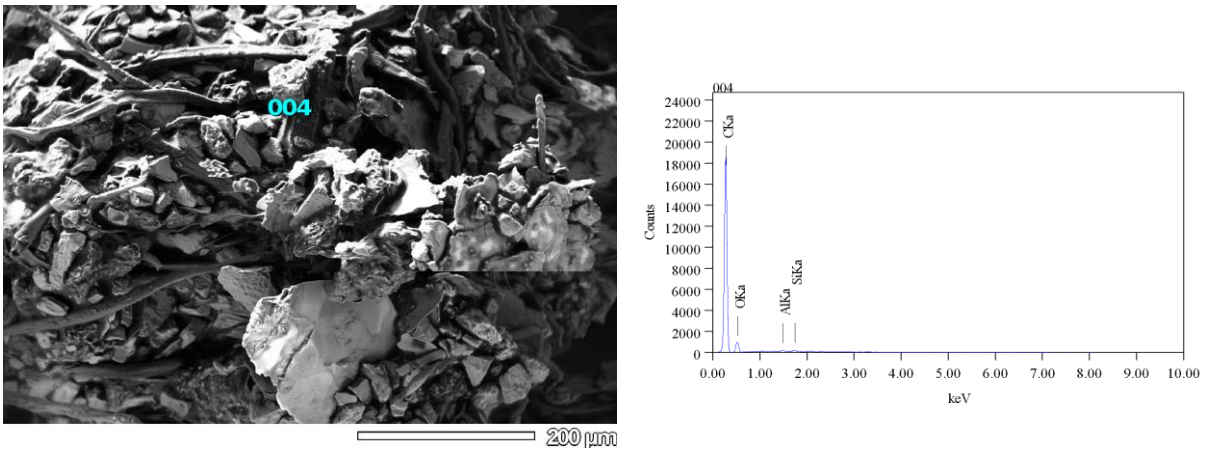

Figure 18: Organic material at Langshisha (las-v2)

Metals

Metals were classified based on high contents of iron (Fe), tin (Ti) or zirconium (Zr). Iron was the most abundant metals in the study area. Most metals contained Iron (appendix E). Two metal particles contained tin and one particle contained zirconium. Tin and zirconium were only present in metal particles collected at Lirung. The metals collected at Kyanjin and Langshisha only contained iron. Figure 19 shows the image and the chemical spectrum of an (iron) metal particle collected at Lirung. Most metal particles were irregular in shape with angular features (
Figure 19). The size of metal particles in the samples varied from 5 µm to 50 µm.

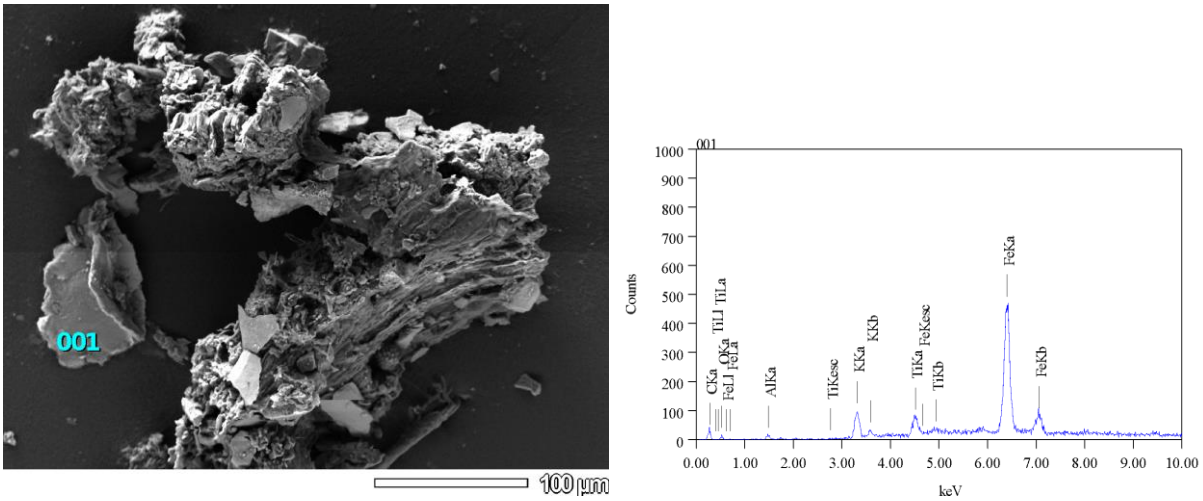

Figure 19: Metal particle at Lirung (g-lir-v-49)

Ca-rich particles

One outstanding particle from a sample at Kyanjin, was a Ca-rich particle. This particle is shown in Figure 20. Even though, only one Ca-rich particle was discovered, it is still worth mentioning since Ca-rich particles were also measured during other studies in the high Himalaya (Cong et al., 2008). The shape was elongated and small. Besides calcium, the particle consisted of small amounts of carbon, aluminium, silica, and iron. Despite the presence of these elements in the particle, the particle is still classified as a Ca-rich particle, because of the high calcium concentration. This high concentration of calcium was not measured in any of the other SEM analysed particles.

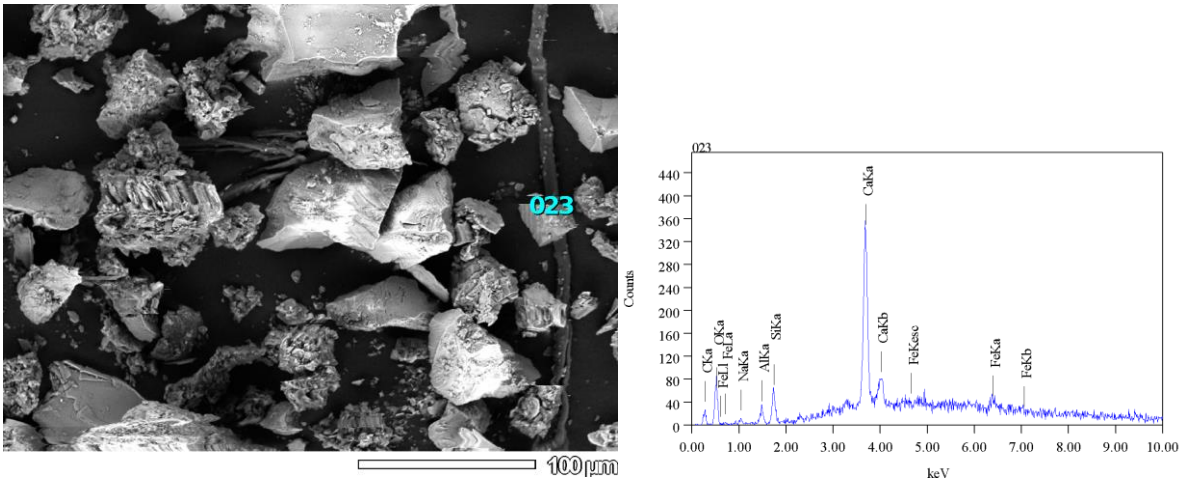

Figure 20: Ca-rich particle at Kyanjin (k-ver2)

Black Carbon (BC)

Two particles of the SEM analysis were classified as BC. One in a sample at Kyanjin and one at Langshisha. These particles were classified as BC because of their round shape, small size (20 µm – 25 µm) and their chemical composition of mainly carbon and a minor fraction of sulphur (Figure 21).

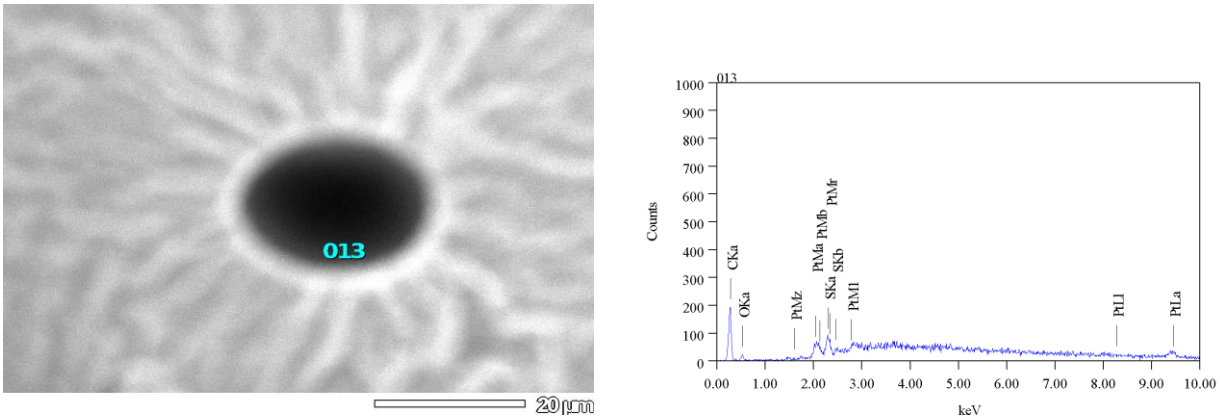

Figure 21: BC particle at Langshisha (las-v13)

Dust deposition

Figure 22 and Figure 23 show the dust deposition rates measured with the dust collectors at Kyanjin and Lirung. At Langshisha only two measurements were taken. Therefore, these data were not used for this study. The collected data at Langshisha are included in appendix B3. Appendix B1-3 contains information about the weight of the caught dust per measurement, the period a measurement took place, the average amount of dust collected per day per measurement and special notes for each measurement. The graphs in Figure 22 and Figure 23 show the average dust deposition and its seasonality at Kyanjin and Lirung.

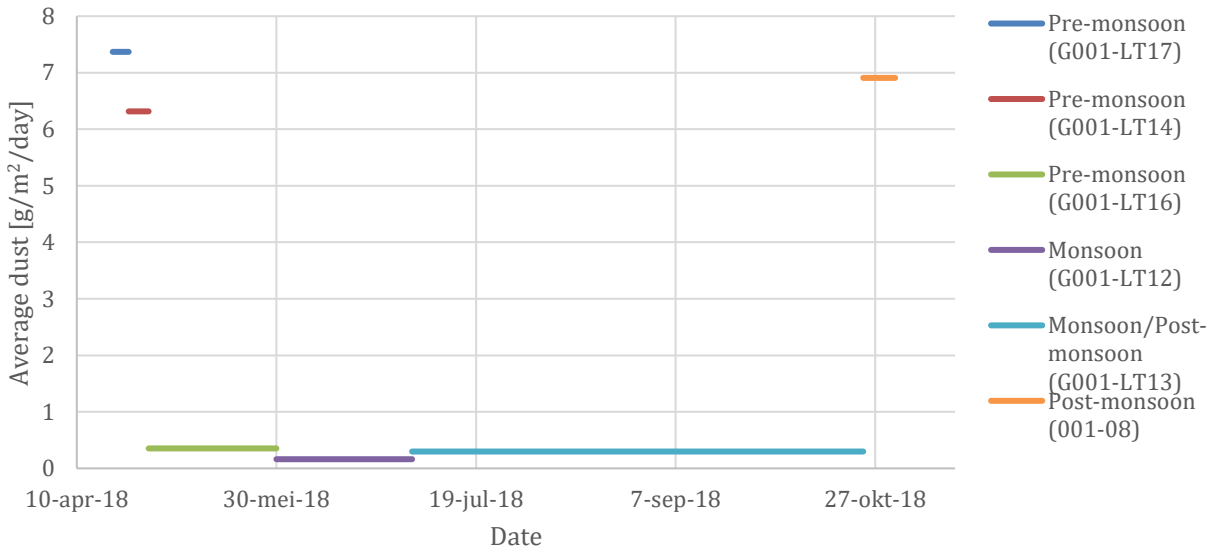

Figure 22: Average dust deposition at Kyanjin over time. Each colour represents a dust measurement, the average time it was in the field and the average deposited dust per day. The y-axis shows the average dust deposition rate per day for a measurement period and the x-axis shows the period of a measurement.

The measurements at Kyanjin (Figure 22) show high deposition rates for April and November and low dust deposition rates from May till October, with the lowest value for June. This is in accordance with the expected high dust deposition rates for the pre-monsoon and post-monsoon seasons and low dust deposition rates for the monsoon season. Only measurement G001-LT13 (monsoon/post-monsoon) was collected over a long period (July till October) during the monsoon and post-monsoon period. Therefore, this measurement is harder to interpret. Furthermore, it seems measurement G001-LT16 is too low for a pre-monsoon dust deposition rate. However, this

measurement was taken over a longer period and at the end of the pre-monsoon/start of the monsoon period which could have caused this lower value.

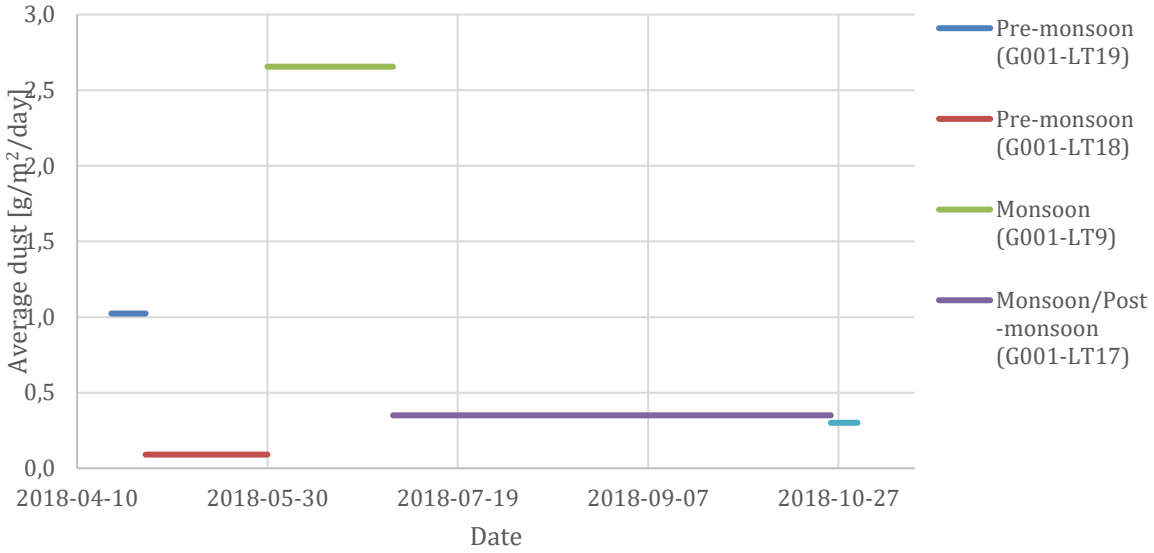

Figure 23: Average dust deposition rate at Lirung over time. Each colour represents a dust measurement, the average time it was in the field and the average deposited dust per day. The y-axis shows the average dust deposition rate per day for a measurement period and the x-axis shows the period of a measurement.

The highest dust deposition rates at Lirung (Figure 23) were much lower than the highest dust deposition rates at Kyanjin. The highest average dust deposition rate for one day at Kyanjin was almost three times higher than for Lirung, while the lowest deposition rates (<0.5 g/m^2/day) were approximately the same for both areas. Therefore, the variability in deposition rates at Lirung was smaller than for Kyanjin. Additionally, the dust deposition at Lirung did not show the typical seasonality of high deposition during the pre- and post-monsoon seasons and low deposition during the monsoon season, as was expected. The highest daily dust deposition rates were even during the monsoon season (measurement G001-LT9).

5.3 Remote sensing data

Dust source and distribution

Figure 24 shows high CO values at most days for North-North-West India, North-East Pakistan and Bangladesh. For these areas the CO concentration was often above 0.065 mol/m^2. This are locations with high population densities where high pollution values can be expected. Furthermore, when the topography of the Himalaya (Figure 25) and the CO (Figure 24) are compared, there is a clear correspondence between the Himalaya mountain ridge and the CO concentrations. It is striking that the CO concentrations peak at the Indo-Gangetic plains and in front of the Himalaya. Most days the CO reaches Nepal but does not penetrate into the mountains. The data show that the study area has low CO values of around 0.020 mol/m^2. The pattern of CO concentrations is simular for all days during the field work period.

Vertically integrated CO column 2018-10-24

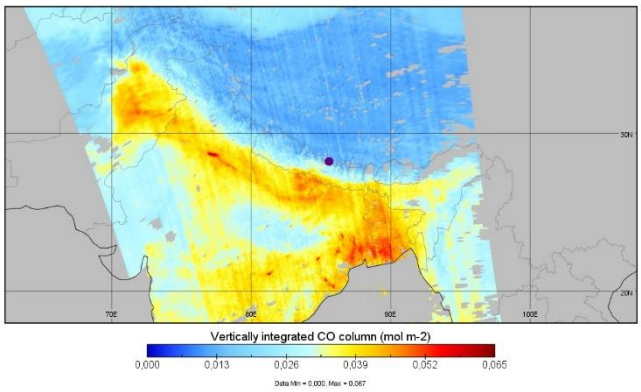

Vertically integrated CO column 2018-10-25

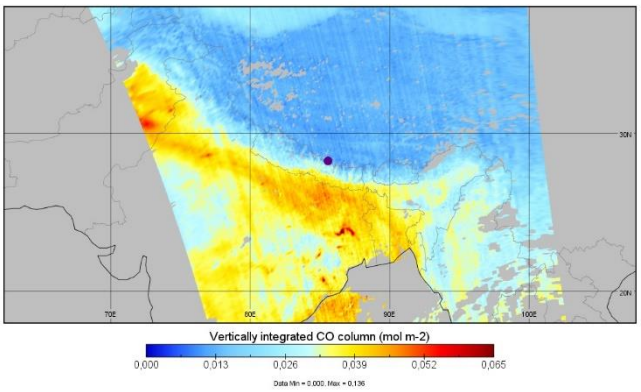

Vertically integrated CO column 2018-10-26

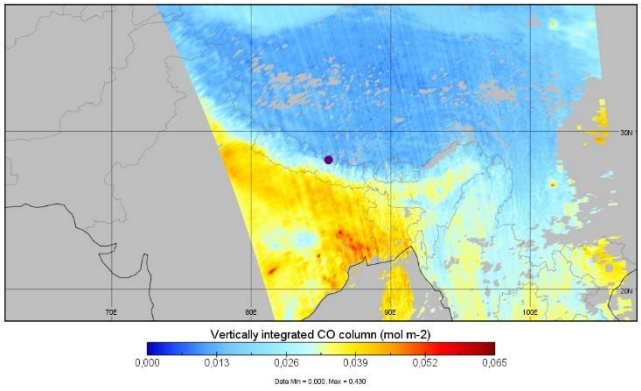

Vertically integrated CO column 2018-10-27

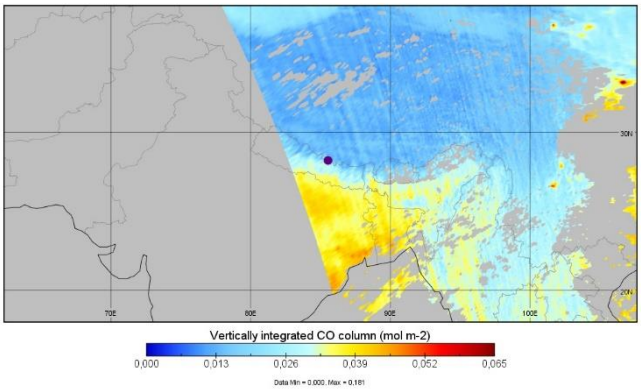

Vertically integrated CO column 2018-10-28

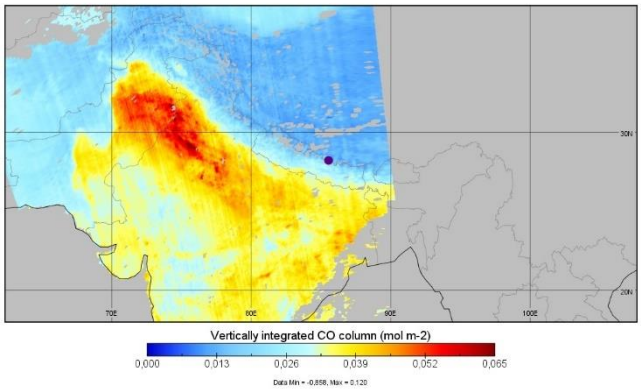

Vertically integrated CO column 2018-10-29

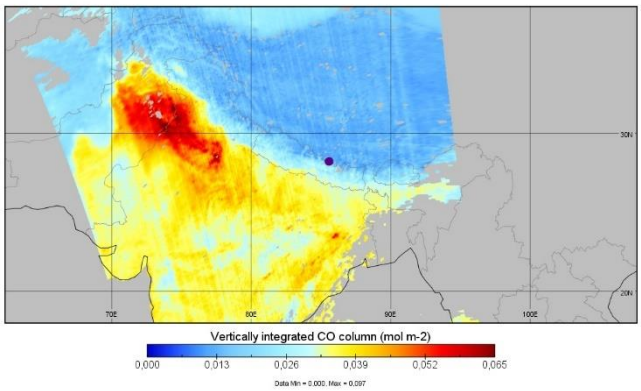

Vertically integrated CO column 2018-10-30

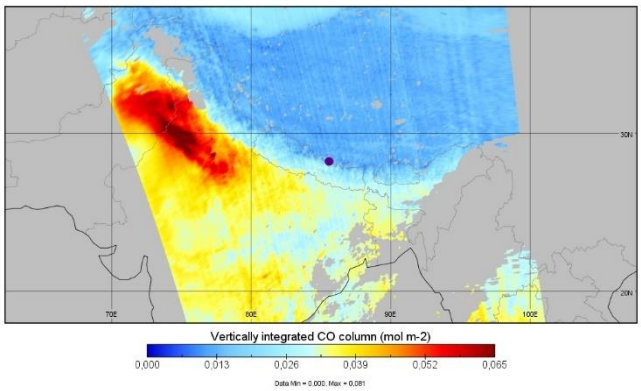

Vertically integrated CO column 2018-10-31

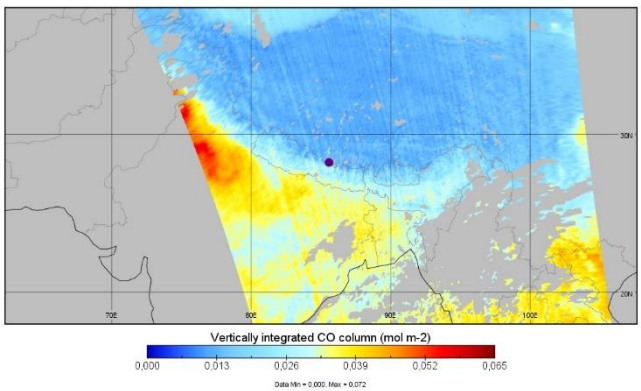

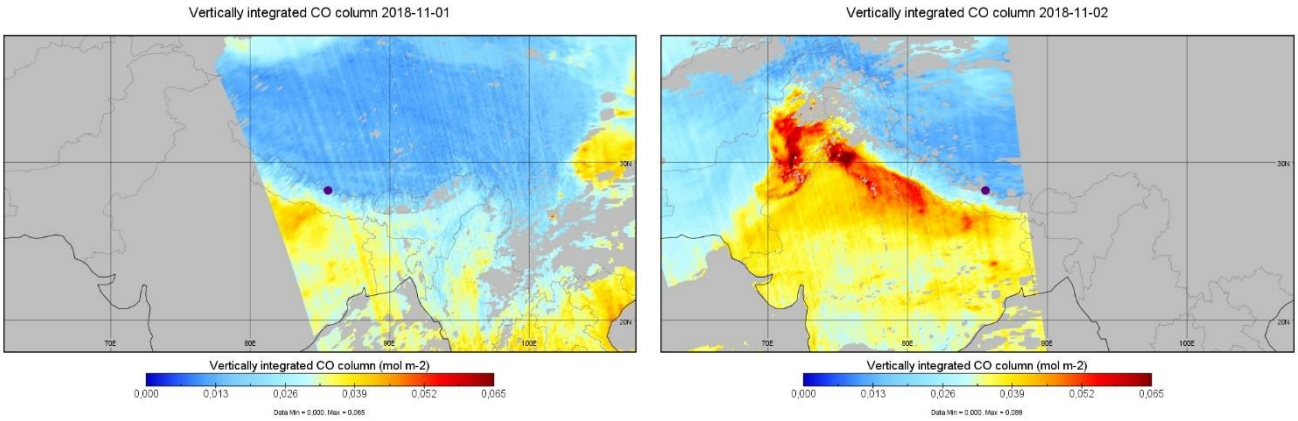

Figure 24: CO columns for 24 October 2018 till 02 November 2018. Images are every day from 01:30 PM. The purple dots show the location of the Langtang Valley (Source: Copernical Sentinel-5P Data hub (2018))

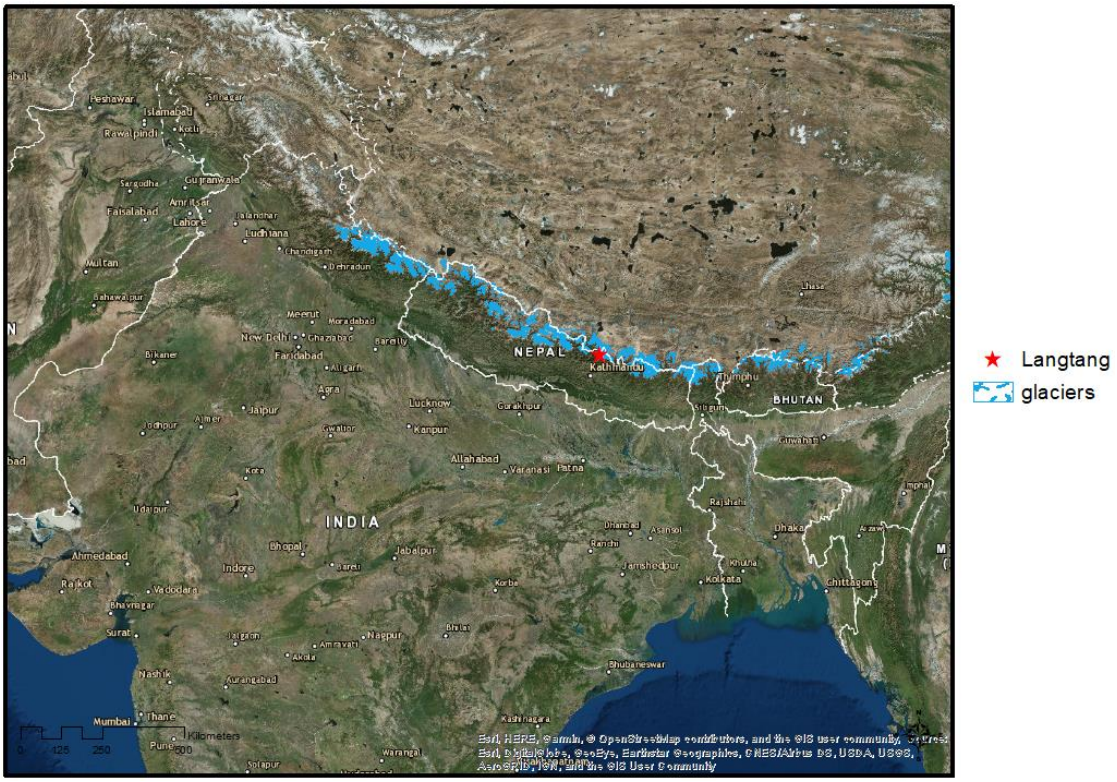

Figure 25: Topography of the area analysed with satellite images of CO and AI

Figure 26 shows large scale aerosol index data for the field work period. Positive values for the UVAI are an indication for aerosols that absorb light, zero values are an indication for clouds and negative values are an indication for light-reflecting aerosols (Stein Zweers. 2018). The images show the presence of LAPs north from the study area on the Tibeatan plateau for every day. In the Langtang Valley the UVAI is predominatly negative. The supply of LAPs from the Indo-Gangetic plain, as expected according to literature and from the CO data, is not visisble in the images. The correspondance between the CO values and the UVAI is low. The UVAI shows high values at the location of the Thar dessert in Norht-West India/Pakistan. Therefore, it is assumed that the UVAI mostly responds to dust. Another cause for the low correspondance between the CO and UVAI could be higher values for light-

reflecting aerosols than for light-absorbing aerosols at the Indo-Gangetic plain, since the CO data do not include light-reflective aerosols.

A notable feature in the images, is the high value for the UVAI, North-West of the study area. At this location high values for the UVAI are present on the 24th , 25th , 29th , 30th , and 31st of October and on the 1st and 2nd of November. At this location a salt lake is present which could have caused this unusual high value. For most days the UVAI has negative values for the study area. Only at the second of November there are positive values present at the study area. The area close to the study area also has higher values for this day compared to the other days of the field work.

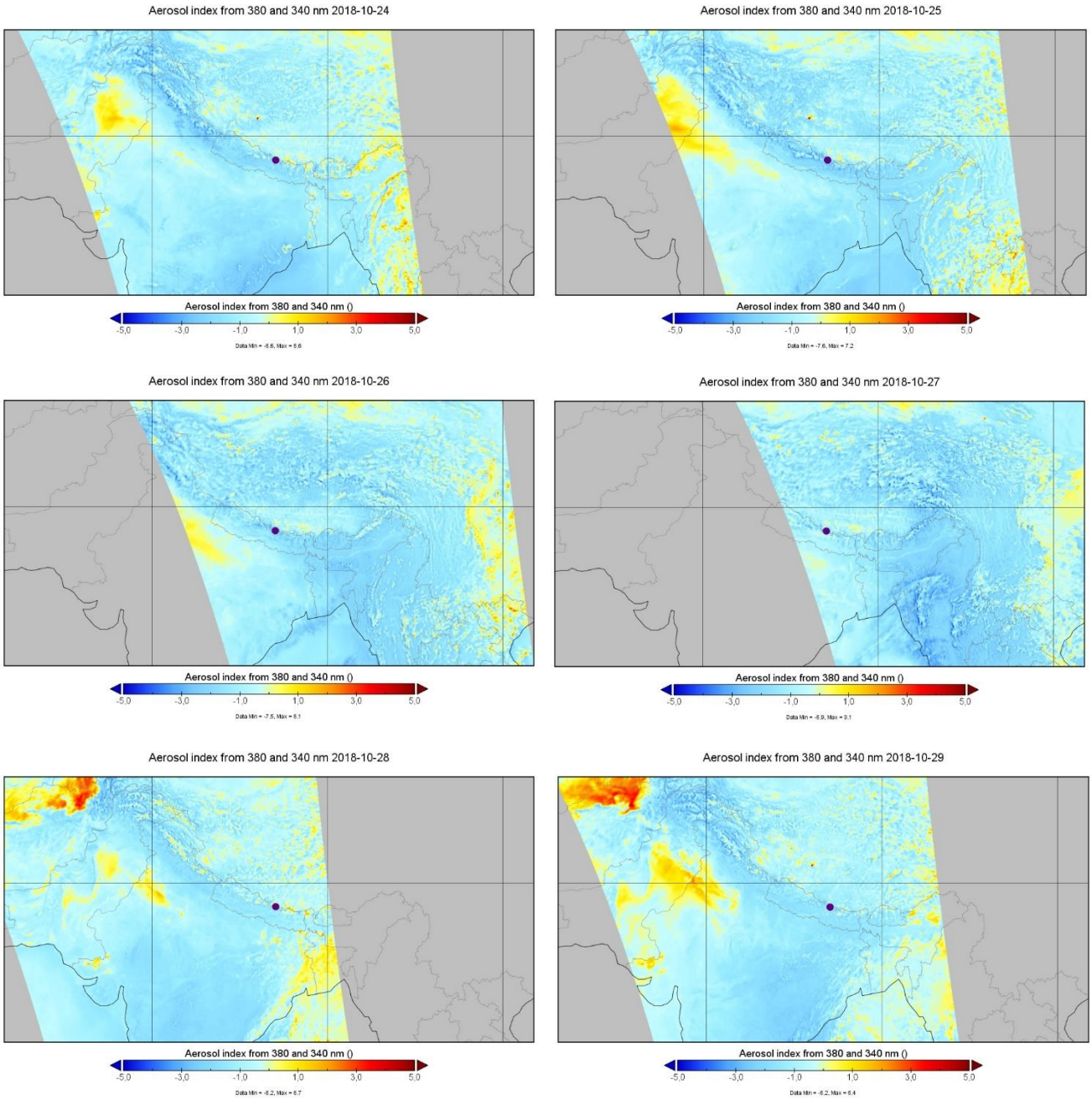

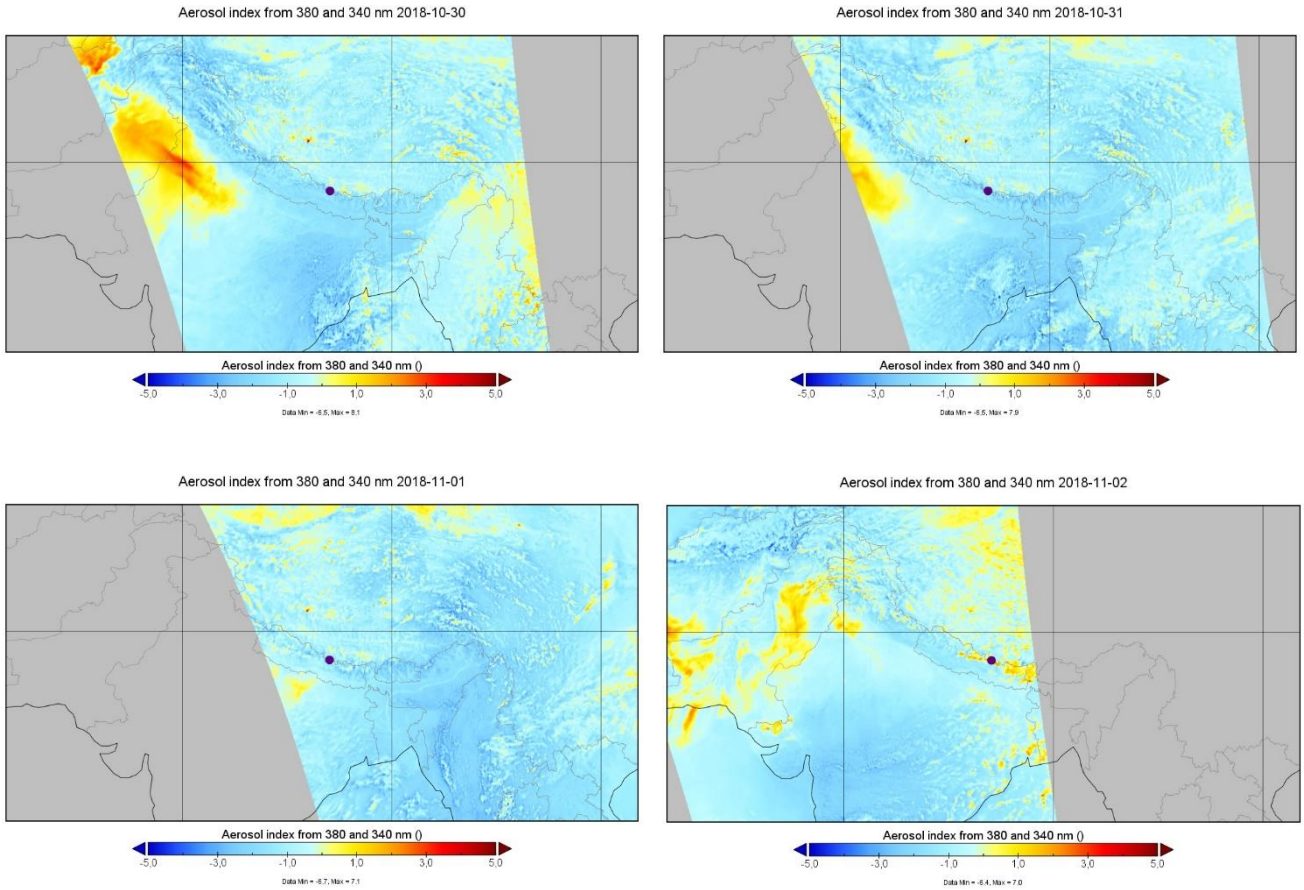

Figure 26: Aerosol index for 24 October 2018 till 02 November 2018. Images are every day at 01:30 PM. The purple dots show the location of the Langtang Valley. (Source: Copernicus Sentinel-5P Data hub (2018))

The Angstrom exponent varies from 0.2 to 1.5 for the field work period (Figure 27). However, for most days, the Angstrom exponent lies between 0.8 and 1.2. This indicates that the measured aerosols at Kyanjin these days were of medium size (Literature review 3.3). Medium LAPs can consist of both smoke and dust. From the 28th till the 30th of October lower AE values were measured. This indicates that larger aerosol particles (dust) were present for these days.

The AOD data at Kyanjin show low values for the entire field work period (Figure 27). The highest values were around 0.16, which are still relatively low values. This indicates that low aerosol concentrations were present during the field work period. To compare the values of the field work (post-monsoon season) with the pre-monsoon and monsoon seasons, the AODs from April and June 2018 are also included. The data show, as expected, higher AOD values for the pre-monsoon season. The AOD at Kyanjin for April has a few peaks of 0.3, which are high values for the AOD. The measured AOD for June is approximately the same as for the post-monsoon, while lower values were expected for the monsoon season. However, for the monsoon period only a few data points are present. Clouds and heavy monsoon rains possibly disturbed the data. Nonetheless, another explanation could be that the post-monsoon of the field work had relatively low values for a post-monsoon season. This last statement is supported by AOD data from MODIS (Figure 30 and Figure 30). These data show high AOD values for North-India and North-Pakistan but low values for the study area. Like the CO data, the AOD decreases along the Himalaya ridge. However, this only applies for the average AOD from 24 October till 28 October (Figure 29). The data from 23 April till 30 April (Figure 30) show that the AOD is also high at the Himalaya mountain ridge, which corresponds with the high AOD measured by AERONET for this period. However, AOD data from MODIS for the study area are missing.

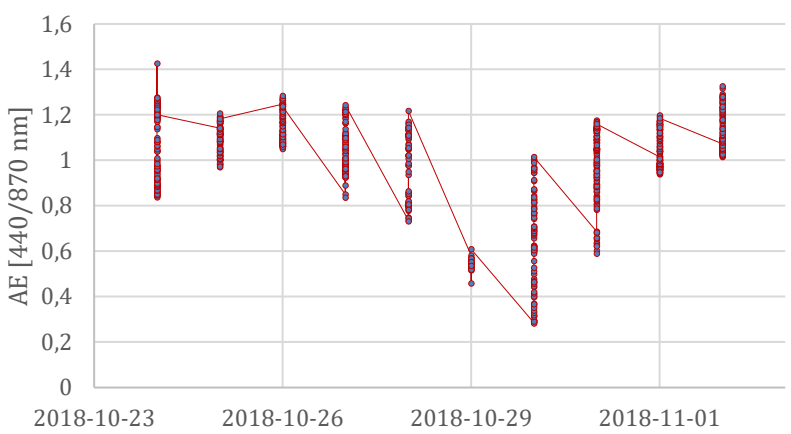

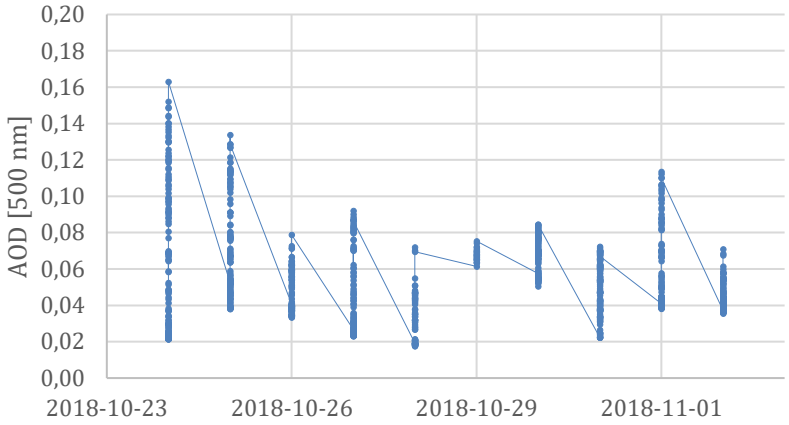

Figure 27: Left: Angstrom exponent (440/870 nm wavelength) for the field work period (2018-10-24 till 2018-11-02) at Kyanjin; Right: Aerosol optical depth (wavelength 500 nm) for the field work period (2018-10-24 till 02-11-2018) at Kyanjin

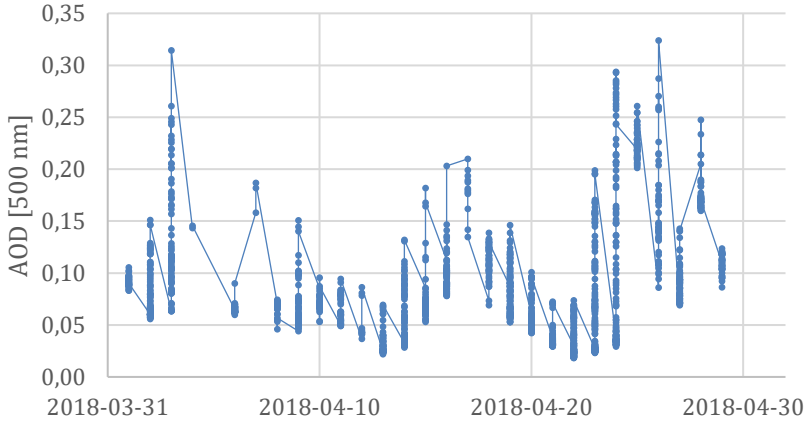

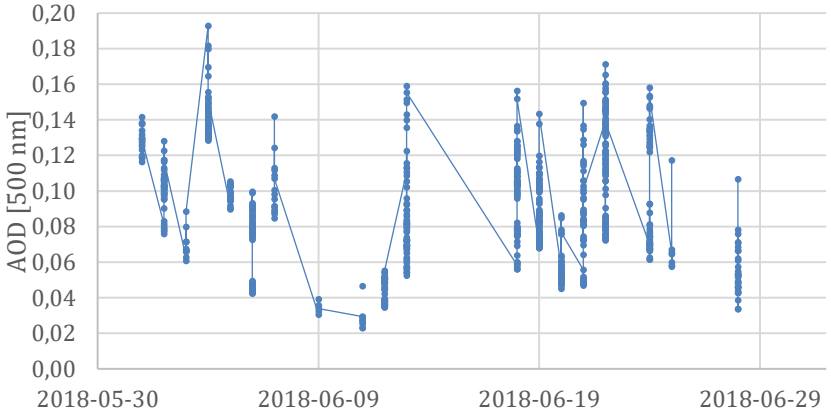

Figure 28: Left: Aerosol optical depth, for a wavelength of 500 nm, for April 2018 (left) and June (right) at Kyanjin

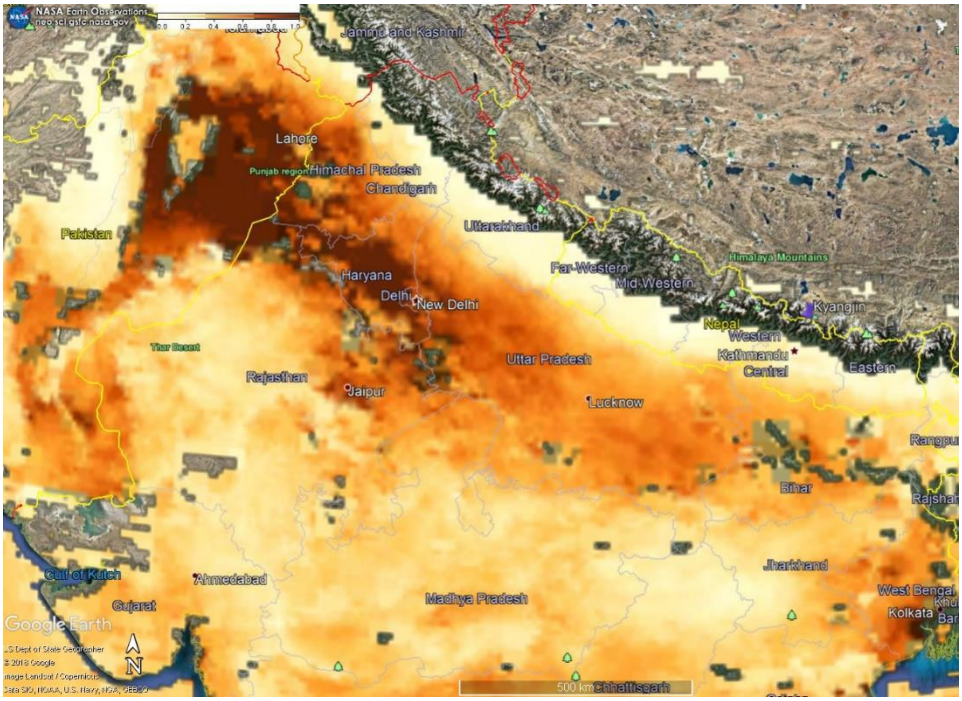

Figure 29: Average AOD data from 2018-10-24 till 2018-10-28 from MODIS (source: https://neo.sci.gsfc.nasa.gov/view.php?datasetId=MODAL2_E_AER_OD&date=2018-11-01)

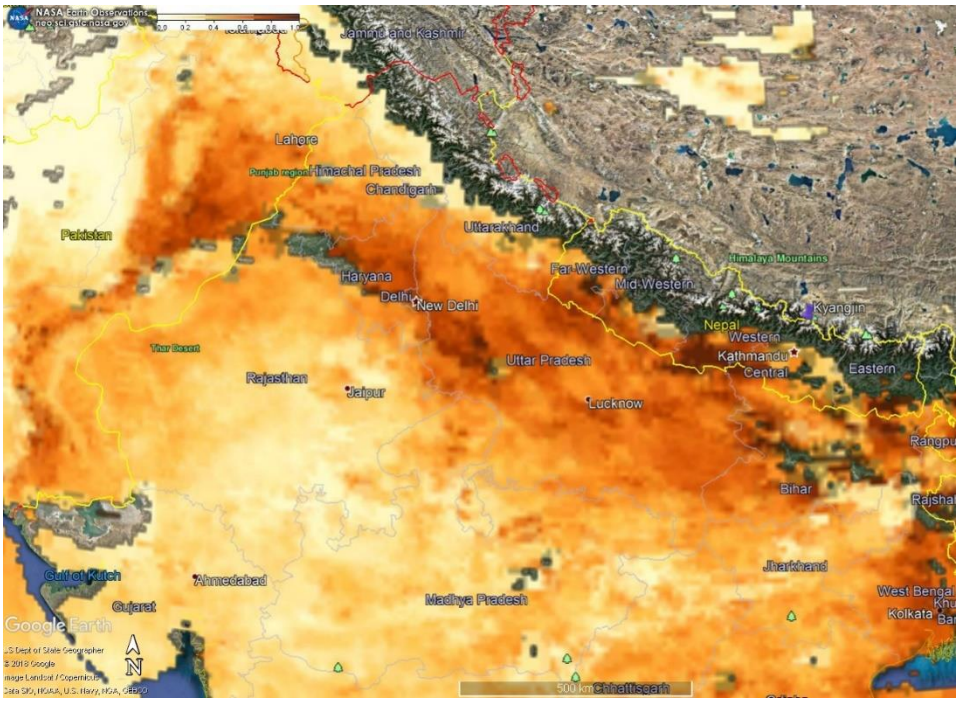

Figure 30: Average AOD data from 2018-04-23 till 2018-04-30 (source: https://neo.sci.gsfc.nasa.gov/view.php?datasetId=MODAL2_E_AER_OD&date=2018-11-01)

6. Discussion

6.1 LAP composition and concentrations

Coarse LAPs

Approximately 85% of the total classified material on the vertical glass slides consisted of transparent silica (Figure 14). Besides the high number of transparent silicate particles, this LAP class also had the largest area coverage on the glass slides for all measurement locations, for both the vertical and the horizontal glass slides. From this can be concluded that transparent silica is the most abundant (coarse) LAP type in the study area. After transparent silica, organic material and silica with brown/black material have the highest abundancy, with a slightly higher number for organic material. Small black and large black materials had, in area coverage, the lowest abundance. This corresponds with the measurements from the study of Takeuchi et al. (2001) who measured that the wind-blown material at Yala Glacier, which is located in the Langtang Valley, mainly consisted of brown or transparent mineral particles and some plant fragments (Takeuchi et al., 2001).

For all measurement locations the vertical slides collected the most LAPs. Cornelis et al. (1997) stated that the vertical glass slides catch dust from horizontal winds, the horizontal top glass slides catch fall-out material and the horizontal bottom glass slides catch local material. Therefore, the high content of LAPs on the vertical slides indicates that wind is an important factor in the number of LAPs. Furthermore, show the vertical slides a higher concentration of LAPs for locations were higher wind speeds are expected. Figure 15 shows that the glass slides at Kyanjin and Langshisha collected more LAPs than Lirung. Kyanjin and Langshisha were located at open areas while the measurements at Lirung were taken at a location in between high mountains, which possibly leads to lower wind speeds. There are no wind data available for Lirung and Langshisha to confirm that there were lower wind speeds at Lirung. However, the lower LAP content on the vertical slides at Lirung shows that there are less windblown LAPs at Lirung and therefore supports the expectation that there is less wind at Lirung. The concentrations of local LAPs (on the horizontal bottom slides) at Lirung and Kyanjin were similar while the values for local materials at Langshisha were lower. From this it can be established that Lirung and Kyanjin had higher concentrations of local LAPs compared to Langshisha.

Fine LAPs

The classified fine materials were similar to materials detected in other studies, who also found aluminosilicates/silicates, organic material, BC, Ca-rich particles and metals (Cong et al., 2008; Cong et al., 2009; Fan et al., 2016). Besides analysing a few particles to estimate the elemental composition of particles, these studies also made a quantitative estimation of the present materials (Table 7). Both studies measured high an abundance of aluminosilicates and silicates. This corresponds with the results of this study, where aluminosilicates and silicates were also observed frequently. Other similarities were the presence of Fe/Ti-rich particles and metal oxides, Ca-rich particles, BC and organic material. The abundance of BC (soot, tar ball and fly ash) was higher for the studies by Cong et al. (2009) and Cong et al. (2008), since BC was only observed ones or twice during this study (Table 6). This could be caused by the small size of BC compared to the other present materials. Because of this smaller size it is possible that some BC particles were covered by larger particles under the SEM and therefore not detected.

Table 7: Composition of materials for the Himalaya measured by Cong et al. (2009) and Cong et al. (2008)

	Cong et al. (2009)
Aluminosilicates	46%
Soot	25%
Calcium sulphates	11%
Fly ash	7%
Ca/Mg carbonates	5%
Biological particles	3%
Metal oxides	3%

	Cong et al. (2008)
Aluminosilicates/silica	55%
Calcium sulphates	16%
Biological particles	12%
Soot	8%
Tar ball	3%
Fe/Ti-rich particles	3%
Ca/Mg carbonates	2%
Pb-rich particles	1%

The classification of particles analysed with the SEM was based on chemical composition and morphology (Table 5). For most particles the chemical composition clearly identified the particle type. The chemical compositions of the aluminosilicates, silicates, organic material, metals, and Ca-rich particles corresponded with the classification criteria based on other studies (Table 5). For BC the chemical spectrum was a bit vague (Figure 21). Therefore, the images of the black carbon particles were also compared to images of BC particles in another study (Figure 31). The morphology between the particles in Figure 21 and Figure 31 is very similar. This supports the classification of the BC particles in this study.

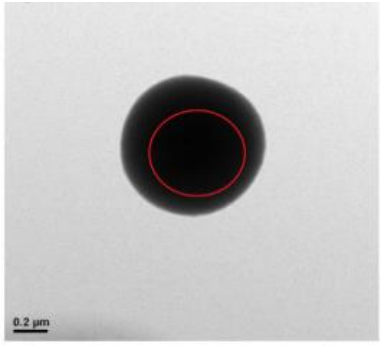

Figure 31: Example of a BC particle from the research of Fan et al. (2016)

By morphology, silicates and aluminosilicates were difficult to distinguish. The analysed particles in Figure 16 and Figure 17 look visually the same. However, the chemical spectra show a clear difference in composition, which makes it possible to differentiate aluminosilicates and transparent silicates. This shows the importance of elemental composition information for the classification of the particles and therefore the contribution of the SEM analysis for this research.

Because of the high abundance of aluminosilicates, the similarity in shape and size between silicates and aluminosilicates and the comparable high abundance of aluminosilicates in other studies it is assumed that the LAPs classified as silica with brown/black material, for the coarse materials with the microscope, were aluminosilicates. During classification of the coarse LAPs it was considered that all transparent materials with an irregular shape were transparent silicates. The aluminosilicates, (transparent) silicates and silicates with brown/black material are considered as dust. From the outcomes of the microscope and SEM analysis can be concluded that there were high dust concentrations and low BC concentrations in the study area during the field work period.

6.2 Dust deposition and seasonality

The dust deposition measured at Kyanjin was high for the pre- and post-monsoon seasons (+- 7 g/m^2/day) and low during the monsoon season (+- 0.5 g/m^2/day) (Figure 22). This corresponds with the outcomes of other studies, which measured the same seasonality for LAP concentrations in the

Himalaya (Chen et al., 2018; Ginot et al., 2014; Marinoni et al., 2010). At Lirung this seasonality was not observed and the highest dust deposition rates at Lirung were approximately three times lower compared to Kyanjin. A reason for the lower dust deposition rates at Lirung could be the higher elevation of the location, as aerosol concentrations decrease with elevation (Clarke et al., 2004). However, the elevation difference between Kyanjin and Lirung is only 360 meters, which makes it unlikely that the elevation difference would be the only cause for the difference in amounts of materials for the two locations.

Another reason for the higher dust deposition and seasonality at Kyanjin could be caused by the higher human activity at Kyanjin. The measurement location at Kyanjin is located near the village of Kyanjin, near hiking trails and next to a helicopter landing pad. Human activity and the helicopters could cause local dust to blow up, which increases the dust deposition rate. During the pre- and post-monsoon seasons there are more tourists at Kyanjin which likely causes higher human activity and more helicopter flights during these periods of the year. At the measurement station at Lirung there is lower human activity compared to Kyanjin and no nearby helicopter landing pad or hiking trail. This could contribute to the overall lower deposition rates and missing seasonality at Lirung.

Another cause could be lower wind speeds at Lirung. Because of the location of Lirung, in between high mountains, and the lower LAP contents on the vertical glass slides at Lirung, it is likely that wind speeds are lower here. Lower wind speeds decrease the amount of materials that can be transported by the atmosphere, and so lower the total amount of dust in the air. This influence by wind speed on the dust concentration in the air is also described in other studies. Marinoni et al. (2010) measured diurnal dust concentrations in the Himalaya and measured the lowest dust concentrations during the night, when the wind speed is the lowest, and increased concentrations for the afternoon when wind speeds are the highest. The measured wind data during the field work at Kyanjin showed the same diurnal wind pattern caused by thermal winds (Figure 12). The thermal winds cause up-valley winds during the day and subsiding winds at night. At lower elevations this diurnal pattern is present all year. In summer this diurnal pattern is also present at higher elevations, but during the winter this pattern is absent at high elevations and strong westerly winds take the upper hand. Furthermore, wind speeds increase during the winter (Potter et al., 2018). Therefore, besides the lower amount of material, lower wind speeds may also be a reason for lower seasonal influence on the dust deposition at Lirung.

6.3 Influence of the LAP types on the albedo

In general BC has a higher absorbing coefficient than dust. Therefor BC often has a higher influence on the ice albedo than dust (Literature review, Page 3). However, the rate to which BC reduces the albedo compared to dust is not a fixed value. This depends on the concentrations and absorbance capacities of the dust and BC, which are variable. The absorption of dust is highly sensitive to the content of iron oxides (Gabbi et al., 2015; Kaspari et al., 2014). Therefore, the iron concentration in dust samples is an indication for the light absorption by the dust. The exact iron concentration for the samples in this study is unknown. However, during the SEM analysis, iron was measured multiple times. Especially the aluminosilicates and metals regularly contained iron, 10 out of 27 aluminosilicate particles contained iron. This is an indication that the dust in the study area has a high absorptivity. Besides, the classification of the material showed much higher concentrations for dust than for BC. Therefore, it can be assumed that the impact of dust on the ice albedo was much higher than the impact of BC on glaciers in the Langtang Valley for the field work period.

6.4 LAP source and distribution

The CO, UVAI and AOD data show different patterns. It was expected that the images would show some similarities. Especially the CO and UVAI data show lack in correspondence. This is probably because the CO data do not show the dust in the air, while the UVAI seems to mainly respond to dust because of the high values at the Thar dessert. Another explanation for the lack in seasonality could be domination of light-reflecting aerosols in the air. The CO data show that there is BC present in the atmosphere. However, when the values of light-reflecting aerosols are higher than the BC and dust

concentrations the UVAI will give a negative value. The large scale AOD data from MODIS show the same pattern as the CO data, with high values at the Indo-Gangetic plain and low values in the study area (Figure 29).

Data for the vertical CO column showed high concentrations (>0.064 mol/m^2) for the Indo-Gangetic plain where pollution is expected to be high, and low concentrations for the Himalayan ridge (+-0.020 mol/m^2). Compared with values from other studies, the high values clearly indicate biomass burning. Menut et al. (2018) modelled CO values with and without biomass burning for Guinea. They modelled CO values between 0.025 and 0.033 mol/m^2 for a no biomass burning situation. For a situation with biomass burning they modelled values between 0.025 and 0.053 mol/m^2 (Menut et al., 2018). From this it can be established that locations with CO values above 0.033 mol/m^2 (Figure 24) are influenced by biomass burning and therefore have high values for BC concentrations. The values for the Langtang Valley lay around 0.020 mol/m^2. Therefore, it seems unlikely that BC from air pollution at the Indo-Gangetic plain reached the study area during the field work period. None of the images (Figure 24) show high CO concentrations for the Langtang Valley. The pollution sticks around the Indo-Gangetic plain and Central-Nepal. This observation is supported by the low concentrations of small and large black materials (potential BC) for the coarse LAP classification and the low abundance of BC established during the SEM analysis, and by other studies, which measured a strong decrease in BC concentrations for an increase in elevation in the Himalaya (Table 1).

The aerosol index images (Figure 26) show, that for most days, there are low concentrations of LAPs present near the study area. However, these LAPs are present at the northern side of the study area which makes it unlikely that those LAPs came from the Indo-Gangetic plain. Besides, the LAP content at the Indo-Gangetic plain was low during the field work period. On most images LAPs are present on the western side of the study area, in East-Pakistan and North-West India. Considering the south-western wind direction during the heavy winds in the afternoon, these LAPs could have reached the Langtang Valley during the later afternoon, since the images were made every day at 1:30 PM. Nonetheless, according to UVAI data it is unlikely that large amounts of pollution from the Indo-Gangetic plain were transported towards the study area during the field work period. However, these data are only for the field work period. Therefore, it is possible that pollution from the Indo-Gangetic plain reaches the study area during other times of the year, especially for the pre-monsoon. Since the UVAI data from TROPOMI are only available since June 2018 it is impossible to view the UVAI for the pre-monsoon.

To compare post-monsoon aerosol presence with monsoon and pre-monsoon values, the AOD at Kyanjin for the pre-monsoon and monsoon seasons were used. The pre-monsoon values are, as expected, much higher compared to the post-monsoon values. At the end of April (pre-monsoon) the AOD values were approximately three times higher than during October/November. For the June (monsoon) the AOD values were comparable to the post-monsoon values, while lower values were expected for this time of the year. However, only a few data points are present for June which make the data hard to compare. Furthermore, show the large scale AOD data from MODIS high values for the Langtang Valley during the pre-monsoon. The gathering of the aerosols before the Himalayan mountain ridge, which was clearly visible on the CO data and the AOD MODIS data for October, is absent here. It seems that the aerosols get higher up into the mountains during the pre-monsoon. This could be caused by western winds and the higher concentrations of aerosols in the air during the pre-monsoon.

High values of BC coming from the Indo-Gangetic plain towards the Langtang Valley seems very unlikely according to the CO, UVAI and AOD data for the field work period. The small amounts of BC measured during this study could be originated from local sources like cooking and heating fires. Nonetheless, the study of Kaspari et al. (2011) measured a threefold increase in BC concentrations on the northeast ridge of the Mt. Everest (at an elevation of 6518 m a.s.l.) from 1860 to 2000. Because BC concentrations also increased in this period by the industrial revolution (Skiles et al., 2018), this is an indication that some BC from polluted areas reaches the high Himalaya. The higher BC values measured by Kaspari et al. (2011) could be caused by increased BC during other seasons. Figure 30 shows that the AOD is much higher during the pre-monsoon towards the mountain ridge compared to

the field work period (Figure 29). This corresponds with other studies which mentioned that the dust distribution in the Himalaya is evenly over the year but that the BC deposition is concentrated during the pre-monsoon (Gabbi et al., 2015).

6.5 Further research

The combination of field and satellite data during this study made it possible to get a better understanding about the composition, concentrations, and sources of LAPs during the post-monsoon season in the Langtang valley. However, the outcomes could be different for other seasons. Therefore, it would be good to do the same research for the pre-monsoon. For this study some samples from the pre-monsoon season were used. However, this were too few samples to measure the difference between the pre- and post-monsoon seasons. The CO and UVAI data should also be analysed for the pre-monsoon season. For the AOD data this was already done during this study, with much higher AOD values for the pre-monsoon. It would be interesting to determine if this pattern also applies for the field, CO and UVAI data.

Because of the high concentrations of silicates and iron in the samples it is suspected that dust has a larger influence on the ice albedo than BC. However, the specific influence of the dust/BC particles on the ice albedo is unknown. For further research it would be interesting to measure the absorptivity of the dust in the samples. This can be done by measuring the iron concentrations in the samples, with a more extensive SEM analysis.

During the field work, samples from LAPs in the air and the LAP deposition were used. However, there were no LAP samples taken from glaciers. It is hard to take LAP samples from glaciers in this study area since LAP influenced glaciers are located at very high altitudes. For further research it would be interesting to take LAP measurements from these high elevated glaciers to determine what concentrations of LAPs reach the glaciers. Because of the hard accessibility of these glaciers another possibility would be to look further into remote sensing and modelling possibilities. For instance, to model if LAPs could reach these glaciers with the use of field data (from lower altitudes) and satellite data.

7. Conclusion

Transparent silica is the largest contributor of coarse LAPs, both in number and area for the Langtang Valley. In number, approximately 85% of the coarse materials consisted of transparent silicates. This applies for all measurement locations. Besides transparent silica, organic material, silica with brown/black material, and small and large black material are also present at all sample locations. However, in much smaller concentrations than transparent silica. The LAP composition of the coarse material is homogenous throughout the Langtang Valley. Kyanjin, Lirung and Langshisha showed similar results in the composition of coarse LAPs. The number of LAPs was not the same for the measurement locations. Wind speed is considered as the main driver for these differences. Vertical glass slides at windy locations caught much more LAPs than locations with lower wind speeds.

Fine materials are dominated by aluminosilicates/silicates and organic material in the Langtang Valley. Other identified materials with lower abundance are: metals, Ca-rich particles, and BC. The abundance of BC was very low. The similarity in morphology and size, but different elemental composition between silica and aluminosilicates validates the importance of information about the elemental composition, and so of the SEM analysis. The elemental compositions measured with the SEM analysis were very similar to the elemental compositions measured by other studies for the Himalaya.

The dust deposition in the Langtang Valley was the highest during the pre- and post-monsoon seasons and the lowest during the monsoon season. Although this seasonality was not observed at Lirung, it is assumed that this seasonality is also present here but at lower rates due to lower wind speeds, lower human activity, and higher elevation. Furthermore, were the dust deposition values for Kyanjin higher than for Lirung because of higher wind speeds at Kyanjin.

During the field work period CO did not penetrate into the mountains generally, but it might in other seasons. It is clear that CO values are high at the polluted areas like the Indo-Gangetic plain. The UVAI is overall negative at Langtang which indicates that there are only few LAPs in the area. The correspondence between the UVAI and the CO is poor. This is because CO is a measure for pollution while the UVAI seems to mainly respond to dust. The AOD values from AERONET measurements in the Langtang Valley were low for the field work period. The AOD values from MODIS showed that the AOD for the same period was high at the Indo-Gangetic plain and low for the Langtang Valley. This shows that the pollution from the plains did (barely) penetrate into the mountains during the field work period. Therefore, it is suspected that the little BC measured in the study area is originated from local sources. For the pre-monsoon season the AOD from AERONET measurement at Langtang showed higher values. The AOD values from MODIS in this season shows high values for the plains. These higher AOD values for the pre-monsoon season, indicate that some BC from further areas could reach the Langtang Valley during the pre-monsoon season.

To conclude, for the field work period it seems very unlikely that high concentrations of LAPs from further areas (the Indo-Gangetic plain) reach the Langtang Valley. Therefore, it is suspected that most LAPs come from local sources. Because of the high concentrations of dust and low concentrations of BC it is assumed that dust has a higher influence on the ice/snow albedo than BC in the Langtang Valley.

8. References

Adhikary, S., Nakawo, M., Seko, K., Shakya, B. (2000). Dust influence on the melting process of glacier ice: experimental results from Lirung Glacier, Nepal Himalayas. *Debris-covered glaciers (Proceedings of a workshop held at Seattle, Washington, USA),* 43-52

Adolph, A. C., Albert, M. R., Lazarcik, J., Dibb, J. E., Amante, J. M., & Price, A. (2017). Dominance of grain size impacts on seasonal snow albedo at open sites in New Hampshire. *Journal of Geophysical Research*, *122,* 121-139. https://doi.org/10.1002/2016JD025362

Apituley, A., Pedergnana, M., Sneep, M., Veefkind, J.P., Loyola, D., Landgraf, J., Borsdorff, T. (2018). Sentinel-5 precursor/TROPOMI level 2 Product user manual Carbon Monoxide. *KNIMI. Issue: 1.0.0.*

Bolch, T., Kulkarni, A., Kääb, A., Huggel, C., Paul, F., Cogley, J. G., Frey, H., Kargel, J.S., Fujita, K., Scheel, M., Bajracharya, S., Stoffel, M. (2012). The State and Fate of Himalayan Glaciers EH. *Science, 336*, 310–314.

Bonasoni, P., Laj, P., Marinoni, A., Sprenger, M., Angelini, F., Arduini, J., Bonafé, U., Calzolari, F., Colombo, T., Decesari, S., Di Biagio, C., di Sarra, A.G., Evangelisti, F., Duchi, R., Facchini, MC., Fuzzi, S., Gobbi, G.P., Maione, M., Panday, A., Roccato, F., Sellegri, K., Venzac, H., Verza, GP., Villani, P., Vuillermoz, E., Cristofanelli, P. (2010). Atmospheric Brown Clouds in the Himalayas: First two years of continuous observations at the Nepal Climate Observatory-Pyramid (5079 m). *Atmospheric Chemistry and Physics*, *10*(15), 7515–7531. https://doi.org/10.5194/acp-10-7515-2010

Brodowski, S., Amelung, W., Haumaier, L., Abetz, C., & Zech, W. (2005). Morphological and chemical properties of black carbon in physical soil fractions as revealed by scanning electron microscopy and energy-dispersive X-ray spectroscopy. *Geoderma*, *128,* 116-129. https://doi.org/10.1016/j.geoderma.2004.12.019

Buseck, P. R., Adachi, K., Gelencsér, A., Tompa, É., & Pósfai, M. (2012). Are black carbon and soot the same? *Atmospheric Chemistry and Physics Discussions*. *12,* 24821-24846. https://doi.org/10.5194/acpd-12-24821-2012

Chen, X., Kang, S., Cong, Z., Yang, J., & Ma, Y. (2018). Concentration, temporal variation, and sources of black carbon in the Mt. Everest region retrieved by real-time observation and simulation. *Atmos. Chem. Phys*, *18*, 12859–12875. https://doi.org/10.5194/acp-18-12859-2018

Clarke, A. D., Shinozuka, Y., Kapustin, V. N., Howell, S., Huebert, B., Doherty, S., Anderson, T., Covert,

D., Anderson, J., Hua, X., Moore, K.G., McNaughton, C., Carmichael, G., Weber, R. (2004). Size distributions and mixtures of dust and black carbon aerosol in Asian outflow: Physiochemistry and optical properties. *Journal of Geophysical Research D: Atmospheres*. *109,* 1-20. https://doi.org/10.1029/2003JD004378

Collier, E., & Immerzeel, W. W. (2015). High-resolution modeling of atmospheric dynamics in the Nepalese Himalaya. *Journal of Geophysical Research*. *120,* 9882-9896. https://doi.org/10.1002/2015JD023266

Cong, Z., Kang, S., Dong, S., Liu, X., & Qin, D. (2008). Elemental and individual particle analysis of atmospheric aerosols from high Himalayas. *Environmental Monitoring and Assessment*, *160,* 323-335. https://doi.org/10.1007/s10661-008-0698-3

Cong, Z., Kang S., & Qin D. (2009). Seasonal features of aerosol particles recorded in snow from Mt. Qomolangma (Everest) and their environmental implications. *Journal of Environmental Sciences*, *21,* 914-919. https://doi.org/10.1016/S1001-0742(08)62361-X

Cong, Z., Kawamura, K., Kang, S., & Fu, P. (2015). Penetration of biomass-burning emissions from South Asia through the Himalayas: New insights from atmospheric organic acids. *Scientific Reports*, *5(9580)*, 1–7. https://doi.org/10.1038/srep09580

Cornelis, W.M., Hartmann, R., Gabriels, D. (1997). Assessing and controlling dust pollution in the harbour of Ghent. *Department of soil management and soil care, University of Ghent, Belgium. Workshop on wind and water erosion.* 25-32.

Dong, Z., Kang, S., Qin, D., Shao, Y., Ulbrich, S., & Qin, X. (2018). Variability in individual particle structure and mixing states between the glacier–snowpack and atmosphere in the northeastern Tibetan Plateau. *The Cryosphere*, 12, 3877-3890. https://doi.org/10.5194/tc-12-3877-2018

Fan, J., Shao, L., Hu, Y., Wang, J., Wang, J., & Ma, J. (2016). Classification and chemical compositions of individual particles at an eastern marginal site of Tibetan Plateau. *Atmospheric Pollution Research*, *7,* 833-842. https://doi.org/10.1016/j.apr.2016.04.007

Fujita, K. (2007). Effect of dust event timing on glacier runoff: Sensitivity analysis for a Tibetan glacier. *Hydrological Processes*, *21,* 2892-2896. https://doi.org/10.1002/hyp.6504

Gabbi, J., Huss, M., Bauder, A., Cao, F., & Schwikowski, M. (2015). The impact of Saharan dust and black carbon on albedo and long-term mass balance of an Alpine glacier. *Cryosphere*, *9,* 1385-1400. https://doi.org/10.5194/tc-9-1385-2015

Ginot, P., Dumont, M., Lim, S., Patris, N., Taupin, J. D., Wagnon, P., Gilbert, A., Arnaud, Y., Marinoni, A., Bonasoni, P., Laj, P. (2014). A 10 year record of black carbon and dust from a Mera Peak ice core (Nepal): Variability and potential impact on melting of Himalayan glaciers. *Cryosphere*, *8*(4), 1479–1496. https://doi.org/10.5194/tc-8-1479-2014

Goossens, D., Gross, J., & Spaan, W. (2001). Aeolian dust dynamics in agricultural land areas in lower saxony, Germany. *Earth Surface Processes and Landforms*, *26,* 701-720. https://doi.org/10.1002/esp.216

Goossens, D., & Offer, Z. Y. (1994). An evaluation of the efficiency of some eolian dust collectors. *Soil Technology*, *7*, 25–35.

Gul, C., Puppala, S. P., Kang, S., Adhikary, B., Zhang, Y., Ali, S., Li, Y., Li, X. (2017). Concentrations and source regions of light absorbing impurities in snow/ice in northern Pakistan and their impact on snow albedo. *Atmospheric Chemistry and Physics Discussions*, *18*, 4981-5000. https://doi.org/10.5194/acp-2017-667

He, C., Li, Q. B., Liou, K. N., Zhang, J., Qi, L., Mao, Y., Gao, M., Lu, Z., Streets, D.G., Zhang, Q., Sarin, M.M., Ram, K. (2014). A global 3-D CTM evaluation of black carbon in the Tibetan Plateau. *Atmospheric Chemistry and Physics*, *14*(13), 7091–7112. https://doi.org/10.5194/acp-14-7091-2014

Herman, J. R., Bhartia, P. K., Torres, O., Hsu, C., Seftor, C., & Celarier, E. (1997). Global distribution of UV-absorbing aerosols from Nimbus 7/TOMS data. *Journal of Geophysical Research:*

Atmospheres, *102*(D14), 16911–16922. https://doi.org/10.1029/96JD03680

Huss, M., & Hock, R. (2018). Global-scale hydrological response to future glacier mass loss. *Nature Climate Change*, *8,* 135-140. https://doi.org/10.1038/s41558-017-0049-x

Immerzeel, W.W., van Beek, L.P.H., Bierkens, M.F.P. (2010). Climate change will affect the Asian water towers. *Science, 328,* 1382-1385. http://doi.org/10.1126/science.1183188.

Immerzeel, W. W., Petersen, L., Ragettli, S., & Pellicciotti, F. (2014). The importance of observed gradients of air temperature and precipitation for modeling runoff froma glacierized watershed in the Nepalese Himalayas. *Water Resources Research*, *50*, 2212–2226. https://doi.org/10.1002/2013WR014506.Received

Kaspari, S. D., Schwikowski, M., Gysel, M., Flanner, M. G., Kang, S., Hou, S., & Mayewski, P. A. (2011). Recent increase in black carbon concentrations from a Mt. Everest ice core spanning 1860-2000 AD. *Geophysical Research Letters*, *38,* L04703. https://doi.org/10.1029/2010GL046096

Kaspari, S., Painter, T. H., Gysel, M., Skiles, S. M., & Schwikowski, M. (2014). Seasonal and elevational variations of black carbon and dust in snow and ice in the Solu-Khumbu, Nepal and estimated radiative forcings. *Atmospheric Chemistry and Physics*, *14*(15), 8089–8103. https://doi.org/10.5194/acp-14-8089-2014

Kohshima, S., & Yoshimura, Y. (1993). Biotic Acceleration of Glacier Melting in Yala Glacier 9 Langtang Region , Nepal Himalaya. *Snow and Glacier Hydrology, 218,* 309-316.

Kokhanovsky, A.A., de Leeuw, G. (2009). Satellite aerosol remote sensing over land. *New York: Springer.* Chapter 2, Properties of aerosols; p. 19-63.

Lalitaporn, P., Kurata, G., Matsuoka, Y., Thongboonchoo, N., & Surapipith, V. (2013). Long-term analysis of NO2, CO, and AOD seasonal variability using satellite observations over Asia and intercomparison with emission inventories and model. *Air Quality, Atmosphere and Health*, *6,* 655-672. https://doi.org/10.1007/s11869-013-0205-z

Lau, W. K. M., Kim, M. K., Kim, K. M., & Lee, W. S. (2010). Enhanced surface warming and accelerated snow melt in the Himalayas and Tibetan Plateau induced by absorbing aerosols. *Environmental Research Letters*, *5*(2). https://doi.org/10.1088/1748-9326/5/2/025204

Li, C., Bosch, C., Kang, S., Andersson, A., Chen, P., Zhang, Q., Cong, Z., Chen, B., Qin, D., Gustafsson, Ö. (2016). Sources of black carbon to the Himalayan-Tibetan Plateau glaciers. *Nature Communications*, *7:12574.* https://doi.org/10.1038/ncomms12574

Lu, Z., Streets, D. G., Zhang, Q., & Wang, S. (2012). A novel back-trajectory analysis of the origin of black carbon transported to the Himalayas and Tibetan Plateau during 1996-2010. *Geophysical Research Letters*, *39*(1), 1–6. https://doi.org/10.1029/2011GL049903

Lüthi, Z. L., Škerlak, B., Kim, S. W., Lauer, A., Mues, A., Rupakheti, M., & Kang, S. (2015). Atmospheric brown clouds reach the Tibetan Plateau by crossing the Himalayas. *Atmospheric Chemistry and Physics*, *15*(11), 6007–6021. https://doi.org/10.5194/acp-15-6007-2015

Lutz, A. F., Immerzeel, W. W., Shrestha, A. B., & Bierkens, M. F. P. (2014). Consistent increase in High Asia's runoff due to increasing glacier melt and precipitation. *Nature Climate Change*, *4,* 587-592. https://doi.org/10.1038/nclimate2237

Marcq, S., Laj, P., Roger, J. C., Villani, P., Sellegri, K., Bonasoni, P., Marinoni, A., Cristofanelli, P., Verza, G.P., Bergin, M. (2010). Aerosol optical properties and radiative forcing in the high Himalaya based on measurements at the Nepal Climate Observatory-Pyramid site (5079 m a.s.l.). *Atmospheric Chemistry and Physics*, *10*(13), 5859–5872. https://doi.org/10.5194/acp-10-5859-2010

Marinoni, A., Cristofanelli, P., Laj, P., Duchi, R., Calzolari, F., Decesari, S., Sellegri, K., Vuillermoz, E., Verza, G.P., Villani, P., Bonasoni, P. (2010). Aerosol mass and black carbon concentrations, a two year record at NCO-P (5079 m, Southern Himalayas). *Atmospheric Chemistry and Physics*, *10*(17), 8551–8562. https://doi.org/10.5194/acp-10-8551-2010

Menut, L., Flamant, C., Turquety, S., Deroubaix, A., Chazette, P., & Meynadier, R. (2018). Impact of

biomass burning on pollutant surface concentrations in megacities of the Gulf of Guinea. *Atmospheric Chemistry and Physics*, *18,* 2687-2707. https://doi.org/10.5194/acp-18-2687-2018

Orr, A., Listowski, C., Couttet, M., Collier, E., Immerzeel, W., Deb, P., & Bannister, D. (2017). Sensitivity of simulated summer monsoonal precipitation in Langtang Valley, Himalaya, to cloud microphysics schemes in WRF. *Journal of Geophysical Research*, *122*(12), 6298–6318. https://doi.org/10.1002/2016JD025801

Painter, T. H., Barrett, A. P., Landry, C. C., Neff, J. C., Cassidy, M. P., Lawrence, C. R., McBride, K.E., Farmer, G. L. (2007). Impact of disturbed desert soils on duration of mountain snow cover. *Geophysical Research Letters*, *34*(12), 1–6. https://doi.org/10.1029/2007GL030284

Penning De Vries, M. J. M., Beirle, S., Hörmann, C., Kaiser, J. W., Stammes, P., Tilstra, L. G., Tuinder, O.N.E., Wagner, T. (2015). A global aerosol classification algorithm incorporating multiple satellite data sets of aerosol and trace gas abundances. *Atmospheric Chemistry and Physics*, *15,* 10597-10618. https://doi.org/10.5194/acp-15-10597-2015

Potter, E. R., Orr, A., Willis, I. C., Bannister, D., & Salerno, F. (2018). Dynamical Drivers of the Local Wind Regime in a Himalayan Valley. *Journal of Geophysical Research: Atmospheres*, *123(13),* 186-202. https://doi.org/10.1029/2018JD029427

Putero, D., Cristofanelli, P., Marinoni, A., Adhikary, B., Duchi, R., Shrestha, S. D., Verza, G.P., Landi, T.C., Calzolari, F., Busetto, M., Agrillo, G., Biancofiore, F., Di Carlo, P., Panday, A.K., Rupakheti, M., Bonasoni, P. (2015). Seasonal variation of ozone and black carbon observed at Paknajol, an urban site in the Kathmandu Valley, Nepal. *Atmospheric Chemistry and Physics*, *15,* 13957-13971. https://doi.org/10.5194/acp-15-13957-2015

Qian, Y., Flanner, M. G., Leung, L. R., & Wang, W. (2011). Sensitivity studies on the impacts of Tibetan Plateau snowpack pollution on the Asian hydrological cycle and monsoon climate. *Atmospheric Chemistry and Physics*, *11*(5), 1929–1948. https://doi.org/10.5194/acp-11-1929-2011

Qian, Y., Yasunari, T. J., Doherty, S. J., Flanner, M. G., Lau, W. K. M., Ming, J., Wang, H., Wang, M., Warren, S.G., Zhang, R. (2015). Light-absorbing particles in snow and ice: Measurement and modeling of climatic and hydrological impact. *Advances in Atmospheric Sciences*, *32,* 64-91. https://doi.org/10.1007/s00376-014-0010-0

Qu, B., Ming, J., Kang, S. C., Zhang, G. S., Li, Y. W., Li, C. D., Zhao, S.Y., Ji, Z.M., Cao, J. J. (2014). The decreasing albedo of the Zhadang glacier on western Nyainqentanglha and the role of light-absorbing impurities. *Atmospheric Chemistry and Physics*, *14,* 11117-11128. https://doi.org/10.5194/acp-14-11117-2014

Ramanathan, V., Ramana, M. V., Roberts, G., Kim, D., Corrigan, C., Chung, C., & Winker, D. (2007). Warming trends in Asia amplified by brown cloud solar absorption. *Nature*, *448*(7153), 575–578. https://doi.org/10.1038/nature06019

Ramanathan, V., Carmichael, G. (2008). Global and regional climate changes due to black carbon. *Nature Geoscience, 1,* 221-227.

Riksen, M. J. P. M., Goossens, D., Huiskes, H. P. J., Krol, J., & Slim, P. A. (2016). Geomorphology Constructing notches in foredunes : Effect on sediment dynamics in the dune hinterland. *Geomorphology*, *253*, 340–352. https://doi.org/10.1016/j.geomorph.2015.10.021

Scherler, D., Bookhagen, B., & Strecker, M. R. (2011). Spatially variable response of Himalayan glaciers to climate change affected by debris cover. *Nature Geoscience*, *4*(3), 156–159. https://doi.org/10.1038/ngeo1068

Schneider, C.A., Rasband, W.S., Eliceiri, K.W. (2012). NIH image to ImageJ: 25 years of image analysis. *Nat Methods, 9(7),* 671-675.

Schuster, G. L. (2005). The Angstrom Exponent and Bimodal Aerosol Size Distributions. *Journal of Geophysical research, 11,* D07207. https://doi.org/10.1029/

Skiles, S. M., Flanner, M., Cook, J. M., Dumont, M., & Painter, T. H. (2018). Radiative forcing by light-absorbing particles in snow. *Nature Climate Change, 8,* 964-971.

https://doi.org/10.1038/s41558-018-0296-5

Stein Zweers, D. C. (2018). *TROPOMI ATBD of the UV aerosol index document number : S5P-KNMI-L2-0008-RP, KNMI, issue: 1.1.*

Steinegger, U., Braun, L. N., Kappenberger, G., & Tartari, G. (1993). Assessment of Annual Snow Accumulation over the Past 10 Years at High Elevations in the Langtang Region. *Snow and Glacier Hydrology*, (218), 155–166.

Stokes, D.J. (2008). Principles and practice of variable pressure/environmental Scanning Electron Microscopy (VP-ESEM). United Kingdom: John Wiley & Sons Ltd. Chapter 2, Principles of SEM; p. 17-60.

Takeuchi, N., Kohshima, S., & Seko, K. (2001). Structure, Formation, and Darkening Process of Albedo-Reducing Material (Cryoconite) on a Himalayan Glacier: A Granular Algal Mat Growing on the Glacier. *Arctic, Antarctic, and Alpine Research*, *33*(2), 115–122. https://doi.org/10.2307/1552211

Thompson, L. G., Yao, T., Mosley - Thompson, E., Davis, M. E., Henderson, K. A., & Liu, P.-N. (2000). A High-Resolution Millenial Record of the South Asian Monsoon from Himalayan Ice Core. *Science*, *289*(2000), 1916–1919. https://doi.org/10.1126/science.289.5486.1916

Torres, O., Bhartia, P. K., Herman, J. R., Ahmad, Z., & Gleason, J. (1998). Derivation of aerosol properties from satellite measurements of backscattered ultraviolet radiation: Theoretical basis. *Journal of Geophysical Research Atmospheres*, *103*(D14), 17099–17110. https://doi.org/10.1029/98JD00900

Venkataraman, C., Habib, G., Eiguren-Fernandez, A., Miguel, A. H., & Friedlander, S. K. (2005). Residential biofuels in South Asia: Carbonaceous aerosol emissions and climate impacts: Supporting online material. *Science*, *307*(5714), 1–11.

Wang, M., Xu, B., Cao, J., Tie, X., Wang, H., Zhang, R., Qian, Y., Rasch, P.J., Zhao, S., Wu, G., Zhao, H., Joswiak, D.R., Li, J., Xie, Y. (2015). Carbonaceous aerosols recorded in a southeastern Tibetan glacier: Analysis of temporal variations and model estimates of sources and radiative forcing. *Atmospheric Chemistry and Physics*, *15,* 1191-1204. https://doi.org/10.5194/acp-15-1191-2015.

Warren, S.G., Wiscombe, W.J. (1980). A model for the spectral albedo of snow. 2: snow containing atmospheric aerosols. *Journal of the atmospheric sciences, 37,* 2734-2745.

Xu, J., Grumbine, R. E., Shrestha, A., Eriksson, M., Yang, X., Wang, Y. U. N., & Wilkes, A. (2009). The Melting Himalayas : Cascading Effects of Climate Change on Water , Biodiversity , and Livelihoods, *23*(3), 520–530. https://doi.org/10.1111/j.1523-1739.2009.01237.x

Yasunari, T. J., Bonasoni, P., Laj, P., Fujita, K., Vuillermoz, E., Marinoni, A., Cristofanelli, P., Duchi, R., Tartari, G., Lau, K. M. (2010). Estimated impact of black carbon deposition during pre-monsoon season from Nepal Climate Observatory - Pyramid data and snow albedo changes over Himalayan glaciers. *Atmospheric Chemistry and Physics*, *10,* 6603-6615. https://doi.org/10.5194/acp-10-6603-2010

Ye, D.-Z., & Wu, G.-X. (1998). The role of the heat source of the Tibetan Plateau in the general circulation. *Meteorology and Atmospheric Physics*, *67*(1–4), 181–198. https://doi.org/10.1007/BF01277509

Zhang, R., Wang, H., Qian, Y., Rasch, P. J., Easter, R. C., Ma, P. L., Singh, B., Huang, J., Fu, Q. (2015). Quantifying sources, transport, deposition, and radiative forcing of black carbon over the Himalayas and Tibetan Plateau. *Atmospheric Chemistry and Physics*, *15*(11), 6205–6223. https://doi.org/10.5194/acp-15-6205-2015

Satellite data and websites

- *Aeronet AOD data Kyanjin_Gompa (2018) David M.G., Holben B.N. 2018 October 10.*

https://aeronet.gsfc.nasa.gov/cgi-bin/type_one_station_opera_v2_new?site=Kyanjin_Gompa&nachal=0&year=26&month=9&aero_water=0&level=1&if_day=0&if_err=0&place_code=10&year_or_month=0
- *Aeronet system description (2017) Giles D.M., Holben B.N. 2017 December 04.* https://aeronet.gsfc.nasa.gov/new_web/system_descriptions.html
- *Aerosol optical depth EARONET (2018)* https://aeronet.gsfc.nasa.gov/new_web/aerosols.html
- *Aerosol Angstrom Exponent, NASA (2006) Kempler, S., Eaton, P., 2006 June 6.* https://web.archive.org/web/20060716001955/http://daac.gsfc.nasa.gov/PIP/shtml/aerosol_angstrom_exponent.shtml
- *Copernicus Sentinel-5P Data hub (2018) Produced from ESA remote sensing data* https://s5phub.copernicus.eu/dhus/#/home
- *Copernicus Atmosphere Monitoring Service (2018) Data catalogue* https://atmosphere.copernicus.eu/catalogue#/

9. Appendices

A. Tested methods to distract samples from Vaseline

The method to extract the samples from the Vaseline had to meet the following conditions. First, the samples should not be damaged by, for instance, chemicals or other substances. Second, it was important that as much sample material as possible was retained.

Before the field work, a few methods were tested to determine the best way to prepare the samples for further analysis:

- The first method was to dissolve Vaseline in Sobo and/or WD-40. The two solvents were tested to examine which one worked best and to make sure that the solvents did not damage the samples. When the Vaseline was dissolved the samples were centrifuged multiple times to extract the samples from the solution. Then, the samples were ready for microscopic preparation.
- The second method was to warm the glass slides with the Vaseline in an oven at 40°C to (partly) evaporate the Vaseline.

These tests were performed with test samples taken in the field work area during April 2018.
The best method to extract the Vaseline, was to dissolve the sample in WD-40. Warming the Vaseline only caused the Vaseline to melt but did not result into a better view of the samples under the microscope.

B. Dust collectors

Table B1: Kyanjin

Filter	Date placed	Date removed	Total time in the field (d)	Weight before field (g)	Weight after field (g)	Total weight of dust (g)	Notes
G001-LT7	2018-4-19	2018-4-23	4	51.49	52.61	1.12	
G001-LT14	2018-4-23	2018-4-28	5	48.91	50.11	1.20	
G001 LT16	2018-4-28	2018-5-30	32	50.92 (Utrecht)	51.35 (Nepal)	0.43	
G001 LT12	2018-5-30	2018-7-3	34	51.96 (Utrecht)	52.17 (Nepal)	0.21	Also dust in the plastic where

							the filter was kept
G001 LT13	2018-7-3	2018-10-24	113	48.57 (Utrecht)	49.85 (Nepal)	1.28	Lot of insects in the filter, half of the marbles were gone, lot of algae on the bag
001-08	2018-10-24	2018-11-01	8	49.10 (Nepal)	51.20 (Nepal)	2.10	
001-01	2018-11-01			47.90 (Nepal)			Still in the field

Table B2: Lirung

Filter	Date placed	Date removed	Total time in the field (d)	Weight before field (g)+location of scale	Weight after field (g)+ location of scale	Total weight of dust (g)	Notes
G001-LT19	2018-4-19	2018-4-28	9	48.48	48.83	0.35	
G001-LT18	2018-4-28	2018-5-30	32	48.99 (Utrecht)	49.10 (Nepal)	0.11	-
G001-LT9	2018-5-30	2018-7-2	33	49.00 (Utrecht)	52.33 (Nepal)	3.33	Some algae at the outside of the bag
G001-LT17	2018-7-2	2018-10-25	115	50.12 (Utrecht)	51.65 (Nepal)	1.53	Filter was not attached to the funnel anymore and a few marbles were missing
001-07-Lirung	2018-10-25	2018-11-01	7	48.52 (Nepal)	48.60 (Nepal)	0.08	
001-05	2018-11-01			48.24 (Nepal)			Still in the field

Table B3: Langshisha

Filter	Date placed	Date removed	Total time in the field (d)	Weight before field (g)	Weight after field (g)	Total weight of dust (g)	Notes
G001-LT15		2018-09-17		49.61 (Utrecht)	51.20 (Nepal)	1.59	
G001 LT11	2018-09-17	2018-10-25	38	48.00 (Utrecht)	47.47 (Nepal)	-0.53	Some insects, were removed before weighting

001-03-Lang	2018-10-25			47.08 (Nepal)			Still in the field

C. Glass dust detectors

Table C1: Kyanjin

Glass slide	Date placed	Date removed	Time placed	Time removed	Total time in the field (h:m)	Notes
g-k-h-t-10	2018-10-24	2018-10-25	12:25	13:35	25:10	
g-k-h-b-11	2018-10-24	2018-10-25	12:25	13:35	25:10	
g-k-v-9	2018-10-24	2018-10-25	12:25	13:35	25:10	
g-k-v-13	2018-10-25	2018-10-26	13:35	13:00	23:25	
g-k-h-t-17	2018-10-25	2018-10-26	13:35	13:00	23:25	There were some water drops on top of the Vaseline
g-k-h-b-15	2018-10-25	2018-10-26	13:35	13:00	23:25	
g-k-v-25	2018-10-26	2018-10-27	13:10	14:30	25:30	
g-k-h-t-29	2018-10-26	2018-10-27	13:10	14:30	25:30	
g-k-h-b-27	2018-10-26	2018-10-27	13:10	14:30	25:30	
g-k-v-37	2018-10-27	2018-10-28	14:30	14:30	24	
g-k-h-t-41	2018-10-27	2018-10-28	14:30	14:30	24	
g-k-h-b-39	2018-10-27	2018-10-28	14:30	14:30	24	
g-k-v-43	2018-10-28	2018-10-29	14:45	14:15	23:30	
g-k-h-t-47	2018-10-28	2018-10-29	14:45	14:15	23:30	
g-k-h-b-45	2018-10-28	2018-10-29	14:45	14:15	23:30	
g-k-v-56	2018-10-29	2018-10-30	14:15	14:00	23:45	
g-k-h-b-58	2018-10-29	2018-10-30	14:15	14:00	23:45	
g-k-h-t-60	2018-10-29	2018-10-30	14:15	14:00	23:45	
g-k-v-68	2018-10-30	2018-10-31	14:00	10:30	20:30	
g-k-h-b-72	2018-10-30	2018-10-31	14:00	10:30	20:30	

g-k-h-t-74	2018-10-30	2018-10-31	14:00	10:30	20:30	
g-k-v-92	2018-10-31	2018-11-01	10:30	14:15	27:45	
g-k-h-b-94	2018-10-31	2018-11-01	10:30	14:15	27:45	
g-k-h-t-96	2018-10-31	2018-11-01	10:30	14:15	27:45	
g-kdust-98	2018-11-01	-	-	-	-	Dust sample of material near measuring station Kyanjin. Measured by doping a glass slide into the ground

Table C2: Lirung

Glass slide	Date placed	Date removed	Time placed	Time removed	Total time in the field (h:m)	Notes
g-lir-h-t-6	?	2018-10-25	?	10:15	?	Slide was broken, many dust
g-lir-h-b-7	?	2018-10-25	?	10:15	?	Many dust
g-lir-v-8	?	2018-10-25	?	10:15	?	Many dust
g-lir-h-t-23	2018-10-25	2018-10-27	10:15	10:45	48:30	Vaseline was partly melted
g-lir-h-b-21	2018-10-25	2018-10-27	10:15	10:45	48:30	Vaseline was partly melted?
g-lir-v-19	2018-10-25	2018-10-27	10:15	10:45	48:30	Glass slide was broken, finger prints on the slide (to remove the slide)
g-lir-h-t-35	2018-10-27	2018-10-28	11:25	09:30	22:05	Vaseline melted a little
g-lir-h-b-33	2018-10-27	2018-10-28	11:25	09:30	22:05	Vaseline melted a little
g-lir-v-31	2018-10-27	2018-10-28	11:25	09:30	22:05	
g-lir-v-49	2018-10-28	2018-10-30	09:30	09:30	48	
g-lir-h-b-52	2018-10-28	2018-10-30	09:30	09:30	48	Vaseline melted a little
g-lir-h-t-54	2018-10-28	2018-10-30	09:30	09:30	48	Some hairs present. Vaseline melted a little
g-lir-v-82	2018-10-30	2018-11-01	09:30	09:30	10:00	
g-lir-h-b-84	2018-10-30	2018-11-01	09:30	09:30	10:00	Vaseline melted a little
g-lir-h-t-86	2018-10-30	2018-11-01	09:30	09:30	10:00	Vaseline melted a little

g-lir-mdust-1-88	2018-11-01	-	-	-	-	Slide doped in material just near the measurement station at Lirung
g-lir-mdust-2-90	2018-11-01	-	-	-	-	Slide doped in moraine material 10 meter North from measurement station at Lirung

Table C3: Langshisha

Glass slide	Date placed	Date removed	Time placed	Time removed	Total time in the field (h:m)	Notes
LAS-V-25102018-y2	2018-04-23	2018-10-25	08:40	16:00		Only vertical slide remained, others destroyed
LAS-T-HOR-y4	2018-10-25	2018-10-27	16:00	08:15	40:15	
LAS-B-HOR-y5	2018-10-25	2018-10-27	16:00	08:15	40:15	
LAS-Ver-y6	2018-10-25	2018-10-27	16:00	08:15	40:15	
LAS-T-HOR2-y10	2018-10-27	2018-10-28	08:15	08:15	24	
LAS-B-HOR2-y12	2018-10-27	2018-10-28	08:15	08:15	24	Slightly broken
LAS-ver2-y14	2018-10-27	2018-10-28	08:15	08:15	24	
LAN-smoke Campfire-y3	2018-10-27	-	07:45	-	-	Single sample of soot from campfire

Table C4: Additional slides

Location+slide	Coordinates	Elevation	Date placed	Date removed	Time placed	Time removed	Time in the field (h:m)	Notes
Sherpagoan Sherp-h-1	N28.16212 E85.39901	2615 m	2018-10-22	2018-10-23	17:55	07:25	13:30	
Thyangshyap Thang-g-h-5	N28.20800 E85.47567	3195 m	2018-10-23	2018-10-24	14:45	06:30	15:45	Near to house with smoke
Thyangshyap Thang-g-v-3	N28.20800 E85.47567	3195 m	2018-10-23	2018-10-24	14:45	06:30	15:45	Near to house with smoke
Kyanjin Bakery	N28.21243 E85.56764	3890	2018-10-29	2018-10-30	08:50	14:15	29:25	

g-kbak-v-62								
Kyanjin Bakery g-kbak-h-b-64	N28.21243 E85.56764	3890	2018-10-29	2018-10-30	08:50	14:15	29:25	
Kyanjin Bakery g-kbak-h-t-66	N28.21243 E85.56764	3890	2018-10-29	2018-10-30	08:50	14:15	29:25	Disturbed by animal/ human
Kyanjin Bakery g-kbak-v-76	N28.21243 E85.56764	3890	2018-10-30	2018-10-31	14:30	13:45	23:15	
Kyanjin Bakery g-kbak-h-b-78	N28.21243 E85.56764	3890	2018-10-30	2018-10-31	14:30	13:45	23:15	
Kyanjin Bakery g-kbak-h-t-80	N28.21243 E85.56764	3890	2018-10-30	2018-10-31	14:30	13:45	23:15	Disturbed by human /animal
Kyanjin Bakery g-kbak-v-16y	N28.21243 E85.56764	3890	2018-10-31	2018-11-01	13:45	15:00	25:15	
Kyanjin Bakery g-kbak-h-b-18y	N28.21243 E85.56764	3890	2018-10-31	2018-11-01	13:45	15:00	25:15	
Kyanjin Bakery g-kbak-h-t-20y	N28.21243 E85.56764	3890	2018-10-31	2018-11-01	13:45	15:00	25:15	Disturbed by human /animal
g-k-kitchen fire-1-y30	Holy land	3890	2018-11-01	-	-	-	00:01	1 minute above kitchen fire, Vaseline melted a little
g-k-kitchen fire-2-y35	Holy land	3890	2018-11-01	-	-	-	00:01	1 minute above kitchen fire
Bamboo glasslside-y22	N28.15588 E85.39796	1976	2018-11-03	2018-11-04	17:05	06:10	13:05	
Kath Summit glass slide- y24	N27.68604 E85.31179	1299	2018-11-06	2018-11-07	15:00	09:30	18:30	

D. Classification of the glass slides

Sample	Transparent silica	Silica with brown/black material	Organic	small black material	large black material	Notes
g-k-v-9-1	107	24	2	0	0	
g-k-v-9-2	105	30	7	4	0	
g-k-v-9-3	74	20	8	8	0	
g-k-v-9-4	84	18	9	9	2	
g-k-v-9-5	76	14	12	4	0	
g-k-v-9-6	92	11	17	6	0	
g-k-v-9-7	93	13	10	10	0	
g-k-v-9-8	93	14	9	5	1	
g-k-v-9-9	102	11	10	2	0	
g-k-v-9-10	112	10	8	6	0	
g-k-v-9-tot	**938**	**165**	**92**	**54**	**3**	
g-k-v-13-1	77	5	14	7	0	
g-k-v-13-2	68	6	13	6	0	
g-k-v-13-3	97	7	12	5	0	
g-k-v-13-4	50	9	10	7	2	
g-k-v-13-5	109	10	6	6	0	
g-k-v-13-6	93	15	12	10	1	
g-k-v-13-7	91	13	11	2	0	
g-k-v-13-8	105	10	7	4	0	
g-k-v-13-9	125	7	7	6	0	
g-k-v-13-10	110	4	7	2	0	
g-k-v-13-tot	**925**	**86**	**99**	**55**	**3**	
g-lir-v-19-1	36	0	1	0	0	
g-lir-v-19-2	36	2	0	0	0	
g-lir-v-19-3	18	2	2	1	0	
g-lir-v-19-4	46	3	4	2	0	

g-lir-v-19-5	65	2	2	0	0	
g-lir-v-19-6	46	1	0	1	0	
g-lir-v-19-7	31	1	1	1	1	
g-lir-v-19-8	47	2	1	0	0	
g-lir-v-19-9	51	0	2	3	0	
g-lir-v-19-10	37	1	1	1	0	
g-lir-v-19-tot	**413**	**14**	**14**	**9**	**1**	
g-k-v-25-1	91	10	10	2	1	
g-k-v-25-2	112	6	9	7	0	
g-k-v-25-3	111	5	10	3	0	
g-k-v-25-4	113	10	9	5	1	
g-k-v-25-5	101	10	7	8	0	
g-k-v-25-6	84	4	12	4	0	one big organic piece
g-k-v-25-7	92	3	16	2	1	
g-k-v-25-8	92	6	15	14	1	
g-k-v-25-9	75	10	9	5	0	
g-k-v-25-10	88	5	12	5	2	
g-k-v-25-tot	**959**	**69**	**109**	**55**	**6**	
g-lir-v-31-1	35	1	3	1	0	
g-lir-v-31-2	23	1	1	2	0	
g-lir-v-31-3	39	1	3	5	0	
g-lir-v-31-4	52	0	5	3	0	
g-lir-v-31-5	43	1	4	1	1	
g-lir-v-31-6	63	0	10	4	0	
g-lir-v-31-7	54	0	4	4	0	
g-lir-v-31-8	19	0	6	4	1	
g-lir-v-31-9	58	0	0	1	0	
g-lir-v-31-10	53	2	0	1	0	
g-lir-v-31-tot	**439**	**6**	**36**	**26**	**2**	
g-k-v-37-1	63	7	7	5	1	
g-k-v-37-2	53	2	10	7	1	

g-k-v-37-3	88	2	6	3	0	
g-k-v-37-4	61	3	8	3	1	
g-k-v-37-5	72	6	7	2	0	
g-k-v-37-6	70	3	5	2	0	
g-k-v-37-7	77	4	9	3	0	
g-k-v-37-8	69	5	9	0	0	
g-k-v-37-9	67	2	4	3	0	
g-k-v-37-10	49	4	5	3	0	
g-k-v-37-tot	**669**	**38**	**70**	**31**	**3**	
g-k-v-43-1	99	3	14	6	1	Large black triangle
g-k-v-43-2	103	8	11	5	0	Large organic piece
g-k-v-43-3	107	7	16	3	0	
g-k-v-43-4	110	7	10	5	0	
g-k-v-43-5	98	9	15	10	0	
g-k-v-43-6	93	5	23	3	2	
g-k-v-43-7	92	3	11	3	0	
g-k-v-43-8	76	9	22	8	0	
g-k-v-43-9	95	7	14	9	2	
g-k-v-43-10	111	10	10	10	0	
g-k-v-43-tot	**984**	**68**	**146**	**62**	**5**	
g-lir-v-49-1	31	1	2	1	0	
g-lir-v-49-2	35	0	3	0	0	
g-lir-v-49-3	34	1	1	1	0	
g-lir-v-49-4	49	0	1	4	1	
g-lir-v-49-5	49	4	11	6	0	
g-lir-v-49-6	55	5	9	2	0	
g-lir-v-49-7	60	5	5	4	0	Big piece of plant(organic)
g-lir-v-49-8	59	5	7	3	0	
g-lir-v-49-9	67	9	7	2	0	
g-lir-v-49-10	33	1	3	0	0	
g-lir-v-49-tot	**472**	**31**	**49**	**23**	**1**	

g-k-v-56-1	87	9	11	1	1	
g-k-v-56-2	101	10	21	6	0	
g-k-v-56-3	87	18	18	7	0	
g-k-v-56-4	99	5	31	7	0	
g-k-v-56-5	87	10	14	10	0	
g-k-v-56-6	83	6	10	5	2	Big plant on photo
g-k-v-56-7	98	5	20	6	0	Large organic material
g-k-v-56-8	83	3	23	8	0	
g-k-v-56-9	88	8	18	2	1	
g-k-v-56-10	89	2	30	6	0	
g-k-v-56-tot	**902**	**76**	**196**	**58**	**4**	
g-kbak-v-62-1	63	12	15	6	3	
g-kbak-v-62-2	63	5	15	8	2	
g-kbak-v-62-3	64	6	11	3	0	
g-kbak-v-62-4	57	6	13	9	0	
g-kbak-v-62-5	59	8	18	7	2	
g-kbak-v-62-6	62	6	21	8	1	
g-kbak-v-62-7	52	7	17	9	1	
g-kbak-v-62-8	62	2	13	6	2	
g-kbak-v-62-9	54	5	10	7	0	
g-kbak-v-62-10	52	5	18	8	1	
g-kbak-v-62-tot	**588**	**62**	**151**	**71**	**12**	
g-k-v-68-1	58	4	6	3	0	
g-k-v-68-2	32	4	7	3	0	
g-k-v-68-3	47	8	5	2	0	
g-k-v-68-4	45	5	3	2	0	
g-k-v-68-5	65	6	6	1	0	
g-k-v-68-6	55	3	5	4	0	piece of clustered black dots
g-k-v-68-7	62	3	2	0	0	
g-k-v-68-8	49	4	4	2	0	

g-k-v-68-9	47	2	5	2	1	piece of clustered black dots
g-k-v-68-10	67	3	2	0	0	
g-k-v-68-tot	**527**	**42**	**45**	**19**	**1**	
g-kbak-v-76-1	48	3	16	4	0	
g-kbak-v-76-2	50	2	10	7	1	
g-kbak-v-76-3	47	5	11	4	1	
g-kbak-v-76-4	41	4	4	10	0	
g-kbak-v-76-5	53	2	10	7	0	
g-kbak-v-76-6	35	7	9	1	1	
g-kbak-v-76-7	37	5	7	3	2	
g-kbak-v-76-8	38	4	13	2	1	
g-kbak-v-76-9	38	6	5	2	1	
g-kbak-v-76-10	24	2	7	2	0	
g-kbak-v-76-tot	**411**	**40**	**92**	**42**	**7**	
g-lir-v-82-1	39	2	3	0	0	
g-lir-v-82-2	45	1	1	0	0	
g-lir-v-82-3	51	1	2	0	0	
g-lir-v-82-4	47	1	2	0	1	
g-lir-v-82-5	45	2	0	0	0	
g-lir-v-82-6	38	0	0	0	0	
g-lir-v-82-7	37	1	1	0	0	
g-lir-v-82-8	46	1	1	0	0	
g-lir-v-82-9	37	1	1	0	0	
g-lir-v-82-10	30	1	1	0	0	
g-lir-v-82-tot	**415**	**11**	**12**	**0**	**1**	
g-k-v-92-1	104	9	18	3	0	
g-k-v-92-2	101	5	15	11	1	
g-k-v-92-3	98	6	21	5	2	
g-k-v-92-4	86	8	17	8	1	
g-k-v-92-5	80	5	17	3	0	
g-k-v-92-6	77	6	19	17	1	

g-k-v-92-7	85	5	26	8	1
g-k-v-92-8	85	4	23	10	0
g-k-v-92-9	82	7	21	5	0
g-k-v-92-10	81	4	23	9	1
g-k-v-92-tot	**879**	**59**	**200**	**79**	**7**
las-v-1	61	2	3	1	1
las-v-2	52	1	1	3	0
las-v-3	40	0	5	2	0
las-v-4	39	2	4	5	0
las-v-5	42	1	0	2	0
las-v-6	53	2	1	1	1
las-v-7	40	1	4	3	0
las-v-8	46	1	3	4	0
las-v-9	63	3	2	1	1
las-v-10	46	0	2	3	0
las-v-tot	**482**	**13**	**25**	**25**	**3**
las-ver2-1	79	1	2	12	0
las-ver2-2	71	0	5	2	0
las-ver2-3	63	0	9	2	0
las-ver2-4	71	0	3	2	0
las-ver2-5	73	3	6	3	1
las-ver2-6	65	1	7	3	0
las-ver2-7	76	0	6	2	0
las-ver2-8	67	0	4	2	0
las-ver2-9	69	1	5	2	0
las-ver2-10	55	0	5	4	0
las-ver2-tot	**689**	**6**	**52**	**34**	**1**
g-kbak-v-16y-1	70	6	4	4	0
g-kbak-v-16y-2	38	8	10	6	4
g-kbak-v-16y-3	47	7	10	3	0
g-kbak-v-16y-4	34	3	8	6	0

g-kbak-v-16y-5	57	6	12	1	0	
g-kbak-v-16y-6	41	8	16	3	1	
g-kbak-v-16y-7	38	5	7	5	2	
g-kbak-v-16y-8	48	8	9	3	0	
g-kbak-v-16y-9	44	7	5	0	2	
g-kbak-v-16y-10	38	4	8	3	2	
g-kbak-v-16y-tot	**455**	**62**	**89**	**34**	**11**	
thang-v-1	13	1	2	1	0	
thang-v-2	32	0	6	1	0	
thang-v-3	33	2	5	3	0	
thang-v-4	27	1	4	3	0	
thang-v-5	25	2	0	0	0	
thang-v-6	21	1	2	3	0	
thang-v-7	25	0	1	2	0	
thang-v-8	38	1	4	2	0	
thang-v-9	25	0	2	2	0	
thang-v-10	41	1	0	1	0	
thang-v-tot	**280**	**9**	**26**	**18**	**0**	
g-k-h-t-10-1	36	0	0	1	0	
g-k-h-t-10-2	37	1	1	0	0	
g-k-h-t-10-3	44	0	0	0	0	
g-k-h-t-10-4	41	1	1	0	0	
g-k-h-t-10-5	35	0	1	0	0	
g-k-h-t-10-6	35	0	2	0	0	
g-k-h-t-10-7	27	0	0	1	0	
g-k-h-t-10-8	43	0	1	0	0	
g-k-h-t-10-9	36	1	1	1	0	
g-k-h-t-10-10	29	1	0	0	0	
g-k-h-t-101-tot	**363**	**4**	**7**	**3**	**0**	
g-k-h-b-11-1	20	0	0	1	0	
g-k-h-b-11-2	44	2	0	0	0	Leg of a animal

g-k-h-b-11-3	22	0	2	0	0	
g-k-h-b-11-4	21	1	1	0	0	
g-k-h-b-11-5	21	2	1	0	0	
g-k-h-b-11-6	31	1	1	0	0	
g-k-h-b-11-7	32	1	1	1	0	
g-k-h-b-11-8	24	1	0	1	0	
g-k-h-b-11-9	22	2	0	1	0	
g-k-h-b-11-10	16	0	0	1	0	
g-k-h-b-11-tot	**253**	**10**	**6**	**5**	**0**	
g-k-h-b-15-1	33	3	2	1	0	
g-k-h-b-15-2	25	1	0	0	0	
g-k-h-b-15-3	6	0	1	1	3	
g-k-h-b-15-4	13	1	1	0	0	
g-k-h-b-15-5	22	0	5	1	0	
g-k-h-b-15-6	15	0	1	1	0	
g-k-h-b-15-7	21	0	0	2	1	
g-k-h-b-15-8	23	0	0	0	0	
g-k-h-b-15-9	23	0	2	1	0	
g-k-h-b-15-10	26	2	3	1	0	
g-k-h-b-15-tot	**207**	**7**	**15**	**8**	**4**	
g-k-h-t-17-1	33	3	1	0	0	
g-k-h-t-17-2	31	1	2	1	0	
g-k-h-t-17-3	37	0	1	1	0	
g-k-h-t-17-4	23	0	0	0	0	
g-k-h-t-17-5	33	1	2	0	0	
g-k-h-t-17-6	24	1	1	1	0	
g-k-h-t-17-7	36	0	0	2	0	
g-k-h-t-17-8	25	1	2	0	0	Large organic piece
g-k-h-t-17-9	36	0	1	0	0	
g-k-h-t-17-10	35	2	0	1	0	
g-k-h-t-17-tot	**313**	**9**	**10**	**6**	**0**	

g-lir-h-b-21-1	14	0	1	2	0
g-lir-h-b-21-2	20	0	1	0	0
g-lir-h-b-21-3	24	0	2	1	0
g-lir-h-b-21-4	26	1	0	0	0
g-lir-h-b-21-5	7	0	0	0	1
g-lir-h-b-21-6	15	1	0	1	0
g-lir-h-b-21-7	34	1	1	1	0
g-lir-h-b-21-8	23	0	0	0	0
g-lir-h-b-21-9	26	0	0	1	0
g-lir-h-b-21-10	30	0	0	0	0
g-lir-h-b-21-tot	**219**	**3**	**5**	**6**	**1**
g-lir-h-t-23-1	26	2	0	2	0
g-lir-h-t-23-2	20	2	2	1	0
g-lir-h-t-23-3	31	1	1	2	0
g-lir-h-t-23-4	27	2	1	1	0
g-lir-h-t-23-5	30	2	2	0	0
g-lir-h-t-23-6	29	2	2	2	0
g-lir-h-t-23-7	31	1	3	2	1
g-lir-h-t-23-8	34	0	2	0	0
g-lir-h-t-23-9	20	1	0	2	0
g-lir-h-t-23-10	28	0	3	0	0
g-lir-h-t-23-tot	**276**	**13**	**16**	**12**	**1**
g-k-h-b-27-1	29	1	0	2	0
g-k-h-b-27-2	30	1	1	1	0
g-k-h-b-27-3	44	1	1	0	0
g-k-h-b-27-4	38	0	1	2	0
g-k-h-b-27-5	36	2	1	1	0
g-k-h-b-27-6	30	0	0	1	0
g-k-h-b-27-7	34	1	0	1	0
g-k-h-b-27-8	30	1	0	1	0
g-k-h-b-27-9	41	0	1	1	0

g-k-h-b-27-10	31	3	0	0	0	
g-k-h-b-27-tot	**343**	**10**	**5**	**10**	**0**	
g-k-h-t-29-1	36	0	1	0	0	
g-k-h-t-29-2	23	1	1	0	0	
g-k-h-t-29-3	43	0	0	1	0	
g-k-h-t-29-4	37	1	0	2	0	
g-k-h-t-29-5	35	2	0	1	0	
g-k-h-t-29-6	21	0	0	0	0	
g-k-h-t-29-7	36	0	0	2	0	
g-k-h-t-29-8	37	0	2	2	0	
g-k-h-t-29-9	38	0	0	2	1	
g-k-h-t-29-10	42	1	2	2	0	
g-k-h-t-29-tot	**348**	**5**	**6**	**12**	**1**	
g-lir-h-b-33-1	29	1	0	0	0	
g-lir-h-b-33-2	30	0	0	0	0	
g-lir-h-b-33-3	39	1	2	0	0	
g-lir-h-b-33-4	29	2	0	0	0	
g-lir-h-b-33-5	29	0	1	1	0	
g-lir-h-b-33-6	36	1	0	0	0	
g-lir-h-b-33-7	38	0	1	2	0	
g-lir-h-b-33-8	34	0	1	1	0	
g-lir-h-b-33-9	36	0	1	0	0	Large organic piece
g-lir-h-b-33-10	10	0	2	2	0	
g-lir-h-b-33-tot	**310**	**5**	**8**	**6**	**0**	
g-lir-h-t-35-1	30	1	0	1	0	
g-lir-h-t-35-2	60	3	1	5	0	
g-lir-h-t-35-3	30	1	0	0	0	
g-lir-h-t-35-4	27	1	1	1	0	
g-lir-h-t-35-5	27	1	1	0	0	
g-lir-h-t-35-6	41	2	2	1	0	
g-lir-h-t-35-7	22	1	0	0	0	

g-lir-h-t-35-8	44	5	3	0	0	
g-lir-h-t-35-9	39	0	1	1	0	
g-lir-h-t-35-10	70	4	1	2	0	
g-lir-h-t-35-tot	**390**	**19**	**10**	**11**	**0**	
g-k-h-t-41-1	32	1	5	2	0	
g-k-h-t-41-2	15	2	1	1	0	
g-k-h-t-41-3	39	0	2	1	0	
g-k-h-t-41-4	41	2	3	2	0	
g-k-h-t-41-5	41	1	0	0	0	
g-k-h-t-41-6	51	2	6	1	1	
g-k-h-t-41-7	29	0	0	1	0	
g-k-h-t-41-8	41	0	1	1	0	
g-k-h-t-41-9	40	0	3	2	0	Large organic piece
g-k-h-t-41-10	37	1	1	1	0	
g-k-h-t-41-tot	**366**	**9**	**22**	**12**	**1**	
g-k-h-b-45-1	10	1	0	0	0	
g-k-h-b-45-2	19	2	5	2	0	
g-k-h-b-45-3	28	1	0	0	0	
g-k-h-b-45-4	47	0	1	1	0	
g-k-h-b-45-5	39	0	0	0	0	
g-k-h-b-45-6	41	1	1	0	0	
g-k-h-b-45-7	33	2	2	2	0	
g-k-h-b-45-8	37	0	3	1	0	
g-k-h-b-45-9	35	1	2	0	1	
g-k-h-b-45-10	27	0	0	0	0	
g-k-h-b-45-tot	**316**	**8**	**14**	**6**	**1**	
g-k-h-t-47-1	31	5	3	3	0	
g-k-h-t-47-2	20	1	1	2	2	
g-k-h-t-47-3	39	4	5	3	0	
g-k-h-t-47-4	31	1	2	1	0	
g-k-h-t-47-5	18	1	4	2	0	

g-k-h-t-47-6	47	3	3	2	3	
g-k-h-t-47-7	31	1	1	2	0	
g-k-h-t-47-8	39	3	2	2	0	
g-k-h-t-47-9	39	2	7	4	0	
g-k-h-t-47-10	30	5	2	0	0	
g-k-h-t-47-tot	**325**	**26**	**30**	**21**	**5**	
g-lir-h-b-52-1	23	1	1	0	0	
g-lir-h-b-52-2	31	1	2	0	0	
g-lir-h-b-52-3	35	1	1	0	0	
g-lir-h-b-52-4	43	0	1	0	0	
g-lir-h-b-52-5	41	0	1	1	0	
g-lir-h-b-52-6	37	2	3	0	0	
g-lir-h-b-52-7	29	0	1	0	0	
g-lir-h-b-52-8	38	0	3	0	0	
g-lir-h-b-52-9	29	1	2	2	0	
g-lir-h-b-52-10	32	1	0	0	1	
g-lir-h-b-52-tot	**338**	**7**	**15**	**3**	**1**	
g-lir-h-t-54-1	52	3	4	3	0	
g-lir-h-t-54-2	34	1	0	1	0	
g-lir-h-t-54-3	39	4	8	2	0	
g-lir-h-t-54-4	51	3	4	2	0	
g-lir-h-t-54-5	46	1	3	6	0	
g-lir-h-t-54-6	30	2	5	4	0	
g-lir-h-t-54-7	54	1	4	3	0	
g-lir-h-t-54-8	34	2	9	6	0	Large organic piece
g-lir-h-t-54-9	58	3	5	3	0	
g-lir-h-t-54-10	51	0	2	1	0	
g-lir-h-t-54-tot	**449**	**20**	**44**	**31**	**0**	
g-k-h-t-60-1	29	1	2	1	0	
g-k-h-t-60-2	34	1	1	0	0	
g-k-h-t-60-3	33	1	2	0	0	

g-k-h-t-60-4	35	0	2	0	1	
g-k-h-t-60-5	58	1	1	1	0	
g-k-h-t-60-6	51	1	0	0	0	
g-k-h-t-60-7	38	1	1	0	0	
g-k-h-t-60-8	47	1	0	0	1	
g-k-h-t-60-9	34	0	0	0	0	
g-k-h-t-60-10	37	0	1	0	0	
g-k-h-t-60-tot	**396**	**7**	**10**	**2**	**2**	
g-kbak-h-b-64-1	31	3	2	3	0	
g-kbak-h-b-64-2	37	0	1	3	0	
g-kbak-h-b-64-3	38	0	8	1	2	
g-kbak-h-b-64-4	34	1	2	2	0	
g-kbak-h-b-64-5	41	3	4	5	2	
g-kbak-h-b-64-6	42	1	3	1	0	
g-kbak-h-b-64-7	20	2	3	2	0	
g-kbak-h-b-64-8	43	1	5	1	0	
g-kbak-h-b-64-9	38	2	7	1	0	
g-kbak-h-b-64-10	29	2	3	0	1	
g-kbak-h-b-64-tot	**353**	**15**	**38**	**19**	**5**	
g-kbak-h-t-66	to disturbed					
g-lir-h-t-6	to disturbed					
g-k-h-b-72-1	27	0	1	0	0	
g-k-h-b-72-2	36	0	1	0	0	
g-k-h-b-72-3	15	0	1	0	0	
g-k-h-b-72-4	30	0	0	0	0	
g-k-h-b-72-5	26	0	1	0	0	Large organic piece
g-k-h-b-72-6	8	0	0	0	0	
g-k-h-b-72-7	4	1	0	0	0	
g-k-h-b-72-8	11	0	1	0	0	
g-k-h-b-72-9	21	1	0	0	0	
g-k-h-b-72-10	10	0	0	1	0	

g-k-h-b-72-tot	**188**	**2**	**5**	**1**	**0**
g-k-h-t-74-1	to disturbed				
g-kbak-h-b-78-1	22	0	1	1	0
g-kbak-h-b-78-2	47	0	3	1	0
g-kbak-h-b-78-3	30	1	2	1	0
g-kbak-h-b-78-4	26	2	4	0	0
g-kbak-h-b-78-5	57	4	6	1	1
g-kbak-h-b-78-6	40	0	1	0	0
g-kbak-h-b-78-7	27	2	5	2	0
g-kbak-h-b-78-8	27	0	3	1	0
g-kbak-h-b-78-9	29	2	7	3	3
g-kbak-h-b-78-10	43	0	3	0	0
g-kbak-h-b-78-tot	**348**	**11**	**35**	**10**	**4**
g-kbak-h-t-80	to disturbed				
g-lir-h-b-84-1	32	0	0	0	0
g-lir-h-b-84-2	30	0	0	0	0
g-lir-h-b-84-3	16	0	1	0	0
g-lir-h-b-84-4	30	0	0	0	0
g-lir-h-b-84-5	22	0	1	1	0
g-lir-h-b-84-6	36	0	0	0	0
g-lir-h-b-84-7	42	0	0	0	0
g-lir-h-b-84-8	28	0	0	0	0
g-lir-h-b-84-9	31	0	0	0	0
g-lir-h-b-84-10	31	0	0	0	0
g-lir-h-b-84-tot	**298**	**0**	**2**	**1**	**0**
g-lir-h-t-86-1	40	0	1	0	0
g-lir-h-t-86-2	31	1	1	1	0
g-lir-h-t-86-3	22	2	0	0	0
g-lir-h-t-86-4	44	1	0	0	0
g-lir-h-t-86-5	30	1	2	0	0
g-lir-h-t-86-6	24	0	2	0	0

g-lir-h-t-86-7	35	0	0	0	0		
g-lir-h-t-86-8	44	1	1	0	0		
g-lir-h-t-86-9	40	0	0	0	0		
g-lir-h-t-86-10	33	0	1	0	0		
g-lir-h-t-86-tot	**343**	**6**	**8**	**1**	**0**		
g-k-h-b-94-1	31	4	2	0	0		
g-k-h-b-94-2	31	2	1	0	0		
g-k-h-b-94-3	23	1	2	0	0		
g-k-h-b-94-4	8	0	0	0	1		
g-k-h-b-94-5	21	1	1	0	0		
g-k-h-b-94-6	34	0	4	0	0		
g-k-h-b-94-7	37	2	1	0	0		
g-k-h-b-94-8	27	0	1	1	0		
g-k-h-b-94-9	37	1	2	0	0		
g-k-h-b-94-10	30	0	2	1	0		
g-k-h-b-94-tot	**279**	**11**	**16**	**2**	**1**		
g-k-h-t-96-1	34	3	1	1	0		
g-k-h-t-96-2	20	0	0	5	0		
g-k-h-t-96-3	19	0	0	0	0		
g-k-h-t-96-4	35	0	1	0	0		
g-k-h-t-96-5	23	0	0	1	0		
g-k-h-t-96-6	28	2	0	0	0		
g-k-h-t-96-7	11	0	1	1	0		
g-k-h-t-96-8	22	1	3	0	0		
g-k-h-t-96-9	22	1	1	0	0		
g-k-h-t-96-10	24	1	0	1	0		
g-k-h-t-96-tot	**238**	**8**	**7**	**9**	**0**		
las-smoke-fire-1	8	0	0	0	1	1	soot
las-smoke-fire-2	4	0	0	0	0	4	soot
las-smoke-fire-3	3	0	1	0	2	0	soot
las-smoke-fire-4	1	0	0	1	0	1	soot

las-smoke-fire-5	1	0	0	0	2	2	Large piece of soot
las-smoke-fire-6	8	0	2	0	2	2	soot
las-smoke-fire-7	3	0	1	1	1	0	soot
las-smoke-fire-8	5	0	0	4	0	1	soot
las-smoke-fire-9	4	0	2	2	1	1	soot
las-smoke-fire-10	5	0	1	4	2	2	soot
las-smoke-fire-tot	**42**	**0**	**7**	**12**	**11**	**14**	soot
las-t-hor-1	5	0	0	0	0		
las-t-hor-2	16	5	1	0	0		
las-t-hor-3	11	0	0	2	0		
las-t-hor-4	19	0	0	0	0		
las-t-hor-5	15	1	0	1	0		
las-t-hor-6	20	1	2	3	1		
las-t-hor-7	8	0	1	1	0		
las-t-hor-8	13	0	2	5	0		
las-t-hor-9	10	0	0	1	0		
las-t-hor-10	9	0	0	3	1		
las-t-hor-tot	**126**	**7**	**6**	**16**	**2**		
las-b-hor-1	6	0	1	0	0		
las-b-hor-2	9	0	1	0	0		
las-b-hor-3	2	0	0	0	0		
las-b-hor-4	7	1	0	1	0	BC?	
las-b-hor-5	5	0	1	0	0		
las-b-hor-6	5	0	0	0	1		
las-b-hor-7	12	1	1	4	0	Soot?	
las-b-hor-8	4	0	0	2	0		
las-b-hor-9	2	0	0	0	0		
las-b-hor-10	8	0	0	0	0		
las-b-hor-tot	**60**	**2**	**4**	**7**	**1**		
las-t-h2-1	13	0	0	0	0		
las-t-h2-2	21	0	0	5	0		

las-t-h2-3	16	0	1	0	0	
las-t-h2-4	15	0	0	0	0	
las-t-h2-5	15	0	0	0	0	
las-t-h2-6	8	0	1	0	1	soot?
las-t-h2-7	18	0	0	3	0	
las-t-h2-8	20	0	0	0	0	
las-t-h2-9	18	0	0	0	0	
las-t-h2-10	23	0	0	0	0	
las-t-h2-tot	**167**	**0**	**2**	**8**	**1**	
las-b-h2-1	8	0	0	1	0	
las-b-h2-2	7	0	1	1	0	
las-b-h2-3	16	0	1	0	1	
las-b-h2-4	12	0	0	2	0	
las-b-h2-5	12	0	0	0	0	
las-b-h2-6	12	0	0	0	1	
las-b-h2-7	15	0	2	0	0	
las-b-h2-8	13	0	0	0	0	
las-b-h2-9	16	0	0	0	0	
las-b-h2-10	6	0	1	0	0	
las-b-h2-tot	**117**	**0**	**5**	**4**	**2**	
g-kbak-h-b-18y-1	29	4	3	0	0	BC?
g-kbak-h-b-18y-2	53	4	8	1	0	
g-kbak-h-b-18y-3	46	0	2	1	0	
g-kbak-h-b-18y-4	40	0	4	2	1	
g-kbak-h-b-18y-5	37	0	7	0	0	
g-kbak-h-b-18y-6	28	1	4	0	1	Large piece organic
g-kbak-h-b-18y-7	118	18	8	6	0	
g-kbak-h-b-18y-8	34	2	2	2	0	
g-kbak-h-b-18y-9	22	0	4	2	0	
g-kbak-h-b-18y-10	40	1	1	4	0	
g-kbak-h-b-18y-tot	**447**	**30**	**43**	**18**	**2**	

g-kbak-h-t-20y	to disturbed					
bamboo-22-1	28	1	0	0	0	
bamboo-22-2	33	0	1	0	0	
bamboo-22-3	21	0	0	0	0	
bamboo-22-4	36	0	0	0	0	
bamboo-22-5	21	0	0	0	0	
bamboo-22-6	30	0	0	0	0	
bamboo-22-7	37	0	0	0	0	
bamboo-22-8	25	0	0	0	0	
bamboo-22-9	28	0	0	0	0	
bamboo-22-10	27	0	0	0	0	
bamboo-22-tot	**286**	**1**	**1**	**0**	**0**	
kath-summit-24y-1	30	0	1	0	0	
kath-summit-24y-2	21	0	0	0	0	
kath-summit-24y-3	47	0	0	0	0	
kath-summit-24y-4	36	0	0	0	0	
kath-summit-24y-5	27	0	0	0	0	
kath-summit-24y-6	29	1	0	1	0	
kath-summit-24y-7	34	0	1	0	0	
kath-summit-24y-8	20	0	1	0	0	Animal
kath-summit-24y-9	41	0	1	0	0	
kath-summit-24y-10	27	0	0	0	0	
kath-summit-24y-tot	**312**	**1**	**4**	**1**	**0**	
k-kitchenfire1-1	31	0	1	0	0	
k-kitchenfire1-2	4	0	0	0	0	Veel luchtbellen
k-kitchenfire1-3	17	0	1	0	1	
k-kitchenfire1-4	18	0	0	0	0	
k-kitchenfire1-5	23	0	0	1	0	
k-kitchenfire1-6	17	0	1	0	0	

k-kitchenfire1-7	21	0	0	0	0	
k-kitchenfire1-8	10	0	0	0	0	
k-kitchenfire1-9	18	0	1	0	0	
k-kitchenfire1-10	Missing					
k-kitchenfire1-tot	**159**	**0**	**4**	**1**	**1**	
k-kitchenfire2-1	26	0	0	0	0	
k-kitchenfire2-2	27	0	0	0	0	
k-kitchenfire2-3	22	0	0	1	0	
k-kitchenfire2-4	20	0	0	1	0	
k-kitchenfire2-5	15	0	0	1	0	Black dash
k-kitchenfire2-6	18	0	0	0	0	
k-kitchenfire2-7	7	0	0	0	0	
k-kitchenfire2-8	21	0	0	0	0	
k-kitchenfire2-9	20	0	0	0	0	
k-kitchenfire2-10	17	0	0	1	0	
k-kitchenfire2-tot	**193**	**0**	**0**	**4**	**0**	
las-ver-april-1	22	4	4	4	0	
las-ver-april-2	40	0	2	5	0	
las-ver-april-3	34	0	1	1	0	
las-ver-april-4	35	0	5	1	0	
las-ver-april-5	28	2	4	1	1	
las-ver-april-6	31	0	2	4	0	
las-ver-april-7	30	0	7	1	0	
las-ver-april-8	48	0	2	5	0	
las-ver-april-9	37	1	7	2	0	
las-ver-april-10	31	0	6	4	0	
las-ver-april-tot	**336**	**7**	**40**	**28**	**1**	
k-ver-4-april-1	32	0	1	0	0	
k-ver-4-april-2	25	0	2	0	0	
k-ver-4-april-3	17	1	0	0	0	
k-ver-4-april-4	19	1	0	0	0	

k-ver-4-april-5	20	0	0	0	0
k-ver-4-april-6	56	0	0	0	0
k-ver-4-april-7	40	0	1	0	0
k-ver-4-april-8	26	0	1	0	0
k-ver-4-april-9	38	0	1	0	0
k-ver-4-april-10	22	0	0	1	0
k-ver-4-april-tot	**295**	**2**	**6**	**1**	**0**
lir-ver1-1	37	2	3	3	0
lir-ver1-2	43	0	4	4	0
lir-ver1-3	27	1	4	4	1
lir-ver1-4	31	0	2	2	0
lir-ver1-5	23	0	5	2	0
lir-ver1-6	45	0	3	2	0
lir-ver1-7	46	1	0	2	2
lir-ver1-8	43	1	1	1	0
lir-ver1-9	46	1	2	2	1
lir-ver1-10	31	1	6	2	0
lir-ver1-tot	**372**	**7**	**30**	**24**	**4**

E. Classification of the SEM measurements

The table contains the data obtained from the SEM analysis per measurements. Measurements with another colour (other than black) are measurements taken on the same particle. So, the red measurements at sample g-k-v-102-9 (1, 2 and 3) are three separate measurements taken on the same particle on the sample.

g-k-v-102-9	Major	Minor	Shape	Size(um)	Classification	Counts
1	Oxygen, Aluminium, Silica	Carbon	Irregular	>200	Aluminosilicate	9000
2	Oxygen, Aluminium, Silica	Carbon, Potassium	Irregular	>200	Aluminosilicate	
3	Oxygen, Carbon	Silica	Irregular	>200	Organic	9000
9	Silica ,Carbon, Oxygen	Calcium	Triangle	10	Silica	1200
10	Carbon, Oxygen	Silica, Iron	Irregular	100	Organic	3200
11	Silica, Oxygen	Carbon	Irregular	100	Silica	3200
12	Carbon, Oxygen	Calcium	Elongated	250(lengthwise)	Organic	850
13	Silica, Oxygen	Carbon, Aluminium	Rectangular	20	Silica	3400
14	Aluminium, Silica, Oxygen	Carbon	Irregular	20	Aluminosilicate	3000
15	-	-	-	-	-	24
16	Carbon, Oxygen	Silica, Aluminium	Irregular	100	Organic	80
17	Oxygen, Carbon	Silica, Aluminium	Irregular	100	Organic	60
18	Iron, Potassium	Oxygen, Carbon	Irregular	5	Metals	135
g-k-v-56	**Major**	**Minor**	**Shape**	**Size(um)**	**Material**	**Counts**
1	Carbon, Aluminium	-	Round	25	Black carbon	30
2	Carbon, Aluminium	Oxygen	Round	25	Black carbon	30
3	Carbon, Aluminium	Oxygen	Round	25	Black carbon	30
4	Carbon, Oxygen	Silica, Aluminium	Irregular	8	Organic	200
5	Carbon, Silica, Oxygen, Aluminium	-	Irregular	10	Aluminosilicate	300
6	Carbon, Oxygen	Silica, Aluminium	Irregular	8	Organic	400
7	Silica, Aluminium, Oxygen	Carbon	Irregular	10	Aluminosilicate	650
8	Silica, Aluminium, Oxygen, Carbon	Natrium, Potassium	Irregular	50	Aluminosilicate	12000
9	Silica, Oxygen	Carbon	Irregular	50	Silica	12000
10	Carbon, oxygen, Silica, Aluminium	Iron, Titanium, Tin	Irregular	40	Aluminosilicate	320

11	Silica, Aluminium, Carbon	Oxygen, Calcium, Iron	Irregular	60	Aluminosilicate	150
12	Silica, Aluminium, Carbon, Oxygen	Potassium, Iron	Irregular	20	Aluminosilicate	1200
13	Silica, Aluminium	Potassium, Carbon, Oxygen	Irregular	40	Aluminosilicate	1500
k-ver2	Major	Minor	Shape	Size(um)	Material	Counts
19	Silica, Oxygen	Aluminium, Carbon	Irregular	70	Aluminosilicate	800
20	Silica, Oxygen, Aluminium	Carbon, Natrium, Magnesium	Irregular	50	Aluminosilicate	13500
21	Silica, Oxygen	Carbon	Irregular	100	Silica	25000
22	Oxygen, Carbon, Silica, Aluminium	Iron, Potassium	Irregular	100	Organic/Aluminosilicate	9000
23	Calcium	Oxygen, Silica, Aluminium	Elongated	>100(lengthwise)	Calcium	400
24	Silica, Aluminium	Oxygen, Carbon, Iron, Potassium, Magnesium	Irregular	10	Aluminosilicate	
25	Iron, Aluminium, Silica	Potassium, Oxygen, Carbon	Irregular	50	Metals/Aluminosilicate	550
26	Silica, Oxygen	Aluminium, Potassium	Irregular	50	Silica	13000
27	Silica, Aluminium	Calcium, Oxygen, Natrium	Irregular	80	Aluminosilicate	1200
28	Silica, Aluminium, Oxygen	Carbon, Potassium	Irregular	30	Aluminosilicate	12000
29	Potassium	Silica, Aluminium, Oxygen, Carbon	Irregular	30	Metal	600
30	Silica, Oxygen		Irregular	30	Silica	24000
36	Silica, Iron, Potassium	Aluminium, Oxygen	Irregular	15	Metals/Silica	700
37	Potassium, Silica	Carbon, Oxygen, Aluminium	Irregular	15	Metals/Silica	850
38	Silica, Aluminium	Potassium, Oxygen	Irregular	5	Aluminosilicate	10500
39	Carbon	Oxygen	Irregular	2	Organic	5600
40	Potassium	Silica, Iron, Carbon, Aluminium	Irregular	30	Aluminosilicate	600
g-lir-v-						
49	**Major**	**Minor**	**Shape**	**Size(um)**	**Material**	**Counts**
1	Iron	Potassium, Tin	Irregular	50	Metals	500
2	Silica, Aluminium	Potassium, Oxygen, Carbon, Iron	Irregular	10	Aluminosilicate	1000
3	Iron, Potassium	Silica, Aluminium, Tin, Zirconium	Irregular	10	Metals	500
4	Carbon	Oxygen	Irregular	>100	Organic	18000
5	Silica, Oxygen	Carbon	Irregular	10	Silica	11000
6	Oxygen, Silica, Aluminium	Carbon, Magnesium, Iron	Irregular	10	Silica	5600
7	Silica, Potassium, Aluminium	Carbon, Oxygen	Irregular	10	?	2700
8	Oxygen, Silica, Aluminium	Carbon, Magnesium, Iron	Irregular	5	Aluminosilicate	6400

9	Silica, Aluminium	Natrium, oxygen	Irregular	10	Aluminosilicate	7200
10	Carbon	Oxygen, Iron	Irregular	100	Organic	600
11	Silica	Aluminium, Oxygen, Carbon	Irregular	2	Silica	7200
12	Silica, Aluminium, Oxygen, Carbon	Iron, Potassium, Magnesium	Rectangular	10	Aluminosilicate	4500
13	Silica, Aluminium, Oxygen	Iron, Carbon, Potassium, Magnesium	Rectangular	5	Aluminosilicate	5000
14	Silica, Oxygen	Carbon	Rectangular	>25	Silica	7200
15	Carbon, Oxygen, Silica	Aluminium	Irregular	30	Organic/Aluminosilicate	6400
16	Silica, Aluminium, Oxygen	Potassium, Carbon	Irregular	50	Aluminosilicate	650
17	Silica, Aluminium	Potassium, Carbon, Oxygen	Irregular	50	Aluminosilicate	100
18	Silica	Carbon, Oxygen	Irregular	15	Silica	50
19	Oxygen, Carbon	Silica, Aluminium, Natrium	Irregular	10	Organic	300
20	Oxygen, Carbon	Silica, Aluminium	Irregular	15	Organic	300
21	Silica, Aluminium	Carbon, Oxygen	Irregular	40	Aluminosilicate	200
22	Silica, Aluminium	Carbon, Oxygen, Natrium	Irregular	5	Aluminosilicate	100
las-v1	**major**	**minor**	**Shape**	**Size**	**Material**	**counts**
1	Carbon, Oxygen	Calcium, Silica	Irregular	150	Organic	100
2	Carbon	Oxygen	Irregular	150	Organic	25
3	Carbon	Silica, Aluminium, Oxygen	Irregular	50	Organic	75
4	Carbon	Oxygen	Irregular	30	Organic	20000
5	Carbon	Oxygen, Silica, Aluminium	Irregular	20	Organic	300
6	Carbon	Oxygen, Aluminium	Elongated	200(lengthwise)	Organic	200
7	Potassium	Carbon, Silica, Aluminium	Elongated	200(lengthwise)	Metal	500
8	Aluminium, Carbon	Oxygen	Irregular	50	Metal/Organic	72
9	Carbon	Oxygen	Irregular	10	Organic	500
10	Silica, Aluminium, Oxygen	Carbon, Potassium, Natrium	Triangle	20	Aluminosilicate	17000
11	Organic	Sulphur	spherical	20	Black carbon	150
12	Organic	Sulphur	spherical	20	Black carbon	200
13	Organic	Sulphur	spherical	20	Black carbon	200
14	Silica, Iron, Potassium	Carbon, Aluminium	Irregular	75	Silica/metals	700
15	Carbon	Silica, Aluminium, Oxygen	Irregular	75	Organic	10000
16	Carbon	Silica, Aluminium, Oxygen,	irregular	75	Organic	8000

17	Carbon, Natrium	Silica, Aluminium, Oxygen	irregular	75	Aluminosilicate/Natrium	18000